Politecnico di Torino

Corso di Laurea in Ingegneria Energetica

A.a. 2020/2021

Sessione di Laurea Ottobre 2021

Methane-assisted iron oxides chemical looping in a solar concentrator: tests in real conditions on the Energy Center rooftop

Relatori:

Prof. Massimo Santarelli

Dr. Davide Papurello

Candidato:

Luca Borghero

Abstract

Recent interest in hydrogen as an alternative fuel for lowering carbon emissions is funding the exploration of new ways for producing this molecule in a clean way. Iron oxides can be used within a process of chemical looping to produce hydrogen when switching from an oxidation state to another one. More specifically, they can lose oxygens at extremely high temperature in an inert atmosphere. The reaction can be helped by adding a gas to the reactor, so that it can happen at a temperature level reachable in a solar dish concentrator. The optimization and well-functioning of the solar facility is key for running the reaction. The materials used for the reactor and its shape highly influence the results. After a deep literature review about the technology and the chemical reaction, several tests with 35% methane feed were performed. Testing a pipe placed horizontally in the focus, alumina could not stand the extreme thermal stress, while steel (AISI 316 and Inconel Hastelloy c-276) lasted enough for the reaction to start, but eventually experienced melting. Operating at a temperature level above 1000 K helped the reaction to switch from methane chemical looping combustion to chemical looping reforming, thus favouring hydrogen and carbon monoxide yields. The gas flow outlet from the reactor reached a percentage up to 45% of hydrogen and 10% of carbon monoxide. Carbon dioxide instead reached very low concentrations. While carbon monoxide and carbon dioxide reached a peak at the beginning of the experiment and then decreased, hydrogen was oscillating around a stable value. Unreacted methane was detected. The temperatures recorded in the reactor and the gas mixture obtained were performed with the outputs of two different simulations studying the heat transfer and the chemistry of the experiment. Matching results highlighted the goodness and reliability of the models built.

CONTENTS

LIST OF FIGURES

LIST OF TABLES

1

INTRODUCTION

The necessity of finding innovative ways for producing alternative fuels is becoming more and more urgent as the climate crisis is showing its effects. By signing "2030 Climate Target Plan", Europe committed to reducing by 55% greenhouse gases emissions by 2030, and subsequently to becoming climate neutral by 2050 [1]. At the same time, renewable energy usage and improvements in energy efficiency are expected to rise by 32% and 32.5% respectively [2]. The urge of a change is visible in every field of our societies: not only the power production sector, but also other industrial sectors feel the need to switch to less carbon-intense processes.

An option for achieving this goal is the use of abundant renewable energies for the production and conversion of chemical substances into useful alternative fuels that have a lower impact on our atmosphere than conventional fuels. Fossil fuels, despite having enabled an incredible development of humans and their ways of living, make us pay the price of altering the earth-air carbon cycle. When burning, they release into the atmosphere additional quantities of CO_2 which are not fully reabsorbed by plants and fixed into organic carbon and therefore keep staying in gaseous form, increasing the capacity of the atmosphere of reflecting back to the surface infrared radiations, i.e. heat, and subsequently increasing the average temperature of the planet. In contrast, fuels originated from biomass, water and solar energy make use of carbon which is already included in the cycle and does not represent an additional source.

1.1 Objective

The following work aims to investigate the reduction process of iron oxides thanks to high temperatures. When furnishing these substances with an adequate level of energy, it is possible to make them release oxygen atoms, thus decreasing their oxidation state. Once this process is completed, the substances can be used for reducing other molecules, such as H_2O or CO_2 (or a mixture of them) to produce H_2 and CO respectively, which can then be used as fuels. The process is included of the larger family of solar chemical looping processes.

The thesis makes use of the previous work that has been developed by the research team of the Energy Department of Politecnico di Torino and its students in terms of chemical looping and thermal reduction of oxygen carriers. Unlike precedent studies, the following thesis aimed to finally apply the prior knowledge to a real situation outside controlled laboratory conditions. The new test bench for the chemical loop has been the solar collector on the Energy Center (faculty of Politecnico di Torino) rooftop. It is constituted of a parabolic dish that concentrates solar radiations in a very small area for reaching high temperatures. The selected energy source is fully renewable and quite abundant from March to September in Turin, Italy, when the research took place.

1.2 Thesis Structure

The work is developed according to the following outline:

- Solar Collector

  The first section after the introduction includes a brief explanation about solar power and the working of devices exploiting the sunlight and its thermal power when concentrated, especially focusing on parabolic dishes.

  Then, the Test Bench used for the experiments is exhaustively described from the technical and operative point of view.

  Together with that, all the actions carried out for the optimization of the focus and set of the machine are listed and explained. These include all the experimental trials and errors for finding the best position of the receiver and the hypothesis made.

Finally, there is an analysis on the recorded data of temperatures correlated to the relative solar irradiance.

- Reduction Reaction

  The following section is relative to the part about the reduction reaction of the chemical looping.

  First, literature review is presented, in order to present the most relevant points about thermal reduction of substances and the subsequent release of oxygen. In particular, the most considered substrates are iron oxides and perovskites. The chance of adding a not inert gas, like methane to the reaction is considered, in order to decrease the temperature required.

  Results of the experiments are listed and commented.

- Experimental Tests

  Experimental setup, issues encountered and results obtained are described in detail. Starting from the first trial, many changes have been made to the initial setup for quickly overcoming problems and making the reaction happen.

- Simulations

  For obtaining a repeatable experiment, some simulations were performed on COMSOL Multiphysics to approximate the real case. First, temperature distribution was investigated, and second the behaviour of the chemical reaction. All the results were compared with the real data from the previous tests.

- Conclusion

  The most interesting findings are explained and commented.

2

SOLAR COLLECTOR

The Solar Collector represented the key tool in this thesis, as all the activities involved its use, and its well functioning was fundamental for obtaining meaningful results. Therefore, its maintenance, proper use and efficiency have always been central to the work.

2.1 Solar Technology

Solar energy is fundamental for plant and animal life on Earth. All the other sources of renewable energies (except from tidal and geothermal) are its final consequences. The Sun is a celestial body made up of hot gases in which nucleus nuclear fusion reactions unleash energy in form of electromagnetic waves. Their wavelength increases from the center to the outer surface, where they are emitted in a spectrum similar to the one of a black body of 5777 K. At the outer surface of the Earth's atmosphere the sun energy arrives with a power of around 1367 W/m^2. This value is the integral of the spectrum of solar radiation [3]. In fact, the level of radiation is not the same for every wavelength, but distributed following a characteristic curve. It can vary of around 3% due to Sun-Earth distance [3]. Of course, this value is lower on the Earth surface, reaching averagely 800 W/m^2. The value depends on many factors, but it is usually under 1000 W/m^2 [4].

Exploiting this power is possible in different ways. The most interesting one for the thesis' purposes is to concentrate the radiations so that a higher power density can be used for a thermochemical process. Therefore a short review of the main principles of this technology is presented in this section.

2.1.1 Solar collectors

The solar radiation, which has a relatively low density, can be concentrated in small areas for making it more useful by using mirrors oriented in a precise way. There are mainly four kinds of Concentrated Solar Power (CSP) systems: parabolic trough collector, linear Fresnel reflector, parabolic dish systems and solar power towers [3]. Although the layouts of these systems might be different, they can all be rated by the concentration ratio, defined as the ratio between the intensity of the radiation in the focus area and the intensity of ambient direct normal radiation [5]. Parabolic dishes are commonly considered as the most efficient instruments for concentrating solar power and converting into electric or chemical power [6]. They are made up of different subsystems:

- The dish, a paraboloidal shaped concentrator, aimed at focusing the solar flux on a little area, i.e., the focus of the parabola. The reflecting surface is made with metallized glass, plastic film, or anodized aluminium. The dish can have different set-ups, it can be constituted by a single piece, or by several units (as it more often happens for larger systems), in form of petals, squares or circles. Mirrors could theoretically modify the solar spectrum when reflecting sunlight. To avoid this, they are designed to leave untouched the spectrum and avoid power losses [3].

- A receiver, the solar heat exchanger, located in the region where the sunlight is concentrated. It can have many different layouts, depending on the function of the CSP system (whether it has to make a chemical reaction happen, produce electricity through a Stirling engine, etc...), and must be able to sustain very high temperatures, up to 1800° C.

- A receiver support, a sustaining structure that keeps in place the solar heat exchanger. Again, there are different strategies for the same purpose, whether it being a mechanical arm starting from the center of the dish and holding it, or being suspended by an semicircular support, etc.

- A tracking system, able to always direct the solar dish towards the sun, so that the solar radiation will be approximately parallel to the parabola axis. The well functioning of this system is extremely important, as the dish can concentrate the solar power on the geometric focus, only if the solar rays are as perpendicular as possible to the concentrator aperture. As explained later, due to the finite distance between the Earth and the Sun, solar rays are not perfectly parallel, but distributed in a cone. The tracking system is equipped with two motors, one for controlling the tilt, i.d. the zenith, and the other for controlling the azimuth, to always keep the dish in the right position.
- A support structure that holds the dish at a certain height from the ground and allows its rotation around the two axis for tracking the Sun.
- Foundations that anchors the support structure to the ground and hold it still.
- A control unit that enables the user to control and move the paraboloid. It must be equipped with an anemometer, so that the tracking can be stopped in case of extreme wind speed and the dish is brought back to a safe position. The connection with a thermocouple (to be placed in the receiver), allows the control unit to slightly unfocus the system when the temperature exceeds a threshold.

2.1.2 Sun-Earth geometry

The intensity of the Sun radiation, from the perspective of an observer on the Earth surface, depends on many factors: the geographical coordinates (latitude and longitude), the time of the day, and finally, the weather. Although the weather might be more difficult to be foreseen, the sun position in the sky can be predicted with extreme precision, as it is a matter of geometry. Moreover, the Earth-Sun spherical coordinate angles are independent of the observer, but they only are dependent on the time of year and the time of the diurnal cycle (day-night) [7].

The declination angle is the angle between the equatorial plane (i.e. the imaginary plane where the equator lies) and the straight line between the Earth and the Sun. Being the axis around which the planet performs its rotation titled of 23.45° relative to the normal to the revolution plane, the declination angle varies throughout the year. It oscillates between -23.45° on winter solstice and +23.45° on summer solstice, being 0° on equinoxes. Its value can be obtained with the Cooper equation 2.1, where n is the number of the day of the year, starting counting from Jan 1st.

$$\delta = 23.45 sin\left(\frac{360}{365}(284+n)\right) \tag{2.1}$$

The time angle varies during the day and corresponds to the angle between the Sun-Earth line and the meridian passing through the observer. It is considered negative during the morning, null at solar noon, and positive in the afternoon.

$$\omega = \frac{360}{24}(t_{sol} - 15) \tag{2.2}$$

The parameter t_{sol} means that solar time, and not clock time should be used. While clock time is the same in vast areas of the world, more or less close to the same meridian (but not necessarily), solar time depends on the specific longitude the observer is, and on the equation of time, as seen in equation 2.3 [8].

$$t_{sol} = t_{clock} + \frac{\psi_{std} - \psi_{loc}}{15} + \frac{EOT}{60} + \Delta_{DST} \tag{2.3}$$

Where ψ_{std} is the longitude of the meridian the time zone is referred to and ψ_{loc} is the longitude of the specific point where the solar time is calculated. Δt_{EOT} is the Equation of Time, expressed in minutes. In fact, over the year, the length of a day is averagely 24 hours, but varies due to the eccentricity of the Earth's orbit the declination. Being the orbit elliptical, the Earth is closest to the Sun on January 3 and furthest on July 4. Thereby the orbiting speed is faster than the average from about October through March and slower from about April through September [9]. This means that the solar mean time happens to be ahead and behind real solar time of up to 16.3 minutes depending on the moment of the year [10]. A useful formula for calculating the equation of time has been provided by Guedez [8], 2.4.

$$EOT = Acos\left(2\pi\frac{n-1}{365}\right) + Bsin\left(2\pi\frac{n-1}{365}\right) + Ccos\left(4\pi\frac{n-1}{365}\right) + Dsin\left(4\pi\frac{n-1}{365}\right) \tag{2.4}$$

A	0.258
B	-7.416
C	-3.648
D	-9.228

Table 1 – Coefficients of the Equation of time [8].

The coefficients can be found in table 2.1.2. Daily saving time, Δ_{DST} is a complication in relating clock time to solar time. During a variable period that usually goes from the end of March to the end of October (it varies as it is adjusted so that the change happens on weekends) the clock is moved 1 hour later for making a better use of the more abundant sunlight in the northern hemisphere. Nevertheless, not every country is accepting this convention and the beginning and ending date does not coincide everywhere [7].

With these information and the geographical latitude of the observation point, it is now possible to calculate with precision the position assumed by the Sun in the celestial sphere at a given moment. For this purpose, it is necessary to define two more angles, the coordinates which will indisputably indicate every point in the sky: zenith angle and azimuth angle.

The zenith angle is the angle between the straight line connecting the Sun with the observer and the normal to the horizon.

$$\Theta_z = arccos(cos\phi cos\delta cos\omega + sin\phi sin\delta) \tag{2.5}$$

The azimuth angle is defined as the angle between the projection of sun rays on the ground and the geographical south. Similarly to the hour angle, it is negative in the morning and positive in the afternoon.

$$\gamma_s = sgn(\omega)\left|arccos\left(\frac{cos\Theta_z sin\Phi - sin\delta}{sin\Theta_z cos\Phi}\right)\right| \tag{2.6}$$

2.1.3 Solar Dish Geometry

The shape of the concentrating surface is, as already explained in Section 2 a truncated paraboloid, i.e. a 3D surface obtained by the rotation of a parabola around its symmetry axis. The parabola has the geometric property of reflecting all the lines parallel to his axis towards a point, the focus. According to the reflection laws, retrieved from the Fresnel equations:

- The incident ray, the reflected ray and the normal to the reflection surface at the point of the incidence lie on the same plane.
- The angle which the incident ray makes with the normal is equal to the angle which the reflected ray makes to the same normal.
- The reflected ray and the incident ray are on the opposite sides of the normal.

Therefore, the parabola is the geometric curve which normal is always such that in any of its points the normal to the curve divides into two equal parts the angle between the parallel to its axis and the conjunction focus-point. Unfortunately, being the Sun positioned at a finite distance from the Earth, its rays are not perfectly parallel, but diffused in a conical shape with a half-angle of 4.65 mrad of aperture. Therefore, even with a perfect paraboloid concentrator it is physically impossible to concentrate all the power in a single point, but rather into an area [11]. In fact, light coming as a cone will be reflected into another cone.

The geometric concentration ratio is defined as:

$$C_g = \frac{A_C}{A_R} \tag{2.7}$$

Theoretically, its value could be increased indefinitely according to this definition. Nevertheless, there are some thermodynamic limits. The solar radiation has to be considered incident on a device inside which it is concentrated without losses. The small surface A_R is considered to have ideal black-body characteristics at temperature T_R. The energy equilibrium is presented in the formula:

$$\sigma T_S^4 A_C sin^2 = \sigma T_R^4 A_R \tag{2.8}$$

It must be remembered that, at the equilibrium, the surface of the receiver can not be at a higher temperature than the Sun without breaking the Second Law of Thermodynamics, so:

$$T_R \leq T_S$$

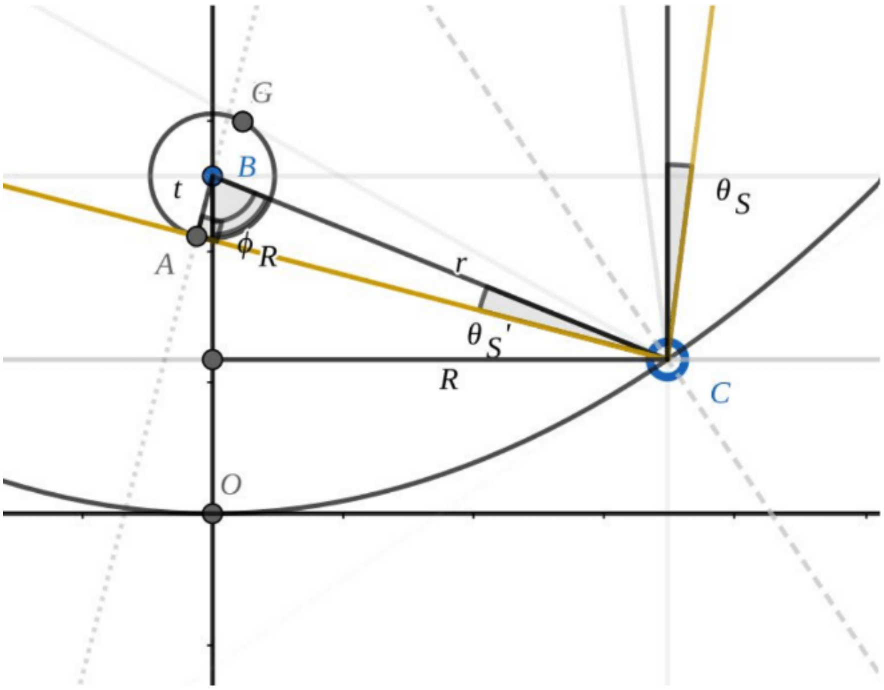

Figure 1 – Scheme of the geometry of the system [11].

The upper bound to the Concentration ratio, for concentration onto a point is:

$$C_{g,pt} = \frac{A_C}{A_R} = \frac{1}{sin^2\Theta} \tag{2.9}$$

Considering a third surface, A_{out}, the same logic applies:

$$\sigma T_R^4 A_R = \sigma T_S^4 A_{out} sin^2\Phi \tag{2.10}$$

Where Φ is the acceptance angle of the receiver. It follows:

$$C_{g,pt} = \frac{A_C}{A_R} = \frac{sin^2\Phi}{sin^2\Theta} \tag{2.11}$$

This value is maximum when Φ is equal to 90°.

Concentrators face another issue, which is the optical limit, further decreasing the concentration ratio under the thermodynamic limit. In the case of a parabolic dish with spherical aperture, considering that:

$$t = rsin\theta_S = \frac{Rsin\Theta_S}{sin\Phi_R} \tag{2.12}$$

as it can be seen in figure 1. The concentration ratio is:

$$C_o = \frac{\pi R^2}{4\pi t^2} \approx \frac{sin^2\Phi_R}{4sin^2\Theta_S} \tag{2.13}$$

The optical limit is the maximum, respecting to the acceptance angle, for:

$$\frac{dC_g}{d\Phi_R} = \frac{2sin\Phi_R cos\Phi_R}{4sin^2\Theta_S} = \frac{sin2\Phi_R}{4sin^2\Theta_S} = 0 \tag{2.14}$$

$$\Phi_R = \frac{\pi}{4}$$

Therefore, the maximum concentration ratio for the parabolic dish is obtained for an acceptance angle of 45°, and is[11]:

$$C_g, max = \frac{1}{4sin^2\Theta_S} \approx 11600$$

This value is lower than the geometric punctual ratio, as it takes into account the fact that the solar rays will be concentrated on the Sun image, rather than in a point. This number is only valid for ideal mirrors and the specified geometry. Real systems with paraboloid mirrors can reach concentration rates of about 2000-6000 [12]. This is due to several phenomena:

- Optical losses: mirrors might have imperfections from the microscopic point of view (irregularities, non-smooth surfaces), or from the macroscopic point of view (aberration of reflection angle) thus reflection of sun rays can happen towards a wrong direction;
- Material imperfection: the substance used for the mirrors will likely not have a reflection coefficient of 1 as hypothesized until now, but lower than 1.

With these considerations, it is possible to estimate the maximum temperature the absorber is capable to reach. This happens when the absorber is in thermal equilibrium with the surrounding environment, i.e.the radiant power emitted by the absorber equals the received power on the collector aperture as shown in equation 2.15.

$$P_{ab} = A_{AB}\sigma T_{ab}^4 = \dot{Q}_{ap}\sigma T_S^4 \frac{r_S^2}{r_{SE}^2} \tag{2.15}$$

As Θ_S is quite small, it can be approximated $\Theta_S \approx tan\Theta_S = 2r_S/r_{SE}$ and therefore $\Theta_S^2/4 = r_S^2/r_{SE}^2$ and considering equation 2.7,

$$A_{AB}T_{AB}^4 = A_{AP}T_S^4 \frac{1}{C_{max}} \tag{2.16}$$

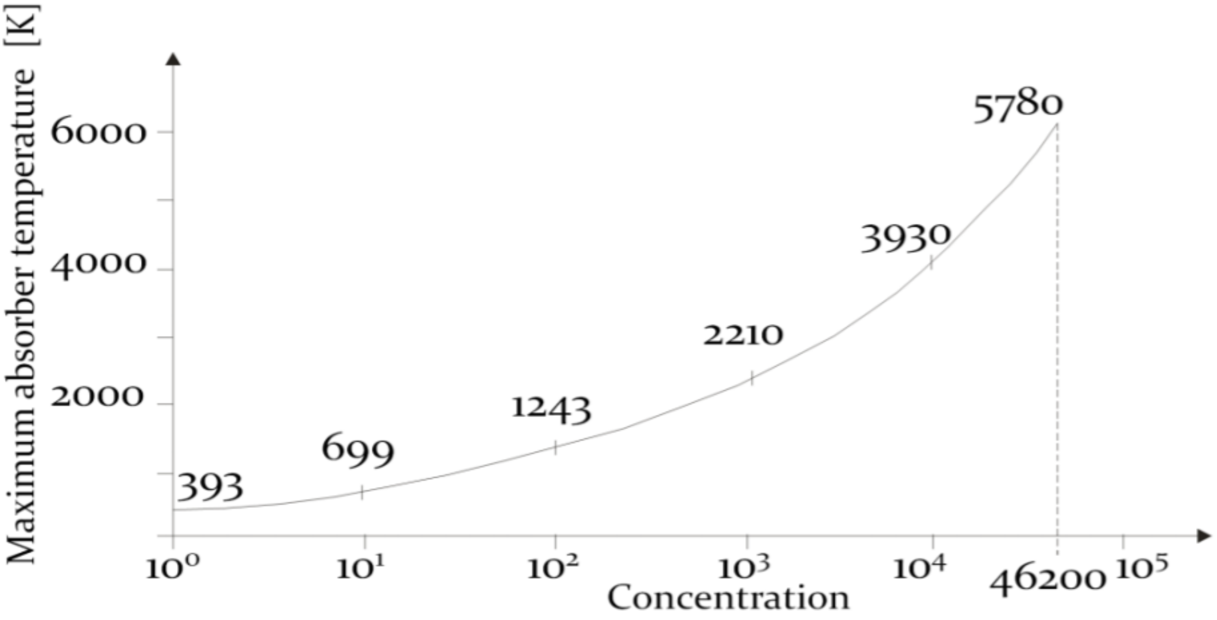

Figure 2 – Plotting of equation 2.17 [12].

Therefore, the receiver temperature can be calculated with equation 2.17

$$T_{AB} = T_S(\frac{C}{C_{max}})^{\frac{1}{4}} \tag{2.17}$$

Fig. 2 shows the maximum theoretical temperature the absorber could reach in an ideal condition from the thermal point of view. It can be seen that, for the optical limit of 11600, the temperature might be even above 3900 K. Looking at the more realistic value of concentration ratio between 2000 and 6000, the temperature might reach 2000 K. Unluckily, this is once again an approximation, as equation 2.17 does not consider a few important phenomena in thermodynamics:

- Nor the Sun, neither the absorber are black bodies, it is just an approximation. Moreover, the solar radiation is even further from the black body radiation spectrum after it has travelled through the atmosphere.
- Conduction and convection thermal losses are not considered in the power balance, but only radiation losses. Nevertheless, the high-temperature difference can cause not negligible losses, especially in the case of a windy day or very low ambient temperature,

- The solar irradiation is not constant throughout the day and the year, but is afflicted by adverse weather conditions.
- There might be shadings and sun light might not be able to reach the reflective mirror because of obstacles.

For these reasons, the absorber might not even reach the maximum temperature for the lower range of concentration ratios.

Regarding to the specific geometry of the solar dish, there are two fundamental parameters connected to its shape: the *focal distance* f and the *rim angle* Φ_R as shown in 3.
The focal distance is the distance between the focus and the vertex. The rim angle is the angle between the axis of the dish and the straight line passing through the edge of the mirror and the focus and it can be calculated with the equation 2.18. It immediately gives an indication about the geometry of the system: high values of Φ_R belong to flatter concentrators, while lower values correspond to more convex concentrators [11]. The parameter y_R, the depth of the solar dish, can be calculated with goniometric considerations 2.19 or with the parametric formula 2.20

$$.tan\Phi_R = \frac{R}{f - y_R} = \frac{4fR}{4f^2 - R^2} \tag{2.18}$$

$$y_R = f - Rtan\Phi_R \tag{2.19}$$

$$y_r = \frac{D_{con}}{16f} \tag{2.20}$$

The dimension of the diameter of the focal area can be estimated with the formula 2.21 [13]

$$d_f = \frac{f\Theta}{cos\Phi_R(cos\Phi_R)} \tag{2.21}$$

2.1.4 Clear Sky Index and Air Mass

As previously mentioned, the solar spectrum at ground level is influenced by different atmospheric conditions: water vapor, ozone, carbon dioxide, and clouds among others. Clear sky conditions means, in meteorological terms, when cloud coverage is totally

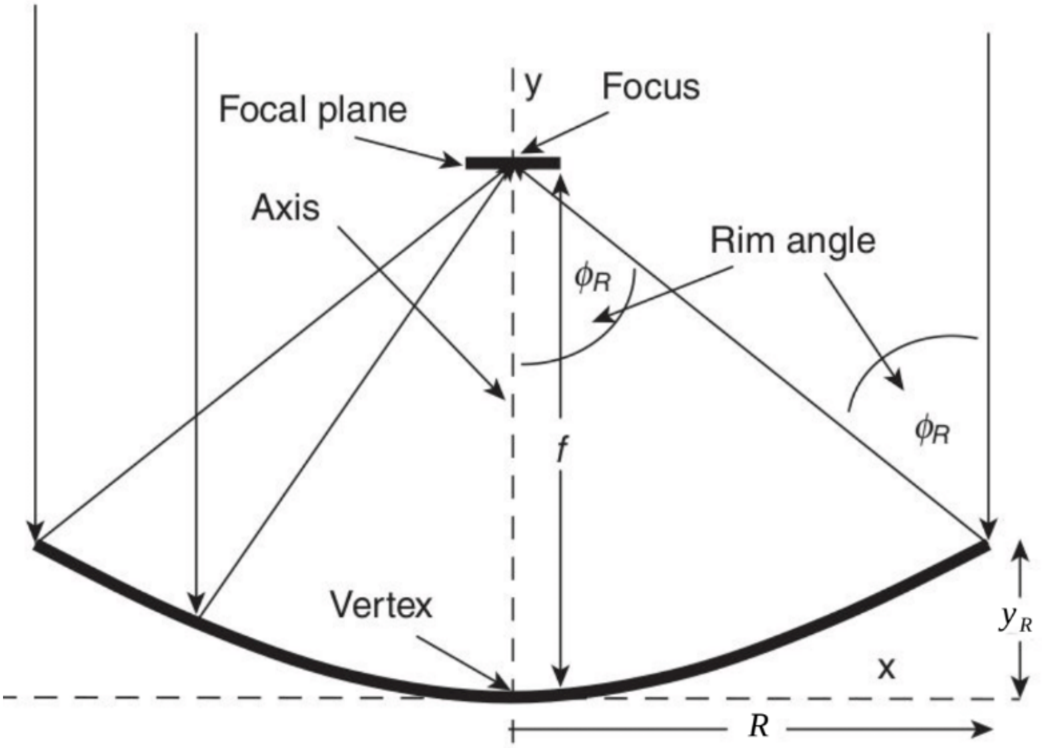

Figure 3 – Bidimensional scheme of the paraboloid concentrator geometry [13].

absent (0 over 8 octans of coverage) [14]. Under this condition, the main factor that affects the spectral profile during the day and the year is the air mass (AM). The air mass is referred to the optical path that sun rays (i.e., direct solar radiation) have to do through the atmosphere. The longer it is, the more attenuated the radiation reaches the ground, due to the interaction with matter [3]. Air mass can be easily calculated without any measurement, as it only is a function of geographical location and time, and it is defined as a function of the solar zenith angle 2.22. Figure 4 shows the effect of higher values of AM on the solar spectrum. It looks clear how a longer optical path negatively influence the power of the radiation for every wavelength.

$$AM = \frac{1}{\Theta_z} \tag{2.22}$$

Perez et al. [15] developed several models to predict short time-step solar energy and daylight availability quantities needed by energy system. They studied the influences of different parameters on global, diffuse and direct radiation, by collecting data in different locations in the US and Europe. As for a solar concentrator the most important solar radiation component is the beam one, the results of the relative model are reported

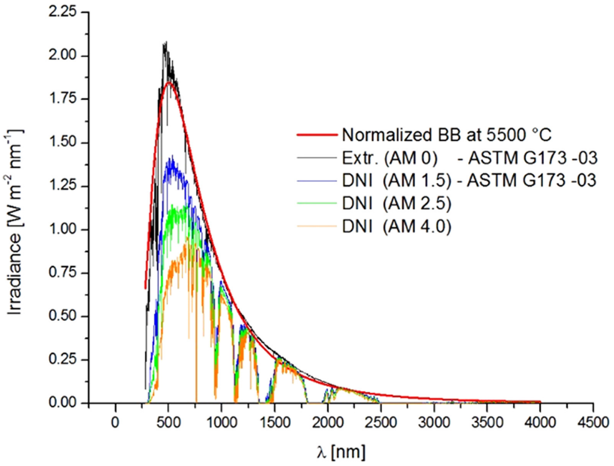

Figure 4 – Direct Normal Irradiance for different Air Mass values [3].

briefly. The models are all relating to Luminous efficacy, a measure in terms of lumens per watt that bounds different solar irradiance components to their photopic equivalent, i.e. illuminance. Illuminance can be defined as the yield of a given light source when its spectrum is weighted by the transfer function of the human eye [16]. Figure 5 shows the polynomial surface that best fits the empirical data recorded in the selected locations. In particular, the efficacy of direct luminous efficacy is plotted against clear sky index and temperature of the dew point. The latter is relevant in this case, as it is a measure of the amount of dispersed moisture. Luminous efficacy decreases with increasing dew point temperature for intermediate conditions, probably because of enhanced aerosol scattering, while it increases for clear conditions, because of increased absorption in the infrared. It must be noticed that beam efficacy values for extremely overcast skies were not plotted as direct irradiance is almost null when the sky is extremely cloudy. The highest values of efficacy are found for very clear skies and high dew point temperatures.

2.2 Test Bench Description

As already mentioned, the main test bench was represented by the Solar Collector on the rooftop of the Energy Center. The machinery has been designed, constructed and finally installed on the roof by El.Ma., an Italian industrial company from Trento [17].

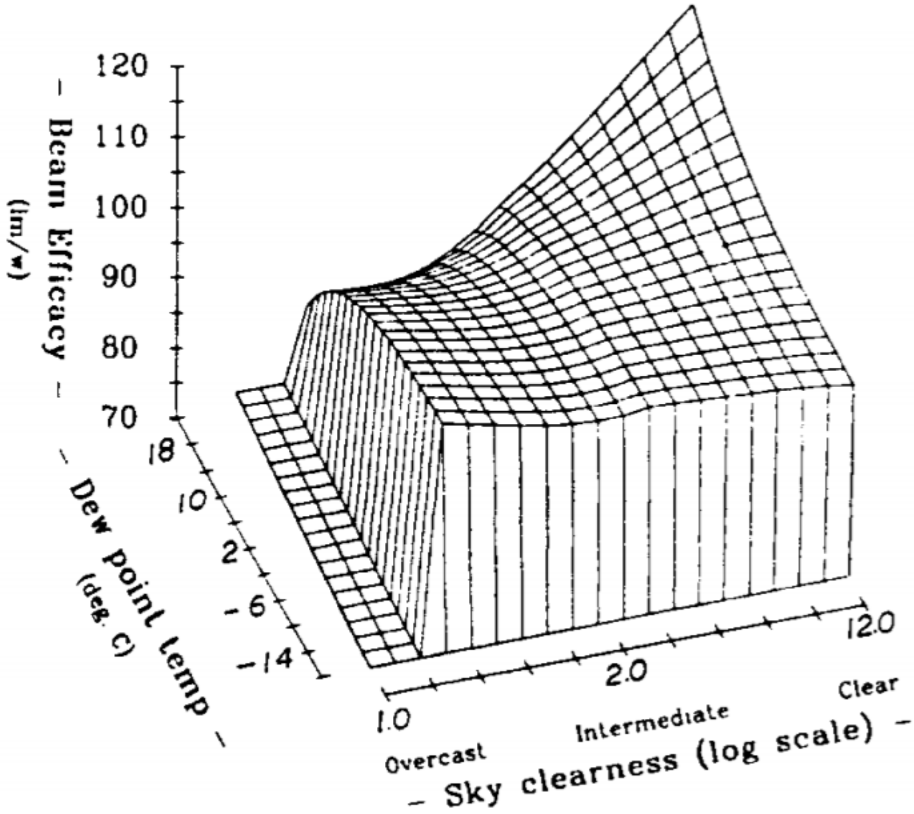

Figure 5 – Best fit polynomial surface showing the function direct luminous efficacy of sky clearness, surface dew point temperature [15].

Considering a normal irradiance of 800 W/m^2 and a captating surface of 4.5 m^2, in optimal conditions, the rated power is 2.8 kW, and it can reach up to 1800°C, according to [18].

2.2.1 Solar Concentrator

The reflecting surface is constituted by the conjunction of 6 petals covered by a plastic reflecting film which is pasted on them. The units are fixed together along their long side and to the structure in the center. In this point, there is no reflecting surface, as that is where the mechanic arm holding the receiver support is mounted. It consists of a large and short U shaped iron arm that sustains the receiver support as it can be noticed in the mechanical drawing in fig. 8. In fact, on the horizontal part opposite to the solar dish, two aluminium joints can swipe and move the receiver closer or further from the

Figure 6 – The Solar dish concentrator by El.Ma. installed on the Energy Center rooftop.

vertex of the paraboloid. Moreover, the support can also be raised or lowered thanks to two vertical aluminium joints, as it can be noticed from fig. 7. The two vertical joints are kept at a stable distance of 20 cm by a horizontal aluminium joint of the same type on the bottom. They hold two iron U shaped supports, where the receiver is placed.

The initial receiver consists of a pipe made of alumina, Al_2O_3, connected to two thinner tubes at the edges. The pipe is 22 cm long (so that part of it goes inside the supports at the tips). It has an external diameter of around 18.06 mm, an internal diameter of around 14.02 mm and is around 2.02 mm thick. The dimensions can slightly vary from one piece to another one, and sometimes even along the same piece.

On one side, the pipe holder is equipped with a Q-type thermocouple of 10 cm length and 6 mm diameter, so that, if mounted correctly, reaches the middle of the pipe without impeding gas flow. The electric connection of the thermocouple is protected by a plastic sleeve and a metallic plate. The small tubes connected to the edges and the cable run inside the mechanical arm, the supporting pillar and reach the control cabinet by

Figure 7 – The picture shows how the support structure, at the end of the mechanical arm is made.

passing inside a duct installed on the floor.

The reflecting surface has a diameter of 2370 mm, and the depth of the dish has been measured to be 370 mm. Fig. 8 indicates the dimensions of the mechanical arm holding the receiver support (which is not represented) and shows where the focus is located. The focal distance is 958 mm measured starting from the plate where the support is connected. The focus lies on the central axis of the parabola. With these information and equation 2.18 it is possible to calculate the rim angle, which is found to be of 61.89°. It has to be noted that the rim angle is higher than 45°, a value which is considered to be output the best efficiency and performance [13]. Therefore, by applying equation 2.13, the theoretical concentration ratio is ≈ 8013. The diameter of the focal point is obtained by applying equation 2.21, 6.41 mm. A summary of the principal dimensions of the solar concentrator can be found in table 2.2.1.

The machine is also equipped with a control unit through which it is possible to modify

Table 2 – Dimensions of the solar concentrator on Energy Center Rooftop.

Simbol	Description	Value	U.m.	Method
D_c	Diameter of the dish	2370	mm	measured
f	Focal distance	958	mm	retrieved from eq. 8
y_R	Depth	370	mm	measured
Φ_R	Rim angle	61.89	°	calculated with 2.18
C_o	Optical concentration ratio	8013	-	calculated with 2.13
d_f	Diameter of the focal point	6.41	mm	calculated with 2.21
l	Lenght of the receiver (space between the holders)	200	mm	measured
d_{in}	Internal diameter of the receiver	14.02	mm	measured
d_{out}	External diameter of the receiver	18.06	mm	measured
t	thickness of the wall	2.02	mm	measured
A	Area of the concentrator	4.5	m^2	retrieved from [18]
P	Power of the concentrator	2.8	kW	retrieved from [18]

the settings and orient with the desired coordination. The collector can work in two modes:

- Automatic, when it automatically tracks the sun basing the time set;
- Manual, if the user wants to decide the coordinates for the orientation. In this mode, it is possible to edit the parameters that regulate the solar tracking. If wanted, it is possible to insert offsets for the azimuth and elevation tracking, choose the night position and the kind of tracking, whether the system should update its position on a temporal or angular basis.

2.2.2 Control Cabinet

The control cabinet is reached by the end of the thin pipes connected to the receiver and hosts the tanks of the gases used for the tests. Moreover, it contains the vacuum pump, used for ejecting all the air that inevitably enters the system between one test and another one.

The control cabinet also hosts an additional control system by Siemens, with different channels for connecting the thermocouples eventually used and starting the pump for the simulations. It is equipped with a display for showing the instant data and it is connected to a cloud system which saves and stores the data.

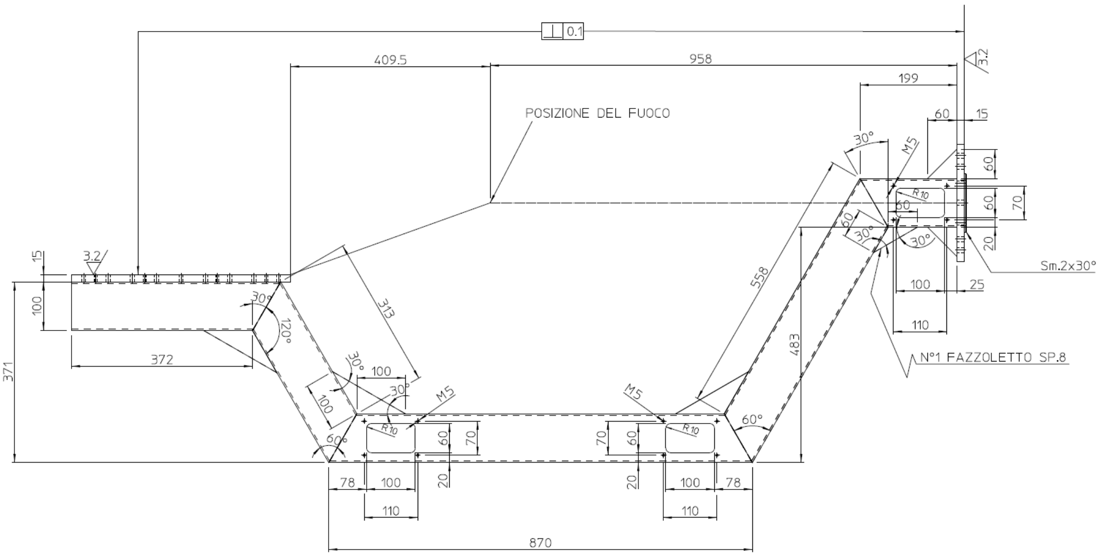

Figure 8 – Technical drawing of the support with the indication of the position of the focus [17].

2.3 Optimization of the focus

The first part of the lab work was mainly focused on the preparation of the test-bench and of the optimal conditions for the happening of the reduction reaction. All the changes to the original setup of the solar dish were made to increase as much as possible the temperature measured by the thermocouple inside the receiver tube.

In fact, by modifying the position of the pipe, it is possible to change the quantity of heat flux that is concentrated on the receiver. The main goal was to find theoretically or empirically the focus position and place the tube as closer as possible to that point. This would theoretically constitute the best situation, when the maximum temperature can be reached. In fact, if the pipe is placed so that the focus hits in the middle.

2.3.1 Thermocouple and support structure removal

The initial setup of the collector was using two additional thermocouples for having more accurate information on the temperature distribution along the tube. Unfortunately, they needed an iron alloy structure as a support which was later found responsible for the low temperatures reached by the reactor. According to a COMSOL simulation,

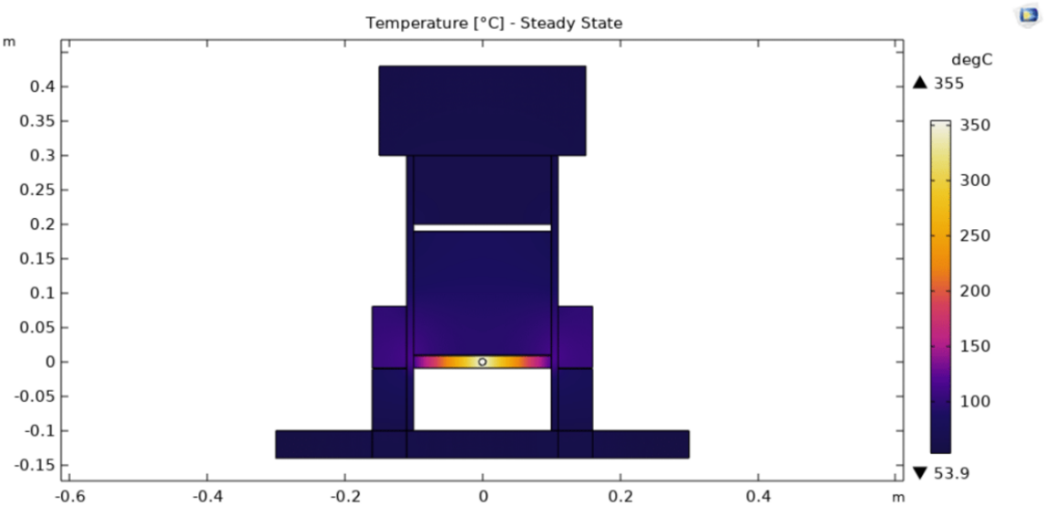

Figure 9 – Initial setup of the test-bench with the iron alloy structure holding the additional thermocouples and the temperature distribution [19].

the structure was responsible for excessive heat losses due to conduction and convection [19]. Fig. 9 shows how the system was built and the temperature distribution over the structure. Therefore, the first change implemented was removing this part and the additional thermocouple, thus leaving the alumina pipe alone with its iron support and the original temperature sensor.

2.3.2 Iterative Method for finding the focus

Although an initial increase in the temperature has been noticed, up to 150°-200° C, it clearly was not enough for the reduction. Therefore, a more precise research of the focus has started. In fact, the information explained in section 2.2.1 were not immediately available but had to be investigated deeply. The initial absence of any guess about the real focal distance and the rim angle made it difficult to find the focus.

The methodology applied for finding the focus consisted into several trials and errors, based on initial guessing. The first tentative has been made based on an assumption found in the literature [13] that the best value for the rim angle is 45°. Having a diameter of 2.37 m, the focal distance would be around 1.55 m. In fact, if Φ_R is 45°, then radius of the paraboloid aperture has to be equal to the distance between the focus and the plane cutting the paraboloid on its aperture. The focal distance is made up by the sum of this plus the depth of the paraboloid (37 cm, see 2.2.1). Nevertheless, the receiver put at this distance (the height was not modified) recorded much lower temperatures, as the thermocouples was out of scale. Moreover, the illuminated area on the pipe and the support was clearly wider than before, meaning that the new position was even further from the initial one. As a conclusion, it has been demonstrated that the guess of 45° for the rim angle was not correct.

Subsequently, the following guess for the focal distance has been made basing on the uncertain information that f were supposed to be around 90 cm, diffused by the constructor El.Ma., but still to be validated. The receiver was placed closer to the dish, at a distance of 102 cm from the metallic plate at the center of the mirrors. Moreover, the support was lowered of 4 cm by changing the position of the aluminium rail. The new setting caused an immediate improvement in the temperature, reaching 230° at 14:40 of the 8th of March 2021. For understanding in an empirical way whether this position was closer before or beyond the focus (from the dish point of view), an opaque plaque has been used for partially shadowing the mirror. The shadow has been seen on the receiver and its support on the opposite side, meaning that the receiver was further from the paraboloid than the real focus. In fact, solar rays are concentrated in the focus, but the light beam reopens beyond it, thus flipping the images. Therefore, the distance has been decreased in the following trials as long as the temperature kept increasing. At 96 cm, it became more difficult to distinguish where the shadow was projected, meaning that probably the focus was very close. Nevertheless, the little increase in temperature could have indicated that the focus was already past. So, it has been decided to try making a step back and check if between 98 and 96 cm there was a point with an even higher temperature. Unluckily, a cloud covered the sun for some minutes, causing a sharp decrease in temperature. The recorded temperature happened to be lower than both the one recorded at 98 cm and 96 cm. This quite senseless finding can be probably be explicated by the time of the measurement. In fact, at around 4 pm, the solar irradiation starts decreasing quite quickly at the beginning of March. Table 3 contains the full list of

Table 3 – Summary of measurements recorded when moving the receiver between 102 and 96 cm.

Distance	Temperature	Time	Getting	Notes
102 cm	230° C	14:40	closer	Flipped shading
100 cm	354° C	14:54	closer	Flipped shading
98 cm	371° C	15:08	closer	Flipped shading
96 cm	383.6° C	15:23	closer	Here it starts being difficult to understand where the shadow is
97 cm	346°C	15:45	further	A cloud causes an accidental sudden decrease of T for some min

the positions and the recorded temperatures.

The alumina pipe was then left at 96 cm of distance and the system was left operating for some days. Among the recorded temperatures, the maximum, 582.3° C, was measured o the 13 March at 13:20 with an irradiance of 661.8 W/m^2. Anyway the temperature did not reach the same level every day, and kept itself lower even on sunnier days with a higher irradiance. This might be due to the strong winds that have been recorded on the 14th and 15th of March, with peaks over 10 m/s. Fig. 10 shows the median value of the temperature between the 10th and the 16th and the range among the second and the third quartiles. On the 17th, the alumina pipe was found broken by a sharp crack and separated into two parts. Unluckily, this inconvenience kept happening many times after changing the old piece with a new one. This might be explained by the way of cutting that has been applied to the pipes that produces microscopic cracks in the material. In fact, a long tube was divided into more pieces with a diamond wheel cutter. Being a ceramic insulating material, alumina can stand very well high temperatures, but even the presence of scratches on the surface can cause the failure of the material. In fact, evidence shows that the measured strength of a ceramic is approximately 100 times lower than the theoretical strength based on an interatomic bond. This is due to fracture mechanics theory which states that failure happens from the deepest flaw [20]. Therefore, it became evident it was necessary to find an alternative way of cutting the pipes for not compromising their performances. The best option was found into directly ordering new pipes of the right length from the manufacturer.

Nevertheless, new trials were made for better understanding the position of the focus,

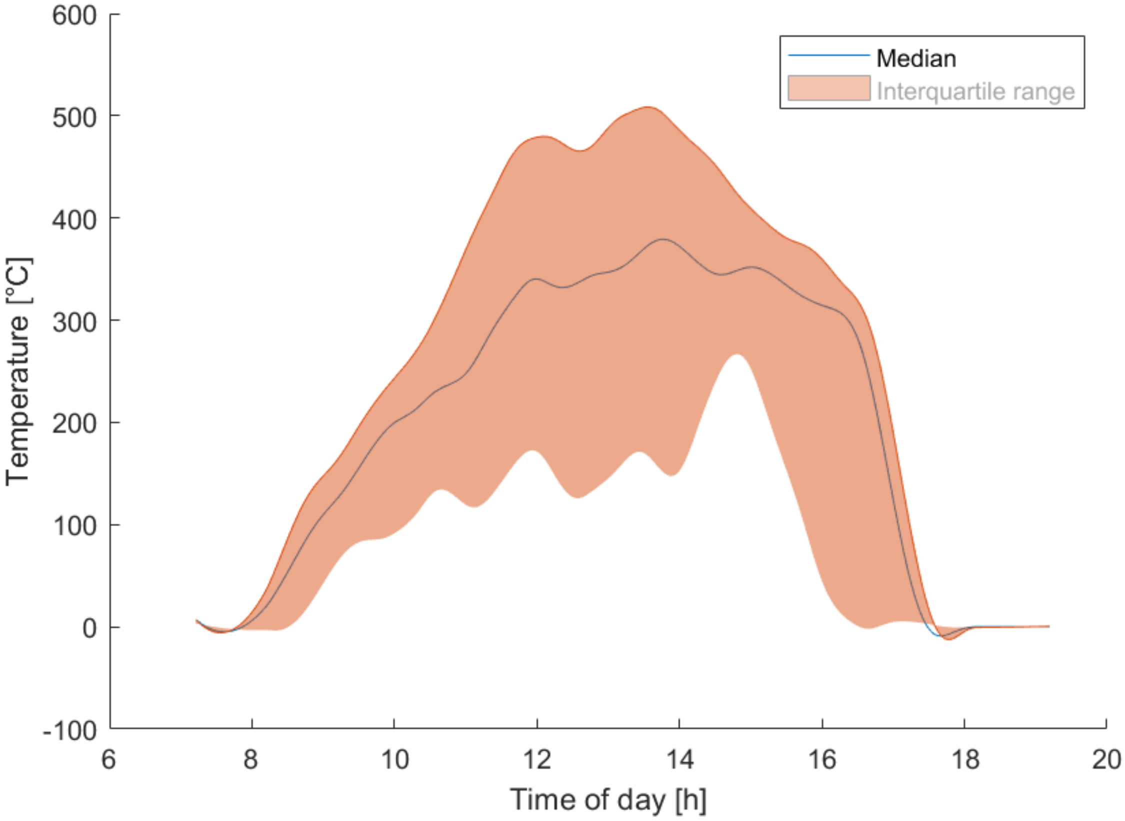

Figure 10 – Average temperatures recorded in the solar collector receiver between the 10th and the 16th of March. Orange area represents the range between the second and third quartiles.

Table 4 – Summary of measurements recorded when moving the receiver around 100 cm.

Distance	Temperature	Time	Getting	Notes
100	290° C	11:35	-	Shade not noticeable
96	228° C	11:56	closer	Same side shading
101.3	302.8° C	12:06	further	Shade not noticeable
104	-	12:24	further	Temp does not increase, the illuminated area is very big

starting from 100 cm from the metallic plate at the center of the mirrors. Unluckily, tests reported in table 4 were not satisfactory as it was not possible to reach high temperatures or quick increases when putting the concentrator into work (meaning that the selected position was hit by a large flux). Probably due to a different time of the day the tests were effectuated, the distance of 96 cm was not anymore the best one. This was meaning none of the selected set-ups corresponded to the real focus. More accurate measurements and the use of a leveling bubble revealed the axis of the parabola was passing above the tested positions. Therefore, the support was remounted at its initial height, 4 cm above the last set up. As soon as the manufacturer transmitted the technical drawings in fig. 8, the receiver (now back again on the axis of the concentrator) was placed at 95.8 cm. The immediate improvements in the temperature gave evidence that the focus was effectively situated around 96 cm from the metallic plate. The exactness of the position was also highlighted from the little illuminated area on the support, mainly focused on the pipe.

2.3.3 Tilt Offset

Nevertheless, further observation with the leveling bubble gave evidence that the arm was not perfectly horizontal when in the reset position, but slightly inclined. To quickly fix the problem, it was necessary to operate on the concentrator setting "Horizon Offset". The description of that voice on the user manual is "departure angle from horizon, expressed in degrees". For the whole duration of the tests, the setting has been set to -1.00°. To find the optimal value for reaching a higher temperature, several trials have been made, starting from a value of 0. Unluckily, it is not possible to modify this parameter while operating, but every time something has to be changed, it is necessary to reset the machine and switch to manual mode. This causes a loss of the state of temperature reached every time. Results can be found in table 5. Although the temperatures reached started decreasing after 14:40, evidence confirmed the best point was at -2.00°.

The system was left operating with this set for the following days and more data was acquired during April. Fig. 11 has been obtained with the same procedure as for fig. 10 and plotted over solar time. It can be immediately seen how the curve in April is averagely higher than in March. This might be due to both the higher solar radiation in this month and to the better set-up of the receiver. In particular, temperatures exceeded 700° C on April 13th, reaching around 734° C with a solar irradiance of 825 W/m^2. This finally is a suitable range for the happening of aided thermal reduction of the powders.

Table 5 – Results of the tests editing the horizon offset in the machine settings.

Offset	Temperature	Time	Notes
0.00°	-	14:01	T does not rise
-0.50°	-	14:06	T does not rise
-1.00°	250° C	14:10	Slow temperature growth
-1.50°	524° C	14:19	
-2.00°	690° C	14:25	Rapid growth of T
-2.50°	647° C	14:37	
-2.25°	611° C	14:48	Sky is less clear
-2.00°	556° C	14:58	Sky is less clear

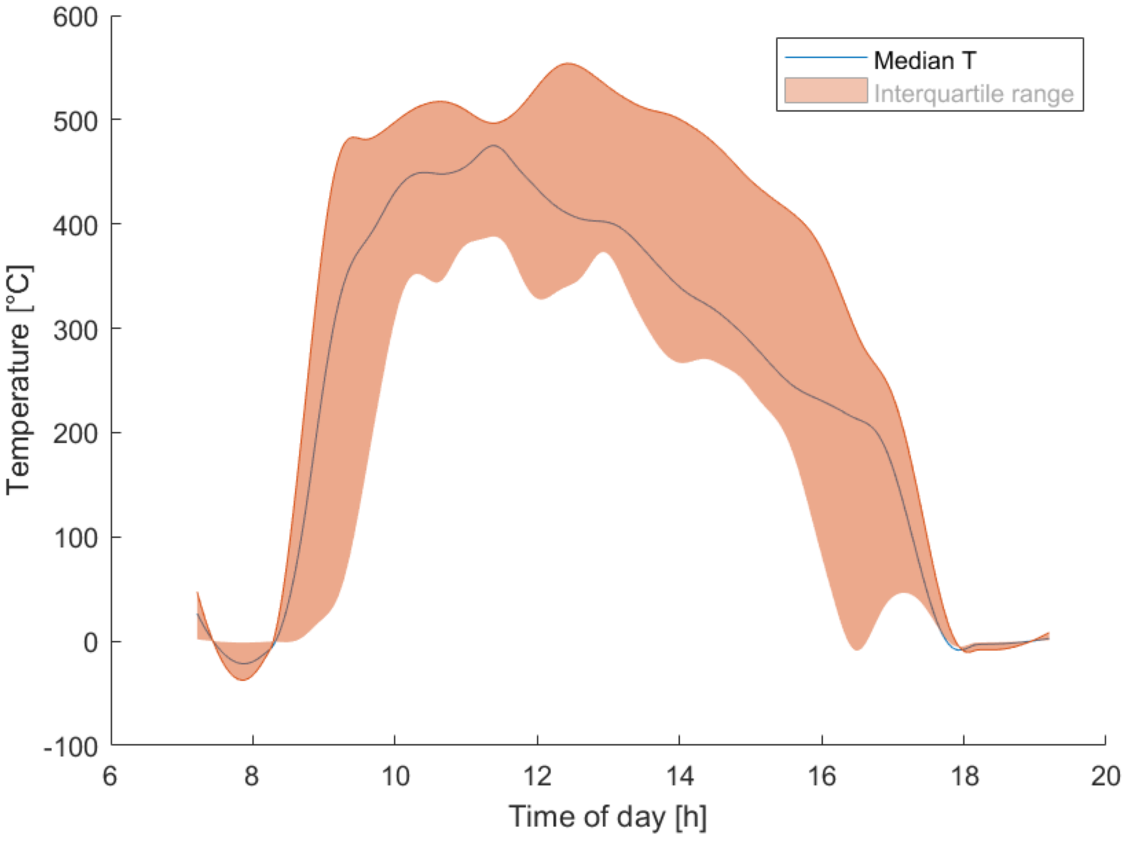

Figure 11 – Average temperatures recorded in the solar collector receiver between the 2nd and the 13th of April. Orange area represents the range between the second and third quartiles.

Table 6 – Info on the thermo-camera used in the optimization tests

Brand	Optris
Model	PI 450 i
Range	-20 - 900°C -20 - 100°C 0 - 250°C 150°C - 900°C
Spectrum	8-14
Frequency	80 Hz or 27 Hz
Optics	029
FOV	29°

2.3.4 Infrared Camera

After this optimisation process, another experiment has been done to understand the quality of the focusing operated on the receiver. The alumina cylinder was studied using an infrared camera by Optris. The model of the instrument used was PI 450 i. The suitable temperature ranges are -20°C - 900 °C, -20 - 100°C, 0 - 250°C, 150 - 900°C (the one used for the test). Other data about the performances of the camera are found in table 6. Although this kind of instrument is not extremely precise when it is about getting an exact measure of temperature, it can be useful for studying temperature differences. In fact, cameras like the one used are very sensitive to temperature variations and can give a good indication about the presence of hot spots and thermal gradients.

The camera has been pointed to the receiver while the concentrator was tracking the Sun. The objective was to identify the presence of the point where the majority of the solar flux (in a perfectly ideal condition, the whole flux) was converging. The camera was assumed to be the right instrument for the purpose as it would only have been necessary to detect the presence of areas with a high-temperature difference than the rest. As hypothesized, images extracted from the camera showed a little area which was extremely hotter than the rest. Due to the high thermal resistance and low thermal conductivity of alumina, the heat concentrated on the focus is not transferred to the rest of the pipe, which remains quite cold. This cause a high-temperature difference that is easily detectable. Fig. 12 clearly shows there is an extremely concentrated hot spot that reaches a temperature around 663°C. The shape looks very elliptical, due to the point of view of the camera, which was not placed at the center of the paraboloid, but on a side of the dish, in order not to catch direct sun rays.

The experiment gave evidence the focusing is quite optimised as there is a very limited

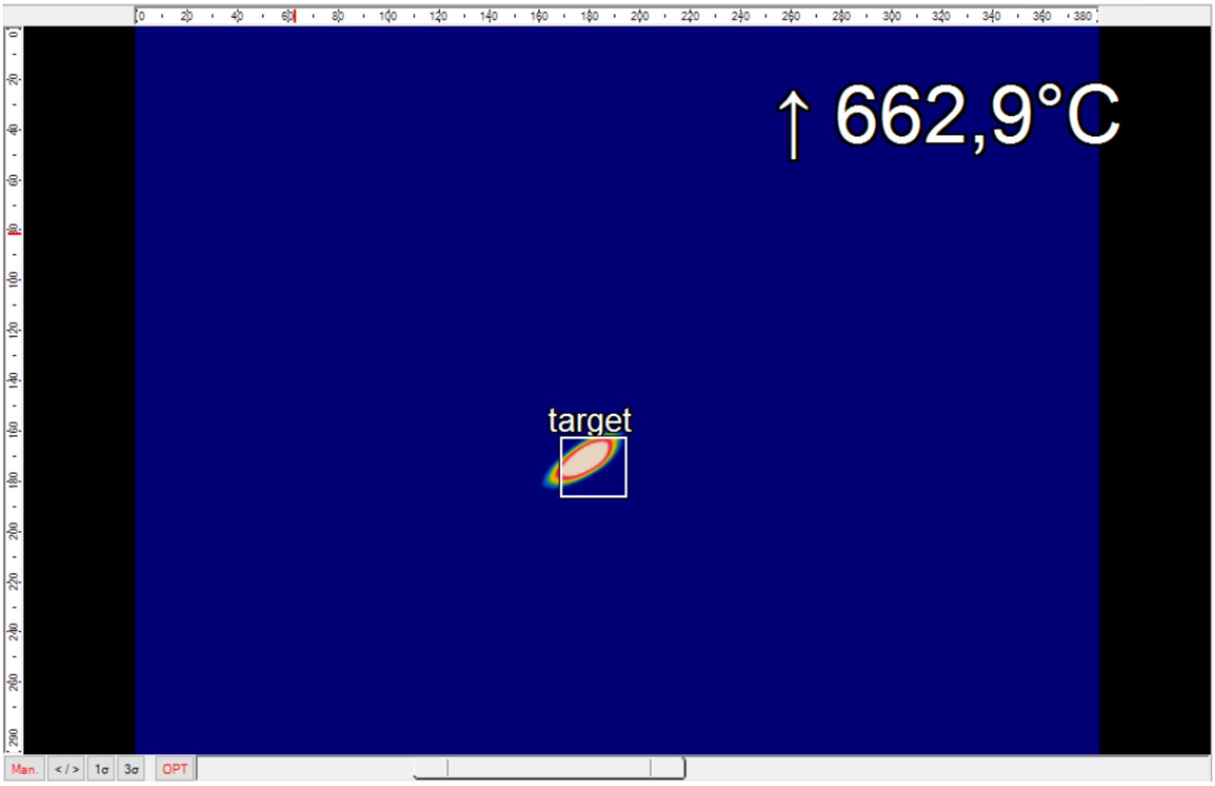

Figure 12 – Image extracted from the infrared camera showing the focus.

area receiving the majority of the heat flux, thus reaching high temperatures. Moreover, it showed how little the area with high temperature is, which most probably is almost coincident with the focal area, which diameter has been calculated with equation 2.21 (6.41 mm).

3

REDUCTION REACTION

Reduction is any kind of chemical reaction in which the number of electrons associated to a chemical species is increased. Consequently, another substance has to release the electrons and be oxidized. Reduction and oxidation always have to happen in pairs, causing redox (oxidation-reduction) reactions. Another way of describing the reaction is related to oxygen exchange. In fact, when a substance is reduced, it loses oxygen, while, when reduced, it gains oxygen. This transfer is central to the phenomenon that is being studied in the thesis.
Linked to that, there is the oxidation state (or oxidation number), that is the degree of oxidation (loss of electrons) of an atom in a chemical compound. An example can be done by looking at the various oxides that are produced when pure iron (a multivalent transition metal) is mixed with oxygen:

- Hematite, i.e. Fe_2O_3, is the iron oxide where iron is at the highest state of oxidation, 3 (Fe^{3+});
- Magnetite, i.e. Fe_3O_4, with a state of oxidation of 2.6 (being it a mixture of Fe^{2+} and Fe^{3+});
- Wüstite, i.e. FeO instead is the iron oxide at the lowest state of oxidation, 2 (Fe^{2+}) [21].

It is possible to switch from one to another thanks to the release or gain of oxygen (and consequent gain or release of electrons), which can happen thanks to several mechanisms. Moreover, it is possible to separate the moments in which the redox reactions happen for making a better use of the reducing power. This could be done through the use of chemical looping, a process in which an oxygen carrier is first reduced for making it lose part of its oxygen atoms (thanks to an external source of energy, such as the Sun), and then is oxidized by making it absorb oxygen from another substance, such as H_2O or CO_2 for producing H_2 or CO. Producing such fuels from water or carbon dioxide through the use of only solar concentrated power can be extremely interesting for reducing the dependency on other non-renewable fuels. In fact, alternative ways for splitting this molecule through solar concentrated power require extremely high temperature. Gibbs free energy for the reaction 3.1 reaches zero (thus happen spontaneously) at 4300 K atmospheric pressure [22].

$$H_2O \rightarrow H_2 + \frac{1}{2}O_2 \tag{3.1}$$

Similarly, the Gibbs free energy for the reaction 3.2 reaches zero for lower values of temperature, around 1000 K. Nevertheless, to reduce it completely to C and O_2 temperature required is much higher [23].

$$CO_2 \rightarrow CO + \frac{1}{2}O_2 \tag{3.2}$$

Therefore, they might require extreme conditions which are not easily reachable. The use of specific metal oxides through chemical looping instead can decrease such temperatures and make the production more feasible.

This thesis focuses mainly on the first step of the chemical looping process, i.e. the reduction of the oxygen carrier. It consists of a high-temperature endothermic reaction in which a metal oxide is reduced upon heating with concentrated solar energy. Nevertheless, the typical reduction temperature range for the thermal reduction to happen is from 1673 to 1873 K [24]. Higher temperatures are often required for a total conversion. Therefore, its use is limited by the extremely high temperatures required. In fact, higher operating temperatures cause larger energy penalties due to heat losses and place constraints on the materials of construction of the reactor. Finally, they require very high solar concentration ratios [25]. The generic chemical reaction is 3.3 [26] and 3.4 [22] in case the reduction is complete and all the oxygen is released.

$$MeO_{oxidized} \rightarrow MeO_{reduced} + \frac{1}{2}O_2(g) \tag{3.3}$$

$$Me_xO_y \rightarrow xM + \frac{y}{2}O_2(g) \tag{3.4}$$

Reducing the oxide is necessary for the second part of the reaction, that is the re-oxidation of the metal and consequent reduction of another molecule. It is an exothermic reaction which can therefore happen at a lower temperature, around 800 - 1100 K. In the case of reaction with water, oxide (eq 3.5) [26] or metal (eq 3.6 [22]) is hydrolyzed to produce an oxide and hydrogen.

$$MeO_{reduced} + H_2O(g) \rightarrow MeO_{oxidized} + H_2(g) \tag{3.5}$$

$$xM + yH_2O(g) \rightarrow M_xO_y + yH_2(g) \tag{3.6}$$

An analogous reaction can be used to yield carbon or carbon monoxide [26] [22]. If operating at a very high temperature, it is possible to completely split CO_2 to atomic carbon C and oxygen O_2.

$$MeO_{reduced} + CO_2(g) \rightarrow MeO_{oxidized} + CO(g) \tag{3.7}$$

$$xM + yCO_2 \rightarrow M_xO_y + yCO \tag{3.8}$$

Alternately, a solar syngas can be produced by a combined reduction of water and carbon dioxide.

Metal oxides cycles can be classified as volatile or non-volatile.

- Volatile cycles, if the substrate needs to reach extremely high temperatures, thus it is volatilised, i.e., passes from solid-state to vapour. An example is ZnO, which is reduced at around 2000°C [21]. An advantage is that the reduction is stoichiometric, so the oxide loses all the oxygen. Unluckily, the high temperatures required extremely good thermal characteristics of the materials used in the system.
- Non-volatile cycles, if the material reduces at a lower temperature (between 1200 and 1500°C). They remain solid during the whole cycle and the reduction is usually not stoichiometric. However, there are some examples of non-volatile cycles that can operate a stoichiometric reduction [21]. Non-stoichiometric cycles keep the oxides stable from the crystallographic point of view. The lattice accommodates changes in anion or cation vacancies concentrations (e.g. $CeO_2(s) \rightarrow CeO_{2-\delta}(s)$) [27].

$$MeO_x \rightarrow MeO_{x-\delta}$$

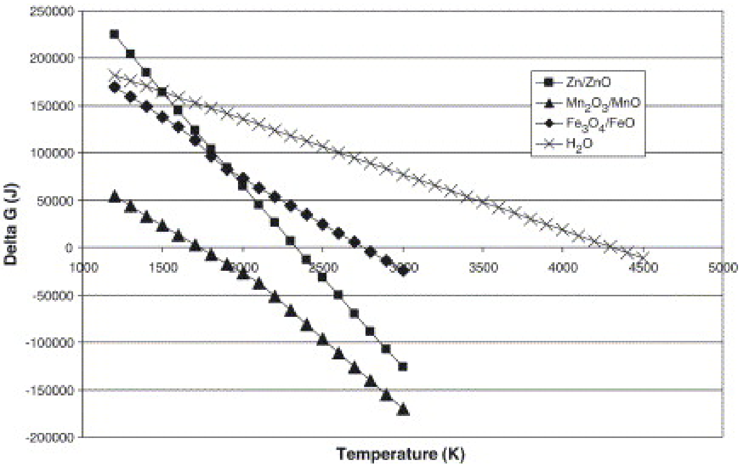

Figure 13 – Graph of Gibbs free energy of different chemical species involved in water splitting reactions [28].

3.1 Iron Oxides

Iron oxides are stoichiometric cycles and combine the advantages of both: they require lower temperatures for their reduction, but can have an almost stoichiometric reduction (passing from an oxidation state to the lower). Nevertheless, they present some drawbacks as well. The first time the reduction has been done in a solar facility was in Laboratoire PROcédés, Matériaux et Energie Solaire (PROMES) in Odeillo, France. It has been demonstrated that the temperature for the reduction was higher than the melting temperature of magnetite Fe_3O_4 (1808 K) and wüstite FeO (1643 K). Fig. 13, retrieved from the study of Perkins [28] shows the temperature for the Gibbs free energy to reach zero for the reaction of $Fe_3O_4 \rightarrow$ FeO is around 2700 K. Palumbo et al. [29] indicate that the temperature at which the reduction from magnetite to wüstite under carbon dioxide atmosphere starts happening spontaneously (i.e., Gibbs free energy reaches zero) is around 2250 K. Therefore, they are considering the reaction 3.9, where CO_2 is split into atomic carbon and oxygen.

$$6FeO + CO_2 \rightarrow 2Fe_3O_4 + C \tag{3.9}$$

Tofighi et al. [30] have shown that a 0.8 g sample reached 80% conversion after 5 min at 2000 °C under argon atmosphere. The same experiment but in air reached only 40% conversion. The liquid phase immediately reduced the surface of the material, thus causing deactivation of the reaction [26]. Moreover, melting of the oxide can also cause

Table 7 – Results obtained under different circumstance of hematite reduction (always inert atmosphere), showing it is even possible to perform reduction to wüstite at 1600°.

Reactant	Product	Reaction T (°C)	Total p (bar)	Chemical conversion (%)
Fe_2O_3	Fe_3O_4	1250	1	60
Fe_2O_3	FeO	2100	1	98
Fe_2O_3	FeO	1950	0.1	95
Fe_2O_3	FeO	1770	0.01	92
Fe_2O_3	FeO	1600	0.001	90

partial volatilization of the sample (thus decreasing the reducing power of water or carbon dioxide) and requires grinding and sieving of the material after every reduction. Therefore, many efforts have been done in order to decrease the temperature level for the reduction to happen.

In practice, it is possible to alleviate this problem by reducing the oxygen partial pressure in the reactor [27]. There are some quite old studies, by Bransky and Hed [31], Darken and Gurry [32], and Salmon [33] which ensure that, whether the oxygen partial pressure is kept under 10^{-11}, it is possible to obtain $Fe_{0.95}$ at 1573 K. If the partial pressure of oxygen is reduced to 10^{-15}, it is possible to make it at 1273 K. In fact, even if classified as stoichiometric, the wüstite phase is stable over a range of possible Fe/O ratios, from $Fe_{0.85}$ to $Fe_{0.95}$ roughly [27]. Therefore, extremely low oxygen partial pressures and accepting a non-stoichiometrical (full) reduction can be part of the solution for reducing the sample anyway at lower temperatures. Another interesting experiment has been realised by Charvin et al. [34] in 2007. They started from hematite and reduced it to wüstite, trying to obtain the purest oxide possible. Then, they performed cycling by reducing water to yield hydrogen and magnetite and repeated the reduction. The total reduction of hematite into wüstite was obtained at 1700 °C (and subsequent meting of the sample) and 0.1 bar under an inert atmosphere. Nevertheless, other interesting results are listed in table 7, showing it is possible to reach a high level of conversion (90%) of hematite into wüstite at 1600°C at very low total pressure.

3.1.1 Methane aided reaction

Keeping the goal of finding alternative ways of operating the thermal reduction of the iron oxides in a solar facility like the solar concentrator, interesting solutions are found. In fact, if the reduction is run in a different atmosphere than an inert (or worst, air), it is possible to change the chemical reaction happening and benefit of thermodynamic characteristics of other chemical species, without compromising the reduction of the sample. Examples found in literature suggest using gaseous hydrogen or methane as reducing agents. As hydrogen or syngas might be the final desired products of the reaction, this thesis and its literature review are mainly focused into further exploring the use of methane. This has been considered as an option for making the reaction more easily reproducible in the solar dish receiver also for the lower cost of methane compared to hydrogen.

When feeding the reactor with even a mixture of an inert gas and methane, the chemical reaction happening is no more only reduction of the oxide. Indeed, methane interacts with the oxygen in the iron lattice thus starting methane reforming and a more or less partial combustion. As they are happening in the loop, they are called Chemical Looping Reforming of Methane (CLRM) and Chemical Looping Combustion (CLC) respectively.

Chemical Looping Reforming is still in the early phase of its development. More in general, reforming is used to refer to all those processes in which a carbon-based fuel is exploited for yielding hydrogen or a syngas.

It is difficult to establish definitive conditions for these reactions to happen. The most general indication is given by Najera et al. [35], which explore the range of temperature between 600 and 1000°C. Therefore, several examples are reported, explaining how and why these reactions can occur at different temperature ranges and with different yields. Monazam et al. [36] claimed to be reaching 60% conversion of the oxide (ferrite) at 825°C after 45 minutes. Lu et al. [37] instead, operated at higher temperatures, around 1000°C and noticed a higher conversion level in a shorter time as the temperature increased. 80% is reached between 20 and 50 minutes, depending on the type of magnetite used and temperature (from 1223 to 1298 K). Looking at the yields of hydrogen per mass of iron oxide, they found 4.94 mmol/g for the original magnetite and 5.25 mmol/g for the calcinated magnetite.

3.1.2 Steam Reforming of methane

Today's majority of hydrogen production in fact, is outrun through steam reforming of methane (SRM) [38]. It is a highly endothermic reaction which therefore has to happen at high temperatures to obtain a favourable rate of conversion. In industrial facilities, reactors heated up with external firing are usually used. Here, methane reacts with steam at around 800°C thus producing a syngas of H_2:CO ratio of 3 according to reaction 3.10. The catalyst used is generally alumina, nickel or a noble metal. At this temperature, the enthalpy change is $\Delta h = +206 \left[\frac{kJ}{mol}\right]$ [21].

$$CH_4 + H_2O \rightarrow 3H_2 + CO \tag{3.10}$$

In reality, the reaction is not perfect, and the exiting mixture usually have the following molar composition: H_2 (43%), CH_4 (2%), CO (7%), CO_2 (6%), H_2O (42%) and traces [21]. To increase the hydrogen fraction in the mixture, the effluent is usually fed to another reactor for the Water-Gas Shift reaction 3.11. This reaction is exothermic and thus it is favoured at lower temperatures, between 200 and 350°C, and has an enthalpy change of $\Delta h = -44 \left[\frac{kJ}{mol}\right]$. The catalyst used is mainly nichel.

$$CO + H_2O \rightarrow H_2 + CO_2 \tag{3.11}$$

The products are generally in a mixture of components: H_2 (50%), CH_4 (1%), CO (0.3%), CO_2 (13%), H_2O (35%) [21].

Chemical-looping steam reforming is one of the oldest methods for producing hydrogen. It was developed at the beginning of last century by pioneers such as Messerschmitt and Lane for the production of hydrogen from gasified coal by using a porous 'sponge iron' [39]. During the following years, many advancements have been made, like the use of a fluidized bed to improve efficiency. Nevertheless, the process had several disadvantages: sintering of the carrier particles, low efficiency, and coking/carbon deposition.

In fact, steam reforming of methane replaced this method and emerged as the most economical process for large-scale hydrogen production. Hydrogen is positively looked at as a fuel, as its combustion only produces water. Anyway, when producing it from methane without appropriate carbon capture, the problem of the emissions is simply shifted. However, if an efficient capture is implemented in a centralized production plant, hydrogen becomes interesting again. Hence, the interest into Chemical-looping Steam Reforming. This technology does not require separation of H_2 from CO and has the potential for being a low cost process for hydrogen production without carbon emissions.

The process works with three reactors and iron oxides, operating between 550 and 900°C [40]. Hematite is reduced by methane to wüstite in the fuel reactor. FeO is then oxidized to Fe_3O_4 in the steam reactor (it is not thermodynamically possible to reach Fe_2O_3 only by using steam). Finally, Fe_3O_4 is re-oxidized to Fe_2O_3 by air in the air-reactor [38].

Fuel reactor [41]:

$$CH_4 + 4Fe_2O_3 \rightarrow CO_2 + 2H_2O + 8FeO \Delta H_{900C} = +356.5\frac{kJ}{mol} \tag{3.12}$$

Steam reactor [40]:

$$3FeO + H_2O \rightarrow Fe_3O_4 + H_2 \; \Delta H_{900C} = -43.2\frac{kJ}{mol} \tag{3.13}$$

Steam in excess has to be provided, but pure H_2 can be easily recovered just by cooling down the mixture and condensing the steam to liquid water.

Air reactor [40]:

$$2Fe_3O_4 + \frac{1}{2}O_2 \rightarrow 3Fe_2O_3 \; \Delta H_{900C} = -232.2\frac{kJ}{mol} \tag{3.14}$$

Reaction 3.14 is strongly exothermic, but is needed to burn out and clean the iron oxides from any carbon or sulphur containing residue is left from the hydrocarbon decomposition.

Net reaction:

$$3CH_4 + 2H_2O + 2O_2 \rightarrow 3CO_2 + 8H_2 \tag{3.15}$$

The process allows to output H_2 and CO_2 at two different stages of the reaction, thus making it much easier to sequestrate the CO_2 and have high purity hydrogen [38]. The process has been run in batch-fluidized bed reactor by Go et alii [42] which detected the formation of the oxides in the respective reactors. Unluckily, they also claimed the presence of CO_2 in the H_2 stream as a consequence of carbon deposits. Rydén et alii [40] operated the process in a two-compartment fluidized-bed reactor at 800–900 °C and atmospheric pressure. By removing the oxidation with air, they did not reach the highest state of oxidation, but only magnetite. However, being the reduction of Fe_3O_4 to FeO (3.12) endothermic, reaction 3.14 is necessary to obtain a continuous and thermally balanced process.

3.1.3 Dry Reforming

An alternate reforming process is Dry Reforming, if carbon dioxide is the oxidizing agent instead of water. CH_4 and CO_2 are processed at temperatures higher than 700°C over a catalyst (nickel or a noble metal) and produce syngas with an H_2:CO ratio of 1 as shown in reaction 3.25 [43].

$$CH_4 + CO_2 \rightarrow 2H_2 + 2CO\Delta H_{900C} = +261\frac{kJ}{mol} \tag{3.16}$$

However, both steam and dry reforming are hampered by many of the same issues: large energy demand (which can entirely defeat any intended reduction of CO_2 emissions), very high reactor operating temperatures, high catalyst cost, catalyst deactivation due to coking, and poor product selectivity for syngas. Dry Reforming can also be operated in a chemical-looping layout. This is an interesting way of re-using CO_2 to produce CO, a highly versatile and widely used chemical. Iron oxides are once again attractive candidates for the reaction because of their low toxicity, low cost and thermodynamically favourable equilibrium for the reaction with CO_2 [38]. Nanostructured core-shell Fe@SiO2 and nanocomposite Fe-BHA (Barium Hexa-aluminate) show that efficient CO2 activation is indeed possible via a CLDR process [35]. The cycle works similarly to the previously mentioned Steam reforming. Oxidation to hematite can be performed in air to quantitatively remove undesired impurities and silicates, strongly improving the carrier utilization although the process becomes more expensive and complex [38].

3.1.4 Chemical-looping Combustion

A promising technology for fossil fuel combustion that enables efficient carbon dioxide sequestration in a concentrated stream is Chemical-looping Combustion (CLC) for power production. The combustion of a fuel is broken down into two, spatially separated half-steps [38]. It provides periodic oxidation and reduction of an oxygen carrier for the flameless, NO_x-free combustion [35]. An oxygen carrier such as Fe_2O_3, NiO or CuO is reduced by transferring the oxygen to the fuel. Subsequently, it is oxidized via reaction with air [38]. Its surface area is increased through the combination with another inert material such as Al_2O_3, TiO_2, SiO_2, $MgAl_2O_4$, $NiAl_2O_4$ or a bentonite. Different kinds of renewable or fossil fuels can be used in the CLC, like coal, biomass, but when methane is used as a reducing agent, CO_2 emissions are less compared to other fuels and also contamination is almost negligible [36]. It usually works with two different reactors. Reaction 3.17 is referred to what happens in the fuel reactor.

$$CH_4 + 12Fe_2O_3 \rightarrow 8Fe_3O_4 + CO_2 + 2H_2O\Delta H_{900C} = 184.0\frac{kJ}{mol} \tag{3.17}$$

Respectively, in the air reactor 3.18

$$2O_2 + 8Fe_3O_4 \rightarrow 12Fe_2O_3\Delta H_{900C} = -986.5\frac{kJ}{mol} \tag{3.18}$$

As reaction 3.17 and 3.18 are conducted in a cycle, the overall reaction is:

$$CH_4 + 2O_2 \rightarrow CO_2 + 2H_2O\Delta H_{900C} = -802.5\frac{kJ}{mol} \tag{3.19}$$

From reaction 3.19 it can be seen that the amount of energy released is the same as in conventional combustion. The main difference lies in the fact that CLC allows to have two separate streams. Moreover, the flue gas from the "combustor" contains almost only CO_2 and H_2O, thus only a condenser is needed for sequestration.

3.1.5 Chemical-looping Partial Oxidation

Unlike chemical-looping reforming processes discussed above, Chemical-looping Partial Oxidation (CLPO) does not require changes to the reactor feeds. Indeed, CLPO works as a modification of the internal circulation rates and oxygen carrier materials used in CLC. The goal is to achieve incomplete (i.e., partial) oxidation, so that not all the oxygen is transferred to the fuel, but only a fraction [38]. Chemical-looping partial oxidation is significantly more challenging because not only partial oxidation of the fuel (in this case, methane) 3.20, but multiple side reactions as well occur in practice. These include complete oxidation 3.17; steam reforming 3.10, water gas shift 3.11, carbon deposition (pyrolysis/cracking) 3.21, and carbon gasification 3.22 [38].

$$Fe_3O_4 + CH_4 \rightarrow 3FeO + CO + 2H_2 \Delta H_{298K} = 280.9\frac{kJ}{mol} \tag{3.20}$$

$$CH_4 \rightarrow C + 2H_2 \tag{3.21}$$

$$C + H_2O \rightarrow CO + H_2O \tag{3.22}$$

$$C + CO_2 \rightarrow 2CO \tag{3.23}$$

$$CH_4 + H_2O \rightarrow CO + 3H_2 \tag{3.24}$$

$$CH_4 + CO_2 \rightarrow 2CO + 2H_2 \tag{3.25}$$

$$CO + H_2O \rightarrow CO_2 + H_2 \tag{3.26}$$

While some of these reaction contribute to the yield of CO and H_2, as expected from the partial oxidation, others instead produce CO_2 3.26 or atomic carbon, which remains on the substrate 3.21.

Monazam et alii [36] performed an experiment for studying the kinetics of reduction of hematite by methane during CLC. The theoretical reduction chain they considered was:

$$Fe_2O_3 \rightarrow Fe_3O_4 \rightarrow FeO \rightarrow Fe$$

They investigated the reaction of iron oxides with a mixture of inert gas and different percentages of methane (15-35%) between 700 and 825°C. The experiment has been run in a thermogravimetric analyzer with the layout shown in figure 14. The sample of iron

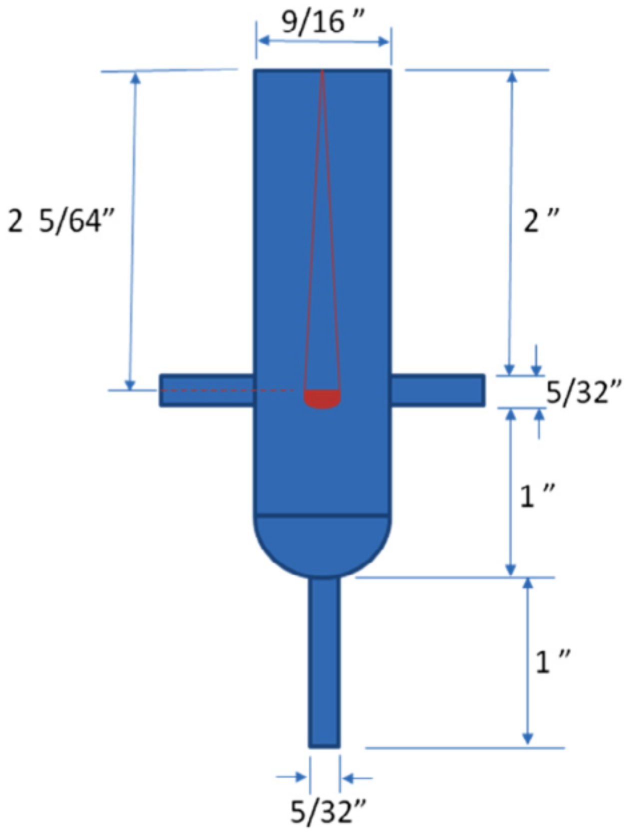

Figure 14 – Sketch of the thermogravimetric analyzer used by Monazam et alii [36].

oxide is placed on the crucible hold in the center of the reactor. Weight changes were measured during the tests, as in a typical thermo gravimetric experiment. Figure 15 shows the cyclic variations of the sample mass due to oxygen loss and gain and carbon deposition on the carrier. Gas mixture used in the reaction enters and exits from the lateral ports, while the one at the bottom is closed. They performed tests with a sample of 60 mg and a total gas flowrate of 45 cm^3/s. Cycles were carried out at constant temperature (i.e., they did not change the temperature level between the oxidation and the reduction). Therefore, the only difference between oxidation and reduction was in the gas swept in the reactor. Reduction reaction times were set at 45 min, while oxidation reaction times were 30 min for all experiments. In between each phase of the cycles the system was flushed with ultra-high pure nitrogen for 10 min. At the exit of the gas stream, a mass spectrometer records the concentrations of CH_4, CO_2, H_2O, H_2, CO, and O_2.

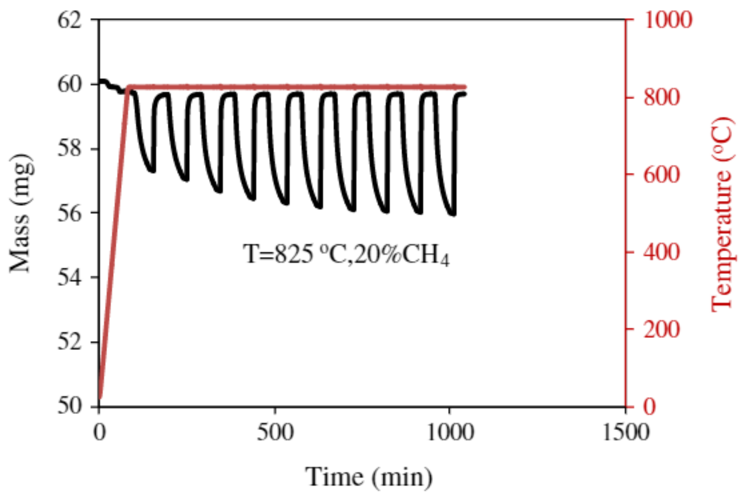

Figure 15 – Typical mass and temperature measurement for hematite using 20% CH_4 for reduction and air for oxidation reactions [36].

The conversion degree can be defined as:

$$X = \frac{m_0 - m(t)}{m_0 - m_f} \tag{3.27}$$

where m_0 is the initial mass of the sample, m_f is the mass of the sample when the reduction is complete and $m(t)$ is the instantaneous weight. In this study, m_f is considered as the mass of FeO and 100% conversion means that the hematite was all converted to FeO. Figure 16 shows the effect of temperature on the reduction of hematite. Considering that, as previously mentioned, time for the reduction reaction was set at 45 minutes, a higher temperature allows to reach a higher level of reduction in the given time. While a slight improvement is seen when going from 700°C to 800°C, the situation is considerably better at 825°C.

Another important issue they noticed is related to carbon deposition. When increasing the temperature and the CH_4 concentration, the phenomenon becomes more relevant. Nevertheless, if the results are normalized to the methane fed, the relative amount of deposited carbon for higher concentrations of CH_4 in the fed is lower, as it can be seen in Fig. 17.

By studying the kinetics of the reaction, the group reached the conclusion that a higher temperature causes a higher derivative of the conversion degree during the initial minutes of the reduction. Looking at the gases produced by the reduction reaction instead,

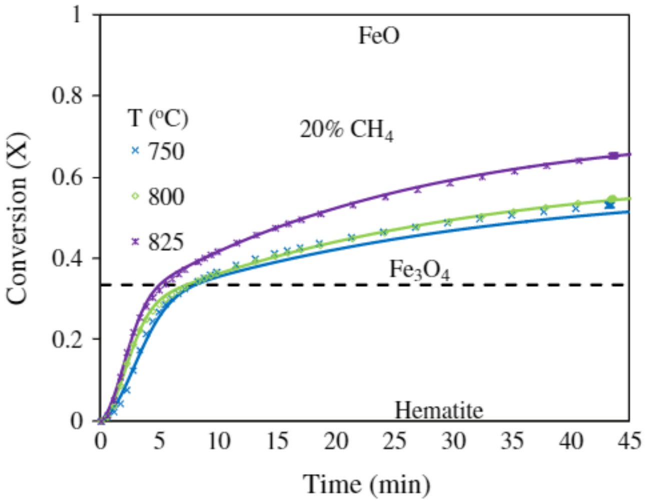

Figure 16 – Conversion rate of hematite (Fe_2O_3) to FeO at different temperatures using 20% CH_4 [36].

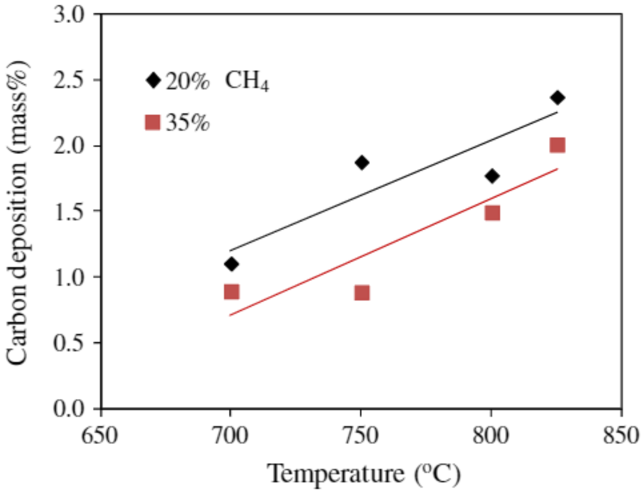

Figure 17 – Carbon contents in reduced hematite for different temperature and CH_4 concentrations (20% and 35%) [36].

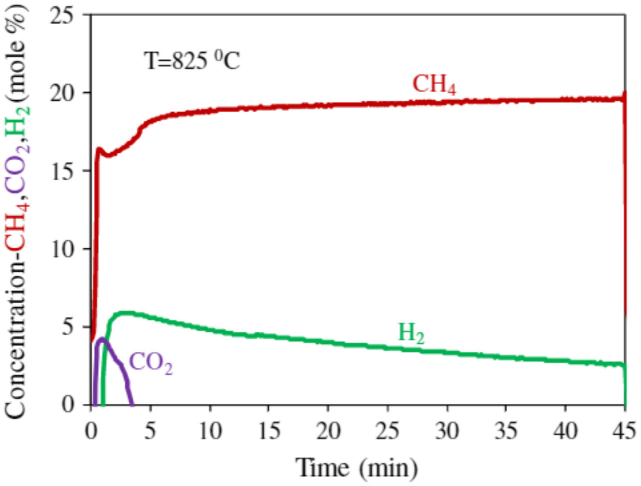

Figure 18 – Outlet gas analysis for the reduction of hematite (Fe_2O_3) with methane (20% CH_4) using a reaction temperature of 825°C [36].

Fig. 18 shows that the CH_4 concentration at the outlet increases rapidly to reach a temporary maximum. At the same time, CO_2 starts to rise. Subsequently, CH_4 concentration keeps increasing. H_2 reaches a maximum value together with CH_4 and then decreases. Fig. 18 illustrates how CO_2 and H_2O concentrations behave: the maximum value is reached initially when CH_4 concentration was still increasing. This means that at the early stages of the reduction, most of the CH_4 was totally oxidized into CO_2 and H_2O. While, as the reaction proceeded, remaining unconverted CH_4 was detected. Simultaneously, CO and H_2 were released into minor amounts due to the partial oxidation of some CH_4 to CO and H_2 instead of CO_2 and H_2O, see Fig. 19.

One of the goals of kinetic studies is to deduce the reaction mechanism. At low conversion stages, the reduction from hematite to magnetite probably happens through the exothermic stage, thus requiring high activation energy. This is due to the sum of the enthalpies of reversible processes and activation energy of irreversible processes happening. When the conversion has already started and proceeded, the activation energy decreases, a phenomenon characteristic of a reversible endothermic process [44]. The probable reaction mechanism is divided into reduction of hematite to magnetite and reduction of magnetite to wüstite:

Methane decomposition and reduction of hematite to magnetite

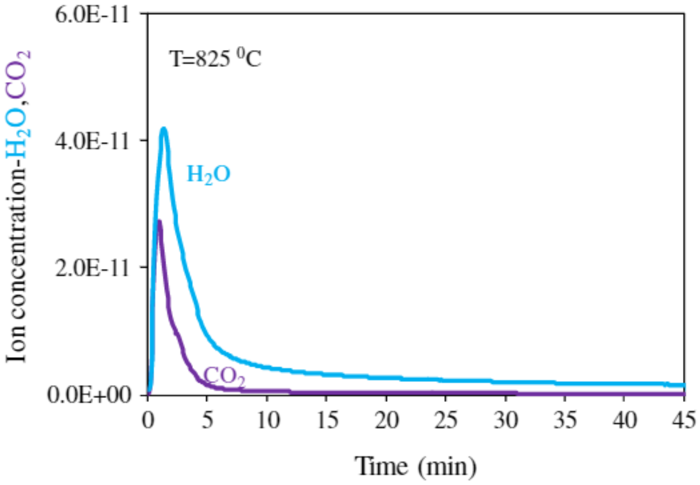

Figure 19 – Ionic concentration of H_2O and CO_2 for the reduction of hematite (Fe_2O_3) with methane (20% CH_4) using a reaction temperature of 825°C [36].

$$3CH_4 \rightarrow 3C + 6H_2 \Delta H^0_{r,800C} = 263.34 \frac{kJ}{mol} \tag{3.28}$$

$$CH_4 + 12Fe_2O_3 \rightarrow 8Fe_3O_4 + CO_2 + 2H_2O \Delta H^0_{r,800C} = 161.1 \frac{kJ}{mol} \tag{3.29}$$

$$3C + 12Fe_2O_3 \rightarrow 8Fe_3O_4 + CO_2 + 2CO \Delta H^0_{r,800C} = 346.2 \frac{kJ}{mol} \tag{3.30}$$

$$H_2 + 3Fe_2O_3 \rightarrow 2Fe_3O_4 + H_2O \Delta H^0_{r,800C} = -6.75 \frac{kJ}{mol} \tag{3.31}$$

$$4CH_4 + 27Fe_2O_3 \rightarrow 18Fe_3O_4 + 2CO_2 + 2CO + 3H_2O + 5H_2 \Delta H^0_{r,800C} = 771.86 \frac{kJ}{mol} \tag{3.32}$$

Methane decomposition and reduction of magnetite to wüstite

$$2CH_4 \rightarrow 2C + 4H_2 \Delta H^0_{r,800C} = 178.9 \frac{kJ}{mol} \tag{3.33}$$

$$CH_4 + 4Fe_3O_4 \rightarrow 3FeO + 2H_2O + CO_2 \Delta H^0_{r,800C} = 377.9 \frac{kJ}{mol} \tag{3.34}$$

$$2C + 3Fe_3O_4 \rightarrow 9FeO + CO_2 + CO \Delta H^0_{r,800C} = 377.5 \frac{kJ}{mol} \tag{3.35}$$

$$H_2 + Fe_3O_4 \rightarrow 3FeO + H_2O \Delta H^0_{r,800C} = 46 \frac{kJ}{mol} \tag{3.36}$$

$$3CH_4 + 8Fe_3O_4 \rightarrow 24FeO + 2CO_2 + CO + 3H_2O + 3H_2 \Delta H^0_{r,800C} = 981 \frac{kJ}{mol} \tag{3.37}$$

The overall reaction of reduction of hematite to wüstite is found to be:

$$7CH_4 + 27Fe_2O_3 \rightarrow 10Fe_3O_4 + 24FeO + 4CO_2 + 3CO + 6H_2O + 8H_2 \Delta H^0_{r,800C} = 1752.9 \frac{kJ}{mol} \tag{3.38}$$

Since the mass spectrometer initially detected the presence of CO and H_2, it has been supposed that the reactive gas (CH_4) initiates hematite reduction. Therefore, it is thought hematite reduction is initially controlled by the topochemical process. Once a thin layer of lower iron oxides such as wüsite is formed on the surface, the mechanism shifts to two simultaneous reaction mechanism (Fe_2O_3 to FeO and produce CO and H_2, intrinsic topochemical kinetics and Fe_2O_3 to Fe_3O_4 and produce CO_2 and H_2O, nucleation and growth kinetics).

The study is relevant to this thesis as it explores the reduction of iron oxides in the temperature range the solar concentrator might more probably be reaching. Indeed, it shows that through the help of methane, the reaction is feasible even at temperatures lower than 850°C. As a main outcome for the intended goal, it is found the CLC is not complete, but rather a mix of CLC and CLPO, thus yielding both carbon dioxide, but also still useful solar syngas.

Another interesting paper that illustrates useful findings for the thesis is the work of Najera et al. [35]. Although they focused mainly on the oxidation of the carriers, they also made some considerations on the reduction reaction with CH_4 as a fuel, as it is important for maximizing the subsequent oxidation and CO_2 sequestration. They performed thermodynamic calculations with the commercial software FACTSTAGE 5.0 to determine the thermodynamic equilibrium limitations for cyclic carrier oxidation and reduction in CLDR. The software seeks Gibbs free energy minimization of the reactant and product mixture at fixed temperature and pressure. They analyzed various possible oxygen carriers, including iron oxides. The graph in figure 20 shows the result of calculations for reduction of Fe_3O_4 with stoichiometric methane supply over a range of temperatures from 600 to 1400°C. It looks clear how the increase of temperature is beneficial to the reduction reaction. Values above 60% are reached for temperatures higher than 700°C for both Fe_3O_4 conversion and FeO selectivity. In this case, FeO is the only reduction product for the carrier. When supplying a quantity of methane sufficient for stoichiometric reduction of Fe_3O_4, a mixture of Fe and FeO is found as reaction product and carrier conversion is complete at every temperature. Anyway, when using stoichiometrical CH_4 supply, the incomplete conversions and selectivities, suggest that

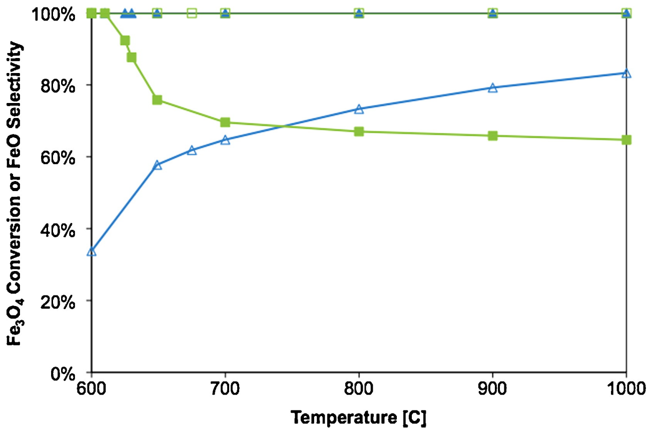

Figure 20 – Thermodynamic calculations for carrier reduction with stoichiometric supply of methane for reduction of Fe_3O_4 to FeO (open symbols) or Fe (filled symbols), respectively. Shown are Fe_3O_4 conversion (triangles) and selectivity to FeO (squares) [35].

methane oxidation over iron oxides rather is a mix of total and partial oxidation, in accordance to the results of Monazam [36]. Fig. 21 shows instead reaction from the gas phases point of view. Although methane conversion is extremely high, always above 96% when the temperature is higher than 600°C or even close to 100%, it does not mean the products are originated from a total oxidation. It seems total oxidation of methane happens more at lower temperature, while, as the temperature increases, H_2 and CO selectivities decrease (i.e. partial oxidation is more present). This is found to happen regardless of stoichiometry for full or partial oxidation of methane. A slight increase in selectivity for partial oxidation products has been noticed when the methane feed is increased. Moreover, carbon formation is also predicted in the reduction reactor for temperatures below 650 °C for Fe_3O_4 reduction with a stoichiometric methane supply.

Lu et al. [37] studied the use of iron oxides for chemical-looping production of hydrogen. In particular, they considered the reactions between magnetite and wüstite. In their experimental tests, they performed 6 cycles of CH_4 reduction and H_2O oxidation to obtain the stable state of the oxygen carrier before kinetic analysis. Reduction was done at 950°C for 60 minutes with a gas flow of 250 mL/min composed of 10% CH_4 and 90% N_2. Before switching to oxidation, the reactor is cleaned for 20 minutes with pure N_2. Oxidation instead, is performed with a stream of water vapor diluted by N_2 for 55 minutes at 850°C.

Then, they did a thermogravimetric analysis (HTG-3, Beijing Scientific Instrument

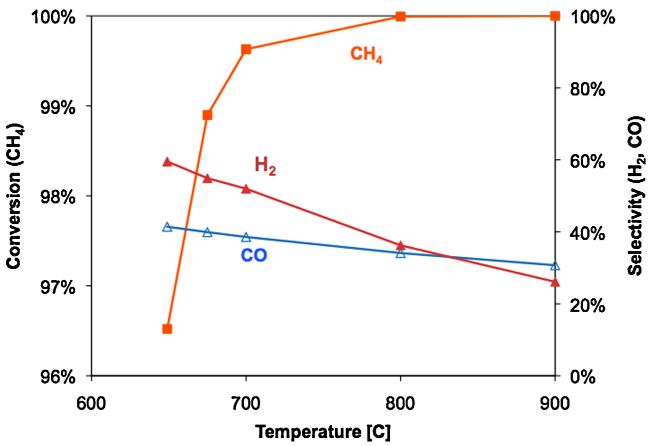

Figure 21 – Methane conversion (squares) with stoichiometric methane feed for full oxidation with oxidized carrier Fe_3O_4, showing temperature dependent selectivity of partial oxidation over full oxidation (H2 over H2O (open triangles) and CO over CO2 (filled triangles)) [35].

Factory) with samples of 300 mg weight and particle size of 380–830 μm. The experiment run under selected isothermal conditions (i.e., 1223, 1248, 1273 and 1298 K). The samples were placed in a high purity alumina crucible and heated in a furnace from ambient temperature to the predetermined temperatures at a heating rate of 10 °C/min under an inert gas flow of pure N_2. Thereafter, a reducing gas flow of 150 mL/min of (90% N_2 and 10% CH_4) was introduced into the furnace after the desired temperature was reached. The kinetics of the reduction from magnetite to wüstite has been deduced by the mass change of the samples. Indeed, when going from Fe_3O_4 loose 6.90% of their weight, as it can be noticed from reaction 3.39.

$$Fe_3O_4 + CH_4(g) \rightarrow 3FeO + CO(g) + 2H_2 \tag{3.39}$$

Fig. 22, retrieved from the paper, plots the production of CO and H_2 during the reduction of the sample under methane atmosphere. After an initial period of around 10 minutes, during which the concentrations of these gases are very low, they increase quickly. This might suggests that the induction period is quite long for the reaction, probably because of the dense structure of the magnetite. The presence of H_2 is almost twice the CO, while very little amounts of CO_2 are detected, probably meaning the oxidation of CH_4 is is mainly partial. This seems to be in accordance with what Najera et al. [35] said about the effect of temperature on partial/complete oxidation. In the end of the reaction, additional increase of the H_2 concentration indicates methane decomposition. They also

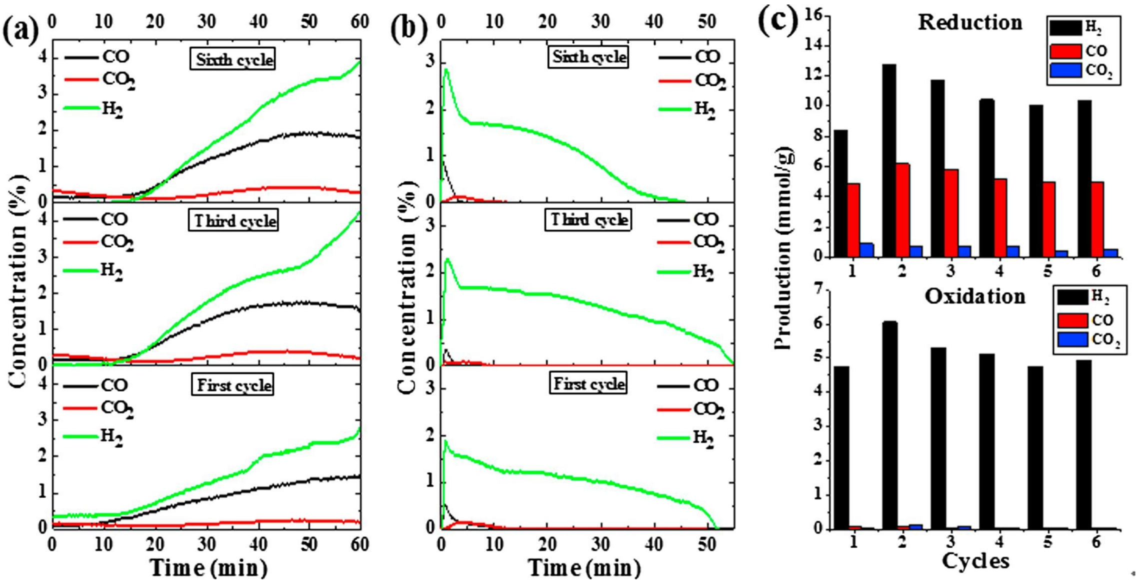

Figure 22 – Typical curves of H_2/CO/CO_2 concentration during reduction (a) and oxidation (b) process and yields of CO, H_2, and CO_2 in the oxidation or reduction step (c) with original magnetite as oxygen carrier [37].

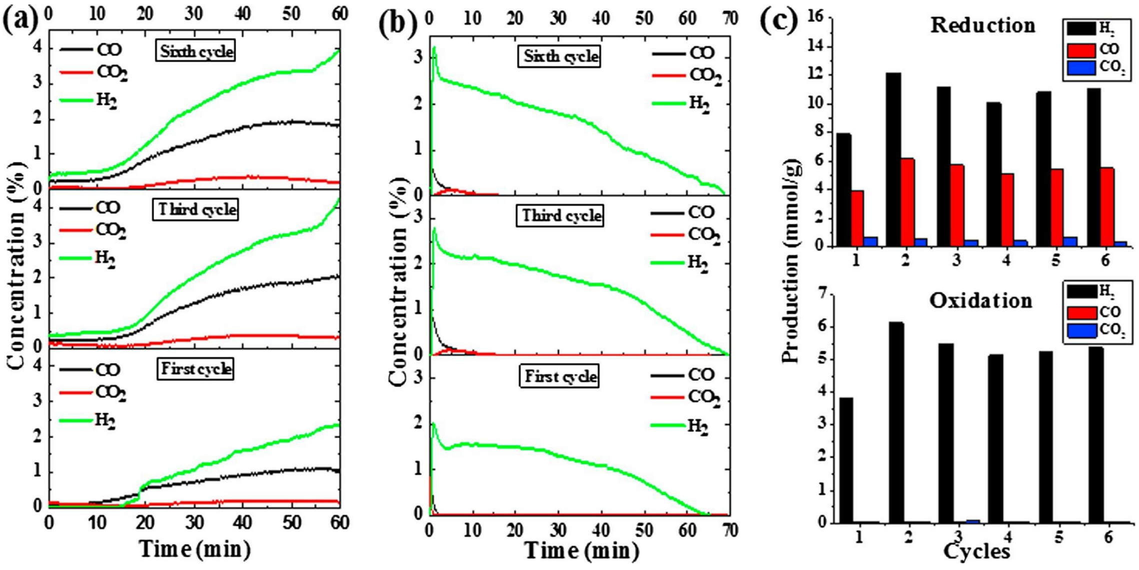

Figure 23 – Typical curves of H_2/CO/CO_2 concentration during reduction (a) and oxidation (b) process and yields of CO, H_2, and CO_2 in the oxidation or reduction step (c) with calcined magnetite as oxygen carrier [37].

studied the behaviour of calcinated magnetite (2h under ambient air at 1000°C), in fig. 23, which was found to be similar and sometimes even better than original magnetite. In fact, less CO_2 is produced in the reduction step (i.e. more partial oxidation than total) and the amount of carbon oxides (CO and CO_2) in the water oxidation step is reduced. Therefore, it means a higher selectivity of syngas and hydrogen.

3.2 Ferrites and Doping

Among the possible solutions, there is the chance of adding an additional element to the iron oxides, thus creating a ferrite. Indeed, the partial substitution of iron cations in the magnetite's matrix by a transition (e.g. Mn, Co, Ni or Zn), or an alkaline earth (e.g. Mg) metal, originates mixed metal iron oxides called ferrites, of the form $(Fe_{1-x}M_x)_3O_4$. Using these alleviates some of the main issues as reduction can happen at lower temperatures than pure magnetite. Moreover, their reduced mixed wüstite phase $(Fe_{1-x}M_x)O$ is still capable of splitting water [45].
Ferrites belong to the family of spinel materials, a group similar to perovskites as they are both oxides containing multiple metal cations in various valence states. Spinels are of the general formula $A^{+2}B^{+3}O_4$ [26]. In the case of ferrites, B would be iron, while A would be one or more than one other metallic cation. In fact, both A and B sites can be occupied by even more than one positive ion, e.g. $(A_x,B_{1-x})^2(C_y,D_{2-y})^{+3}O_4$. Likewise, perovskites usually have formulae $A^{+2}B^{+4}O_3$, or more generally $(A_x,B_{1-x})^{+2}(C_y,D_{2-y})^{+4}O_3$.

An example of how useful adding another element to the oxide can be for the performances of the reduction has been explained by the study of Guo et al. [46]. They analyzed the case of cobalt and found out that only 2% doping in iron oxides can dramatically increase the reactivity in chemical-looping reforming system at low temperature. The presence of cobalt induces oxygen vacancy which helps overcome the energy barrier of methane reforming. The experiment was run similarly to other studies already mentioned, as it consisted of a thermogravimetric analysis for understanding the behaviour of the carrier. The sample was prepared with the sol gel method for dispersing the desired concentration of cobalt into the iron oxide. The 15 mg sample was placed on an alumina crucible and reduced and oxidized for 5 cycles of pre-treatment at 800 °C. Later, they run 10 continuous reduction-oxidation cycles at 600, 700, and 800 °C using a Setaram SETSYS Evolution Thermogravimetric Analyzer. The gas used for the tests was a mixture of inert gases (50 mL/min N2 and 100 mL/min Helium). For the reduction process, a 25% CH4 (50 mL/min) was added to the inert gases for 5 minutes, while the oxidation process used 25% air (50 mL/min) balanced with inert gas for other

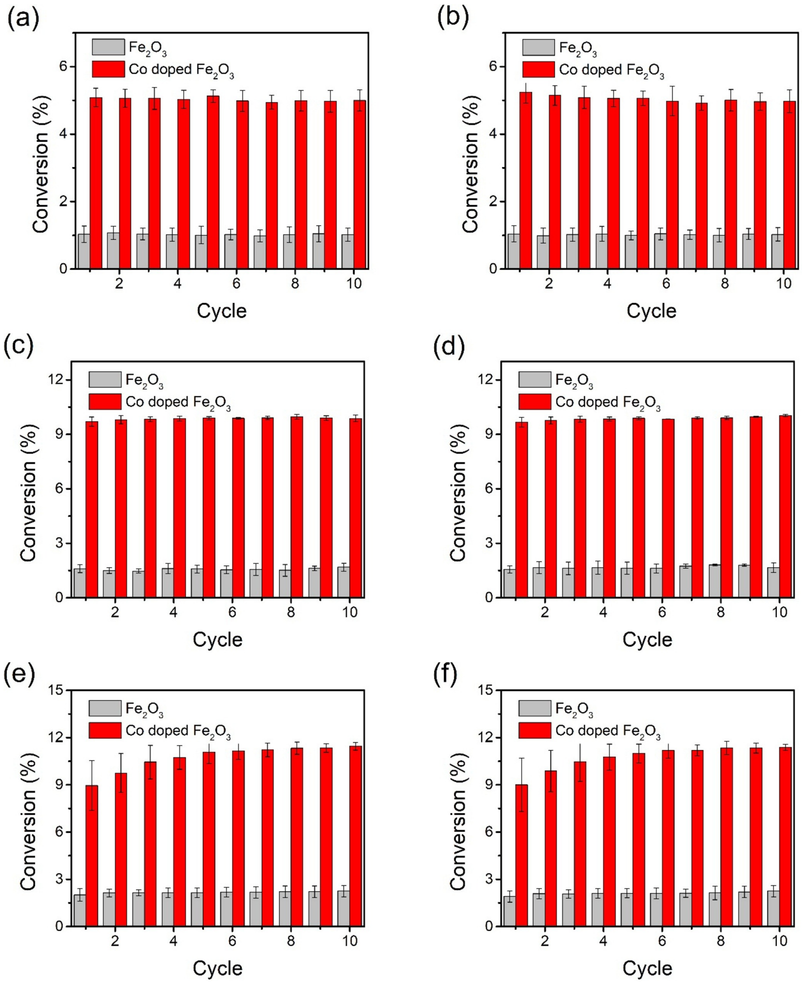

Figure 24 – Comparison between conversion of pure hematite and 2% Co-doped Fe_2O_3 in reduction and oxidation at 600°C, 700°C and 800°C [46].

5 minutes. In between the phases, the system was flushed for 10 minutes with an inert gas for cleaning and avoiding any contact between gaseous O_2 and CH_4.

The research team considered to use different concentration of cobalt for the creation of the ferrite, but by characterizing them with SEM it was found out that doped ferrite and pure hematite have similar average grain sizes, which are around 3.84.6μm. This suggests that the Co doped materials have little morphological change, which is advantageous for chemical looping applications.

Finally, when comparing the performances of pure Fe_2O_3 and 2% Co-doped ferrite, it looks clear how improved the performance of the latter is. Results are shown in fig. 24. Fig. 25 instead, compares the performances of the reactions at different concentration of dopant. It looks clear that increasing the concentration of Co over 2% is not that beneficial to the performances at any temperature level.

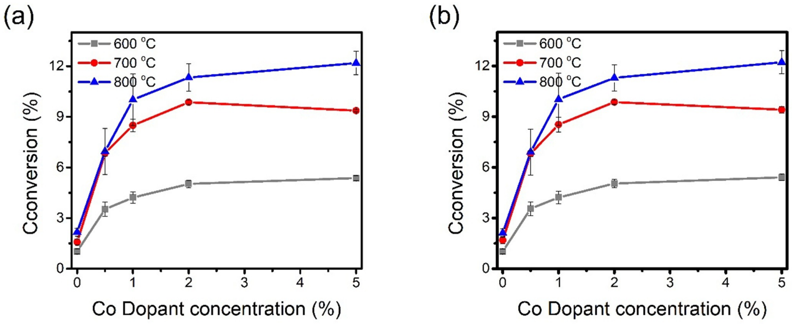

Figure 25 – TGA average redox conversion results of different Co dopants concentrations at different temperatures for (a) oxygen carrier reduction and (b) oxygen carrier oxidation [46].

Another group, composed by Qin et al. [47] studied instead the case of doping the hematite matrix with Lanthanum. The concentration they used was 1%, as they wanted to demonstrate that it is possible to obtain high performances from the ferrite even by using low dopant concentration. They studied the behaviour of the material through a thermogravimetric analysis by cyclic redox reactions using CO and CH_4. The samples were prepared by mechanosynthesis of Fe_2O_3 and La_2O_3 powders and subsequent compression into pellets of 30 mg. They were mounted on an alumina crucible for TGA using a Setaram SETSYS Evolution Thermogravimetric Analyzer. A mixture of 200 mL/min flow consisting of 50% air balanced with N_2 was used for the oxidation was performed, while the reduction step used a 200 mL/min flow of gas containing 50% CO at 700°C or CH_4 balanced with N2 at 1000°C. As in the other studies, oxidation and reduction were separated by a 5 minutes flushing step using a pure nitrogen flow of 100 mL/min. As Guo et al. [46] did, Qin [47] and his group as well compared the performances of pure hematite with the doped one under the same testing conditions. Experimental activity showed how the doping positively influenced the reactivity of oxygen carrier reduction in each cycle. Moreover, the conversion rate increased by 125% in the first cycle and 245% in the fifth cycle. The presence of lanthanum also benefit the oxidation phase, by averagely increasing the conversion rate of a 250%. Figure 26 clearly pictures these findings. Focusing in particular on the reaction with methane, as it is more relevant to this thesis aims, it was found out that La-doped Fe_2O_3 exhibits enhanced reactivity. Additionally, when reacting with CH_4, at 1000 °C, the reactivity of the La-doped oxygen carrier grows between 81 and 243% in each cycle. The main

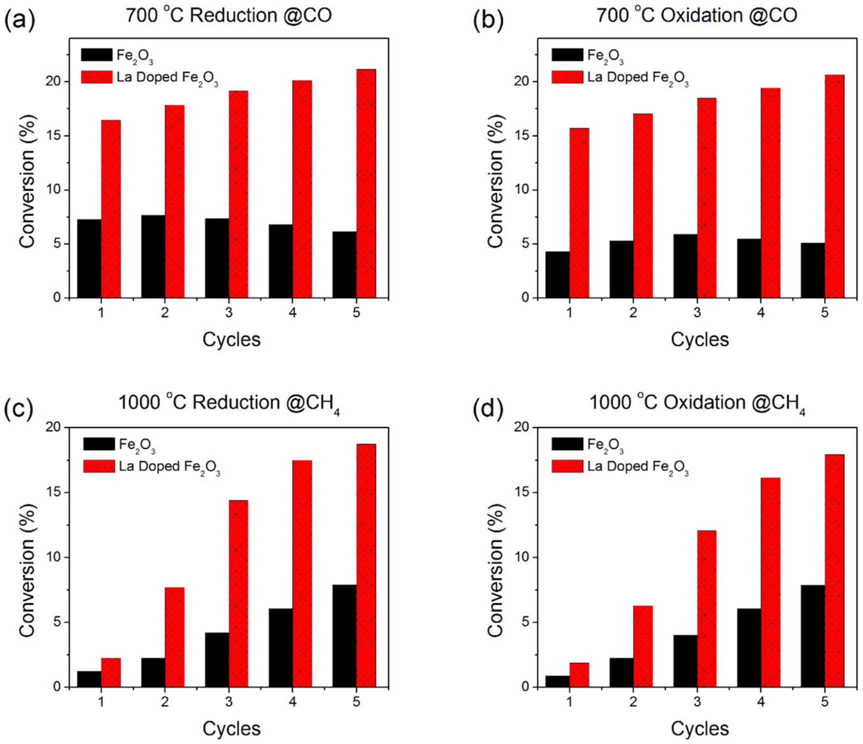

Figure 26 – Comparison between conversion rates in reduction and oxidation reactions of simple Fe_2O_3 and La doped Fe_2O_3 under CO or CH_4 mixtures as reducing gases [47].

learning is that the La dopants have high catalytic activity in combustion and oxidation of lower valence iron cations. The help given by the La dopant consists in the ability to lower the barriers of the C–O bond and C–H bond activation during metal oxide redox reactions. Hence, doping iron oxides with similar materials revealed dramatic metal oxide property modification just by using a relatively simple fabrication process.

There are other studies exploring the effectiveness of adding an additional element into the Co-doped ferrite matrix, as the one of Ma et al. [48]. They focused on several ternary spinel-structured ferrites and explored the effect of the amount of manganese on the materials activity at 650 °C. Once again, samples were prepared with sol gel method, so that not only cobalt, but manganese as well was added to the hematite. Prepared samples for the TGA weighted 0.5 g. The reducing agent was a mixture composed of a 20 vol % H_2 with 80% N_2 gas mixture with a flow rate of 800 mL/min, 99.99% purity. The oxidizing gas was a 20 vol% CO_2 with 80% N_2 gas mixture with a flow rate of 800 mL/min, 99.99% purity. Materials and reactions were studied over 10 successive cycles between 550 and 850 °C. Results showed how the performances in the reduction phases were decreasing with temperature, but also varied depending on the manganese concentration. In these conditions, time for reaching 60% of total conversion, was between 540 and 480 s, compared to the experiment of Monazam et al. [36] which instead required even 45 minutes for reaching the same degree of conversion of pure iron oxides. Although the conditions of Monazam's experiment were different, as the reducing agent used was CH_4 and not H_2, the comparison shows anyway the improvements obtained by doping (and co-doping) the oxides.

Figure 27 illustrates how the reduction reaction for Co, Mn co-doped samples was higher than that of Co, Fe binary materials. Moreover, the highest conversion was reached by $Mn_{0.2}Co_{0.8}Fe_2O_4$ for all the temperatures. Therefore, they concluded that manganese has a promotion effect on the reduction of the samples and the performance of the samples was influenced by the doping amount of the Mn. The reason for the best performances of $Mn_{0.2}Co_{0.8}Fe_2O_4$ is explained in figure 27(e), as the activation energy of this ferrite is lower at every temperature, thus enhancing its performances at lower temperature.

3.3 Perovskites

Perovskites are also an interesting oxygen carriers for chemical-looping processes. They are non-stoichiometric compounds with a good reversibility in delivering and picking up oxygen at high temperatures. They are usually used in fuel cells because of this. Perovskite is the term related to a group of minerals with the crystalline structure of calcium titanium oxide, $CaTiO_3$. In the general formula ABX_3, the A and B positions are occupied by cations, which can have a very different size, while X spots are occupied by anions which bonds with the cations. The structure resembles a cube as the vertexes are occupied by the B cations, A cations are in the center of the cube and X anions lay on the edges of the cube. In other words, it consists of almost hexagonal close packed oxygen layers with cations defining octahedral layers perpendicular to the c-axis [49]. Despite their already known good performances, interest in this oxygen carrier only raised in 2013. The group of Scheffe et al. from ETH/PSI [27] studied thermodynamically and

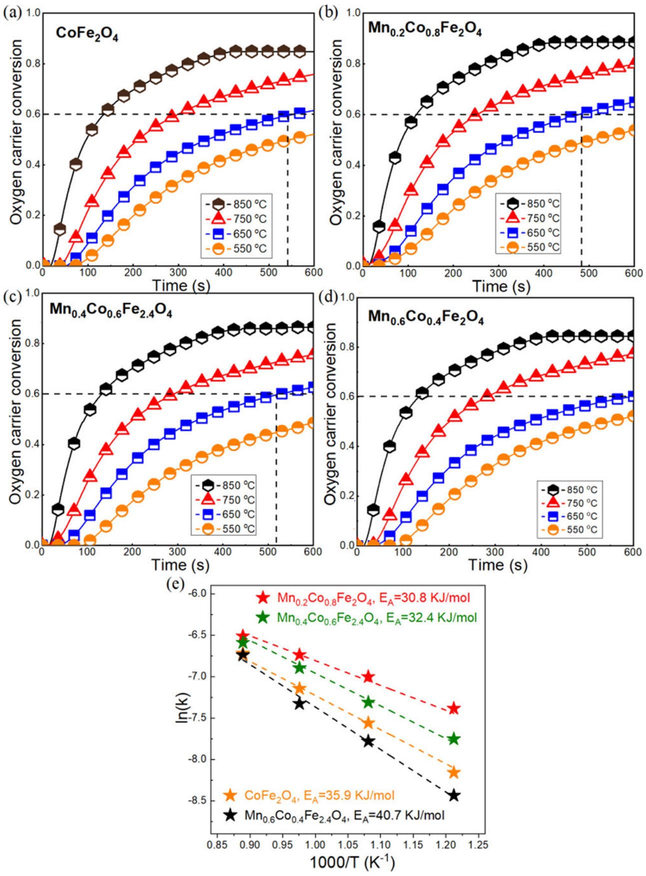

Figure 27 – Oxygen carrier conversion for (a) $CoFe_2O_4$, (b) $Mn_{0.2}Co_{0.8}Fe_2O_4$, (c) $Mn_{0.4}Co_{0.6}Fe_2O_4$, (d) $Mn_{0.6}Co_{0.4}Fe_2O_4$ at various temperatures and (e) Arrhenius plots for the samples reduced in H_2 at 650 °C.

experimetally Lanthanum–Strontium–Manganates (LSM)/$La_{1x}Sr_xMnO_{3ffi}$ for both WS and CDS. While reduction at 1000°C yielded higher O_2 amounts when compared to cerium oxides, oxidation with CO_2 was not complete. Jiang et al. [50] instead, used perovskites for producing O_2 and CO at 1300°C. They tested perovskites of the type $La_{1-x}A_xB_yFe_{1-y}O_{3-\delta}$ (A=Sr, Ce, B=Co, Mn) and found out that the support used (ZrO_2, Al_2O_3 and SiO_2) was responsible of great differences in the reaction performance for carbon dioxide splitting.

4

EXPERIMENTAL TEST

Before running the experimental tests with the solar concentrator on the Energy Center rooftop, it has been necessary to prepare the receivers and finalize the set-up of the test bench.

Reactors were prepared in the lab facilities of the Environment Park in Torino. As the iron oxides packed bed has to stay at the middle of the alumina pipe, there is the necessity of a supporting material that can hold the powder in place, without time compromising the gas flow inside the pipe. The appropriate material has been identified in glass wool. Indeed, due to its high porosity, thermal insulation and high temperatures resistance, glass wool seemed to be suitable for the application. Glass wool has been inserted in the pipe from an edge and pushed inside with a metallic rod for creating a consistent obstacle to powder escape. Once reached the desired point by pushing with the rod, the glass wool stays in place and can block the passage of powders. Commercial hematite has been weighed with a precision balance so that the chosen amount could be inserted in the pipe from the tip opposite to the glass wool. Finally, the reactor is sealed by inserting another plug of glass wool, so that the powders will not be dispersed outside, but held in the designed position. All the weighting, powders movement and pipe filling have been operated under fume hood as it can be seen in Fig. 28, and have been later sealed with paraffin for being transported back to the Energy Center. The following paragraphs describe the actions and the problems encountered during the running of the tests. More details about the geometries and materials of each test can be found in chapter 5 when explaining the temperature simulation.

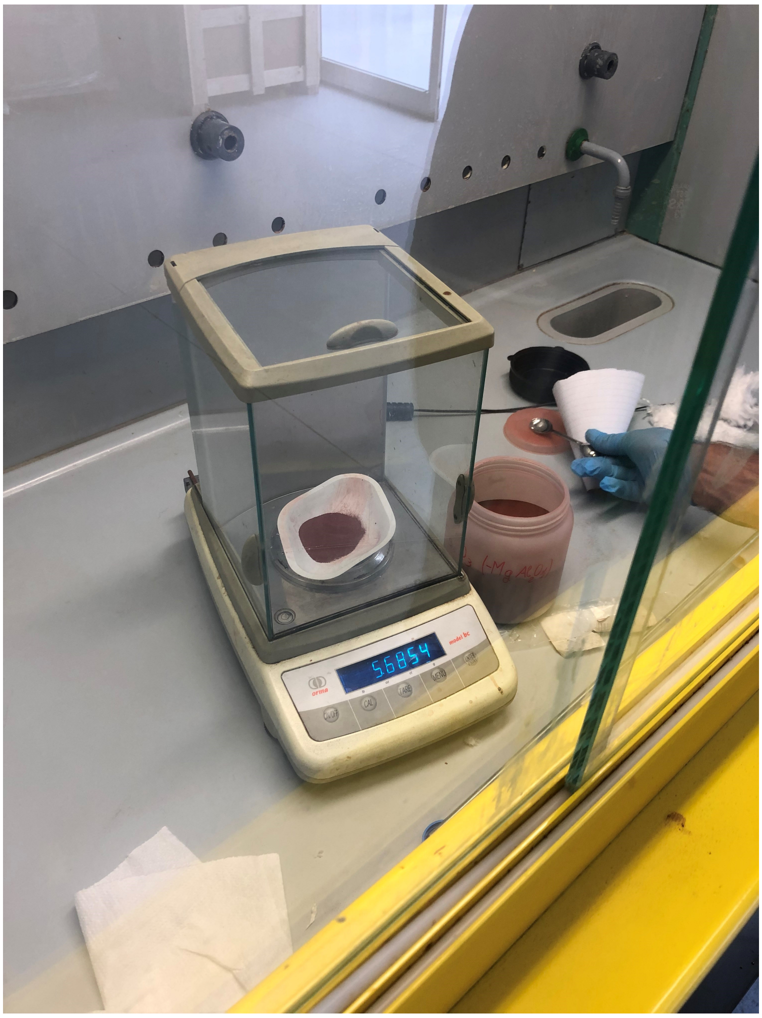

Figure 28 – Hematite powder has been weighted with a precision balance under a fume hood. The picture shows the instruments used in this operation: balance, inox steel spoon and a piece of paper used as funnel for inserting the powder in the pipe.

4.1 Tests #1

The first test was conducted on the 25th of June 2021. The research team prepared the experimental setup in the morning and then the test was run in the early afternoon to exploit the highest sun radiation available.

First of all, the test required another analytic tool by Emerson, in order to evaluate the gaseous mixture composition coming out of the reactor. Therefore, an additional measurement tool was brought from the Environment Park, the X-STREAM process gas analyzer. It works for multi-component analysis, using non-dispersive infrared, ultraviolet, and visible photometry (NDIR/UV/VIS), paramagnetic and electrochemical oxygen (pO2/eO2), and thermal conductivity (TCD) sensor technologies, as well as trace oxygen (trace O2) and trace moisture (trace H2O) for consistent, precise process gas measurement [51]. Because of it, it also turned out to be necessary to change the solvent gas from argon to nitrogen. In fact, argon as a gas might be interfering with the chosen analytics, while nitrogen is more suitable as it does not undermine the quality of the measurements.

After this changes to the gas tanks and metering tool, it had been necessary to calibrate the gas flow meters of the cabinet, to be sure the sample was receiving the correct quantities of gas. To do this, an external instrument was used to measure volumetric and standardized gas flow in the pipe coming out of the pipe exiting the reactor. This means the calibration was effectuated with an empty alumina tube already in place, and by checking the flow after the coming back to the cabinet. The calibration proceeded by setting some volumetric flows on the cabinet controller computer and checking what the flow measured by the other instrument effectively was. The tool used for the calibration is the Definer 220 by Mesa Labs. Its manual reports a volumetric flow accuracy of 0.75% and standardized flow accuracy of 1% of reading [52]. After collecting different points and correlating the set mass flows with the measured ones, it has been possible to understand what was the value to be set on the cabinet controller to effectively have the desired flow output. This procedure has been repeated for both methane and nitrogen. Next, the empty pipe was substituted with a reactor charged with hematite with an L/D ratio of 2, therefore 3.79 g. The pipe edges have been folded with teflon to ensure a better sealing during the operation and the reactor was inserted in the support. A few changes were made also in the general layout of the solar paraboloid to make it more useful for this test's purpose. The B-type thermocouple was extracted from the inside of the pipe and was placed on the external surface, reaching with its tip the focal point. This exposed it to a much stronger heat flux and more variable conditions. This change was made because it was not possible anymore to keep it inside the pipe, due to its volume (the concerns are related to the fact it would interfere with the glass wool and reaction bed and would cause a pressure increase in the gas flow). Moreover, an external thermocouple would be able to record the effective temperature the pipe is exposed to, rather than the of course lower one that is reached inside of it. Then, an

Figure 29 – Final setup for test #1, performed on the 25th of June. The external B-type thermocouple can be seen held by a wire.

additional N-type thermocouple was inserted in the reactor until the glass wool thanks to its reduced diameter. The final setup for test #1 is reported in Fig 29.

After the setting up, the void pump was activated by the command on the controller to extract all the air in the line and check whether the sealing was effectively separating the reaction environment from the external environment. The pressure difference measured was around -70 bar, indicating a sufficient sealing of the line.

After the setup was fully completed, the solar concentrator was switched on and set on automatic mode at 13:25. The parabolic was quickly oriented towards the Sun and the temperature started growing extremely quickly. In fact, the measured temperature jumped from 3.40°C when not oriented (as the thermocouple is designed for working at high temperature, it is quite normal the value read when not operating is not accurate)

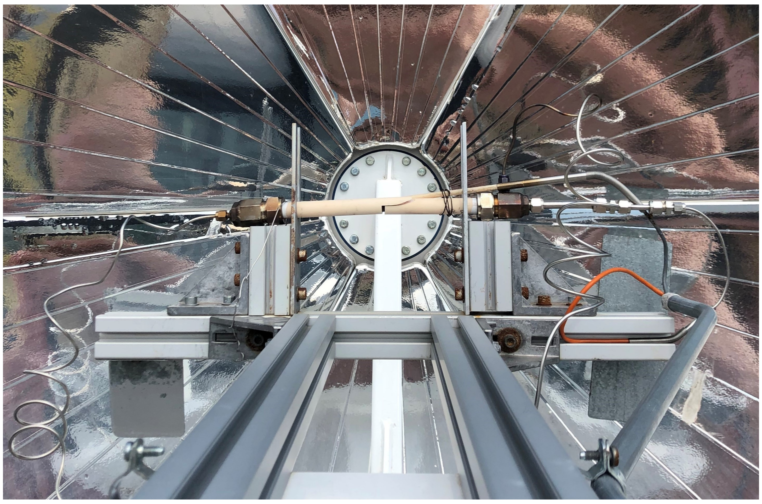

Figure 30 – Picture showing the ceramic fracture of the pipe. The edges are sharp and the pipe was divided in only two pieces that perfectly match.

to 883.65°C in a minute. After one more minute, at 13:27, the measured temperature reached even 1077.31°C.

At 13:42, gas flows started according to the calibration previously undertaken. The system started injecting 91 sccm of CH_4 and 165 sccm of N_2 (the flows set on the computer controller were 86 and 224 sccm respectively). Unfortunately, when the gas flows were switched on and the recording of the test started, the analytic connected to the output of the line kept on measuring air concentration of oxygen for the whole duration of the test. Moreover, no CH_4 was detected. After more than one hour of running the test, at 13:57, the solar concentrator was switched to its initial position and turned off. The pipe was found broken into two by a sharp ceramic fracture, as it can be noticed from Fig. 30, explaining the reason why the analytic was measuring oxygen in the mixture.

The reason of the failure of the test was thought to be related to the extremely fast heating up of the reactor, which was not present in the literature, when the material was heated up more slowly by following a maximum of 150°C/min in the oven according to the website of an alumina producer [53]. As it can be understood in Appendix A.1, by Fig 60, the heating up ramp before reaching a more or less stable value of temperature, is around 500°C/min, with a peak of more than 800°C/min during the first minute. Therefore, the research team decided to try solving the problem before setting up a new test.

4.2 Test #2

To avoid a rapid increase of the temperature as it happened during test 1, it was decided to prepare and mount the reactor the night before the test day so that the solar collector, by following the natural Sun path in the sky from dawn to sunset would not experience extremely fast heating up that might compromise the mechanical properties of alumina. For doing so, it had been necessary to modify the position of the sensor of the end-of-stroke. In fact, when the technical team of El.Ma. Srl installed the machine, they could not orient the solar concentrator perfectly toward East as the foundation of the machine had to respect the orientation of the rooftop. To overcome this problem, a horizontal offset of -26.43° has been set on the controller. Anyway, this solution caused the activation of the solar concentrator as soon as the azimuth is lower than the offset. In summer, the Sun path in the sky is longer as the dawn is earlier and beyond East, and the sunset is later and beyond West. Therefore, this caused the elevation of the Sun to be already quite high when the starting azimuth is reached (and the day already advanced). Moreover, because of DST, this phenomenon is even postponed of one hour. The solar concentrator was therefore not exploitable before around 11 AM and when it was finally able to start, it reached immediately very high temperatures (as the Sun was already quite high in the sky). This fact did not allow the reactor to be heated up gradually, but rather to experience strong gradients. To solve this issue, as already mentioned, it had been necessary to move of the same angle as the horizontal offset the sensor indicating the end-of-stroke. A new hole has been drilled in the correct position and the sensor was moved there. This operation finally allowed the machine to start earlier in the day, to avoid extremely high temperature ramps.

On July 1st the experiment was repeated with some differences from test #1:

- The reactor was charged with hematite that was previously thermally treated (it was kept at 600°C for 6 hours), to be sure the whole sample was completely oxidized;
- The L/D ratio was moved to 1.5 to use a lower quantitative of powders, therefore

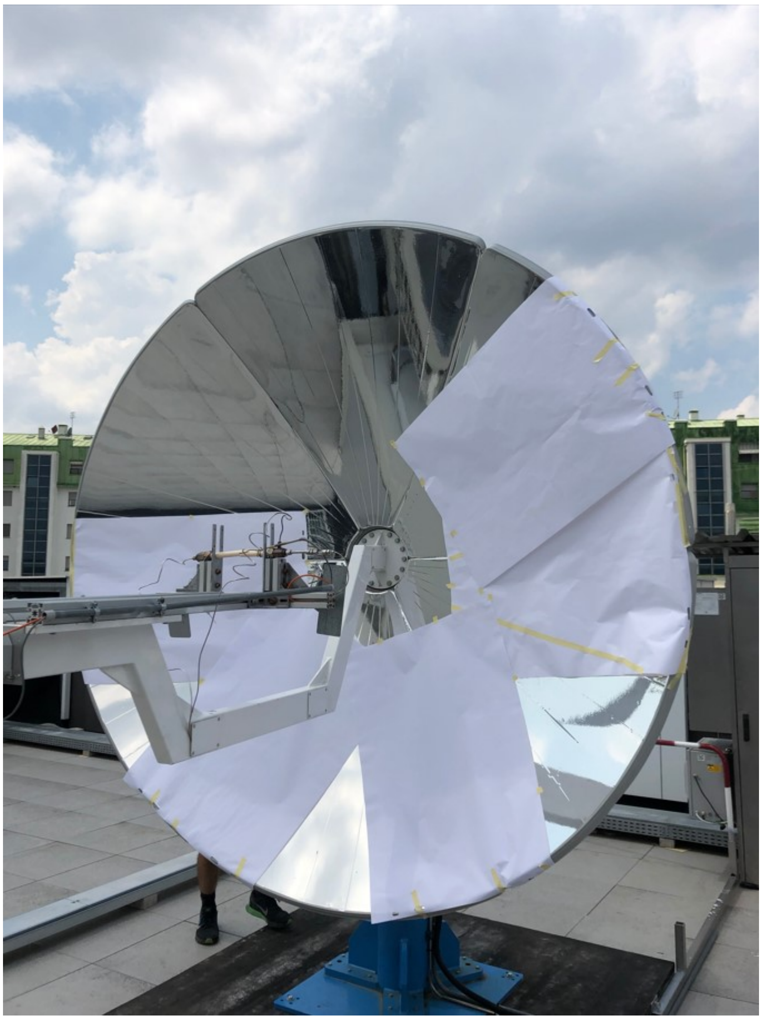

Figure 31 – Picture showing the white sheets of paper used for shading the reflective surface for test #2 (performed on 1st of July). By slowly removing the papers when the solar concentrator is working, it is possible to have a more controlled increase of the temperature.

2.84 g of hematite;

- The temperature growth was controlled as much as possible, and the reactor was already in place since the day before.

To reduce extremely fast temperature ramps, the reflective surfaces of the mirrors were partially covered by white paper sheets, as explained by fig. 31. This can decrease the incoming heat flux on the focus and subsequently, by slowly removing one paper by one, allow a controlled increase of temperature. The inauspicious formation of a cloud caused a sharp decrease of the temperature from 976°C at 13:49 to 819°C in only one minute and then reaching even 654°C at 13:57. The test was started at 14:09, as soon as the thermocouple reached again more than 800°C.

The operations already described in test 1 were repeated, but once again, the analytic kept on detecting atmospheric oxygen concentration. The test was ended at 15:12, meaning that the gas flows were stopped. Later, the concentrator was brought back to its safety position. One more time, the reactor was found broken by a sharp crack in the focal point, similar in everything to Fig. 30.

4.3 Test 3

The failure of the previous test highlighted the fact the alumina pipe was not handling well the high temperatures, and the fact that even the passage of a cloud might have damaged the its integrity. Therefore, it has been suggested to try using a different material for the reactor pipe, more able to withstand extreme temperature gradients. Subsequently it has been decided to try another test using a conductor material for the pipe, such as steel, in particular, AISI 316. In fact, the temperatures measured by the thermocouple during test 1 and test 2 were still compatible with the melting temperature of this alloy, which is around 1370-1398 °C according to [54].

Test 3 was performed on July 9th. The reactor was charged with 2.7 g of thermally treated powders (L/D=1.5) and was mounted on the support on the day of the test. To prevent thermal conduction between the reactor pipe and the support, pieces of alumina have been used to thermally decouple them. Additionally, the calibration of the gas flows has been repeated by using the Definer 220 after the analytic, so checking the gas coming out of the last step of the line. Once again, different measurements have been collected and it has been possible to build an interpolation curve, as it can be seen in figure 32. The tests is similar to the previous ones with alumina as it made use of the same thermocouples.

The test started at 13:01 by flushing pure N_2. At 13:05, the percentage of oxygen detected by the Emerson Analytic fell under 0.05%. At 13:15 methane started being injected in the pipe in the aforementioned quantities. Injecting the methane caused an increase of the static pressure inside the reactor (from 8 to 15 mbar). At 13:28, the measured

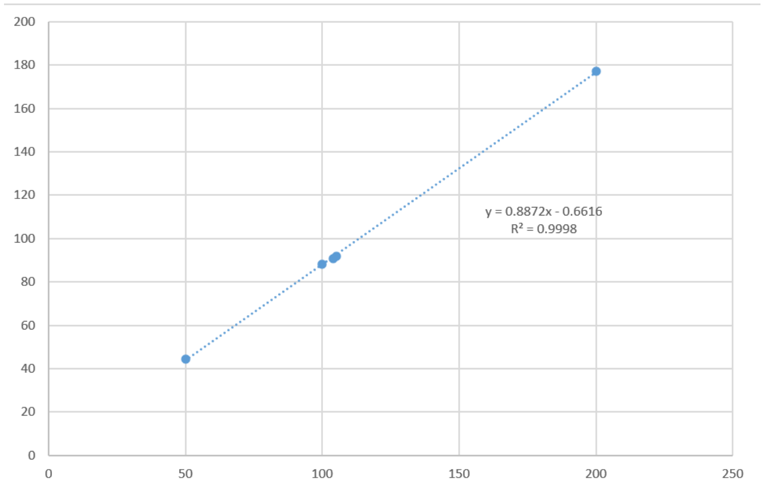

Figure 32 – Interpolation correlating measured and set values of mass flow of CH_4.

quantity of oxygen was 0.17%. At 13:29 the temperature indicated by the sensor reached more than 900°C and pressure dropped to 0.13 mbar. One minute later, the temperature decreased to 138°C. After floating around 150°C, at 13:49, the temperature measured a value of 2145°C (out of scale). The test was stopped at 13:50 and the pipe was later found broken. Nevertheless, this test made it possible to collect interesting data on the reaction as it had been possible to detect the presence of H_2. Fig 33 summarizes visually all the stages of the test, from the initial injection of N_2, subsequent injection of CH_4, rupture of the pipe and loss of pressure (and wrong data collected from the external temperature). Fig. 34 instead, plots the concentration of the gases leaving the reactor. A few comments are necessary about these data:

- As soon as the methane is injected, H_2 is released and quickly reaches $4.5*10^5$ ppm(v) (around 45%).
- CH_4 instead, decreases and then increases again, to reach a plateau at $1.0*10^5$ ppm(v) (around 10%).
- CO is released immediately tipping 10% of the mixture, but then rapidly goes back to 0.
- CO_2 follows a similar pattern, but starting from a much lower peak (1.5 %).

Initial peaks measured before 13:00 are to be considered as leftover gases in the line flushed away by the nitrogen injection. After the loss of pressure, methane goes to 0, as

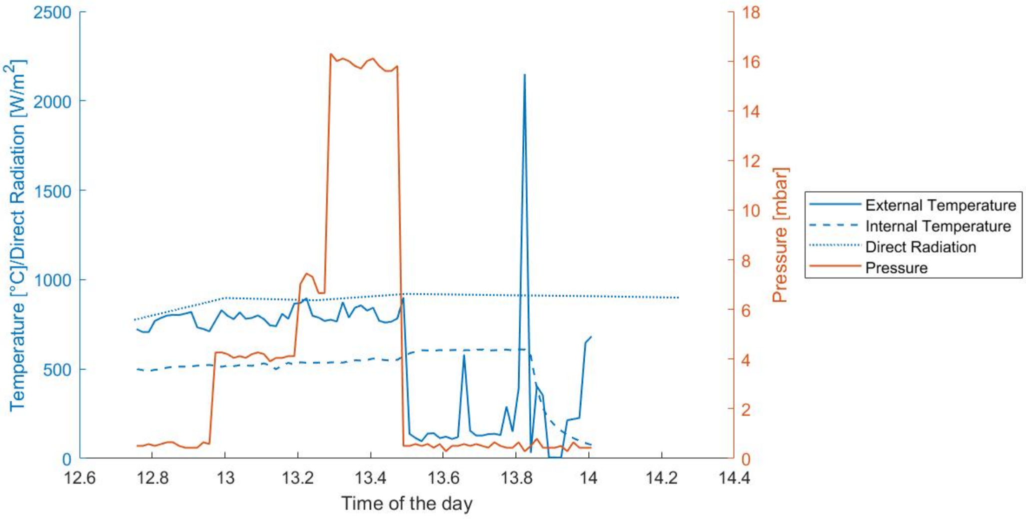

Figure 33 – Internal and external temperature, direct radiation on the normal plane and pressure recorded during test #3 (performed on July 9th). It is possible to notice the errors in monitoring the temperature due to the probable damage of the thermocouple.

the whole quantity is burned when exposed to air. Values recorded after that moment might not be accurate anymore as the line was probably not experiencing any flow, but rather a static gas mixture. Oxygen started increasing again after a while.

The rupture of the tube is completely different from the ceramic fracture of the reactors used in test #1 and test #2. Here, the behaviour is far from the ceramic one, but observing Fig. 35, it looks like the pipe wall melted. In fact, the hole presents an irregular elliptic shape, resembling the focal area hit by the concentrated light beam. The surroundings are weakened and darker, while going further from this point steel looks untouched. The unlucky break of the reactor happened more quickly than in test #3, when the same material was used. This could be due to the reduced dimensions of this pipe, which therefore gets heated up much faster, as it will be explained in chapter 5.

4.4 Test 4

As test #3 was the first one in which it was possible to observe a reaction occurring, it has been decided to repeat it in similar conditions, although risking another rupture of the pipe. This time, the pipe used was another again made of steel AISI 316, but with

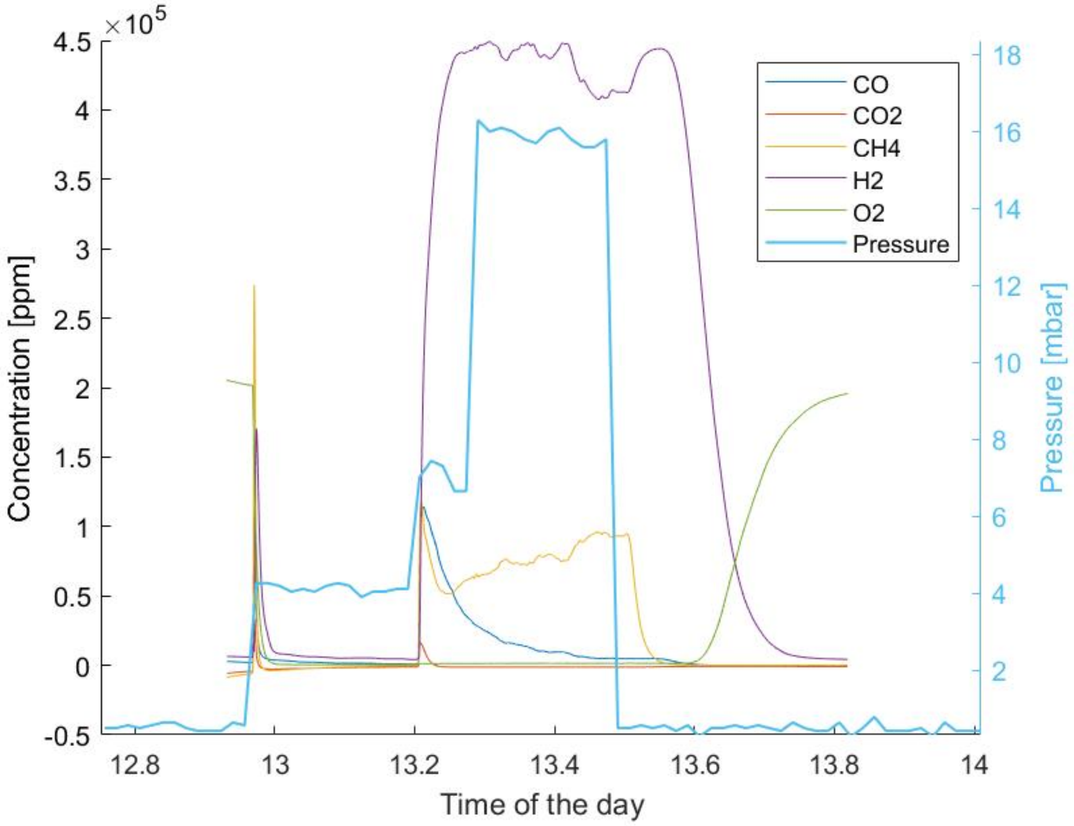

Figure 34 – Ppm concentration of the gaseous mixture outflowing the reactor during test #3 (performed on July 9th).

a lower diameter (internal diameter=0.771 cm). Pieces of alumina were used to avoid it touching the metallic tube holder. The reactor was charged with 0.53 g of thermally treated powders, accordingly to the L/D ratio of 1.5. Two N type thermocouples were used for this test. The external one was twisted around the tube, so that the tip would touch the focal area. The internal one was mounted on the support and run inside the pipe until touching the glass wool plug. Fig. 36 shows the final setup of the experiment. According to the calibration performed for test #3, the quantities set on the controller for flushing the right amounts of gases were: 292 smcc of N_2 (for sending 169.5) and 104 smcc of CH_4 (for sending 90.9). The date of test #4 was the 20th of July.

As it can be noticed by fig. 37, N_2 was flushed into the pipe since 12:00, before switching on the solar concentrator. The orientation of the paraboloid towards the sun caused an immediate increase of the internal and external temperature. Despite a sudden decrease of both internal and external temperature right after 13:00, at 13:13 the controller detected complete pressure loss. At 13:15 the external thermocouple broke down,

Figure 35 – Picture of the AISI 316 pipe used for test #3 (performed on the 9th of July). The hole has been produced by the intense heat concentrated on the focal area, which melted the pipe wall.

indicating the out of scale value. Nevertheless, the test was not stopped and at 13:29 CH_4 was flushed inside the pipe. The reaction occurred anyway to some extents: fig. 38 indicates a slight increase in the detected level of H_2, although an increase of O_2 as well, meaning the pipe was not sealed anymore.

The rupture of the pipe, revealed by the loss of pressure and later observed when the concentrator was shut down, can be seen in fig. 39.

Figure 36 – Final setup of test #4 (performed on the 20th of July). Both thermocouples used are N-type ones. The external one is twisted and warepped around the pipe.

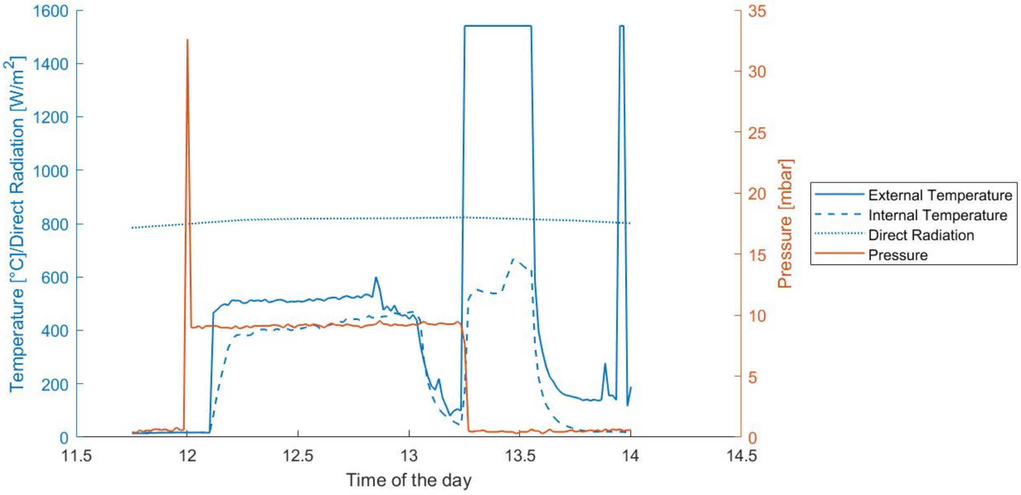

Figure 37 – Internal and external temperature, direct radiation on the normal plane and pressure recorded during test #4 (performed on July 9th). It is possible to notice when the external thermocouple got broken and suddenly peaked to 1500 °C.

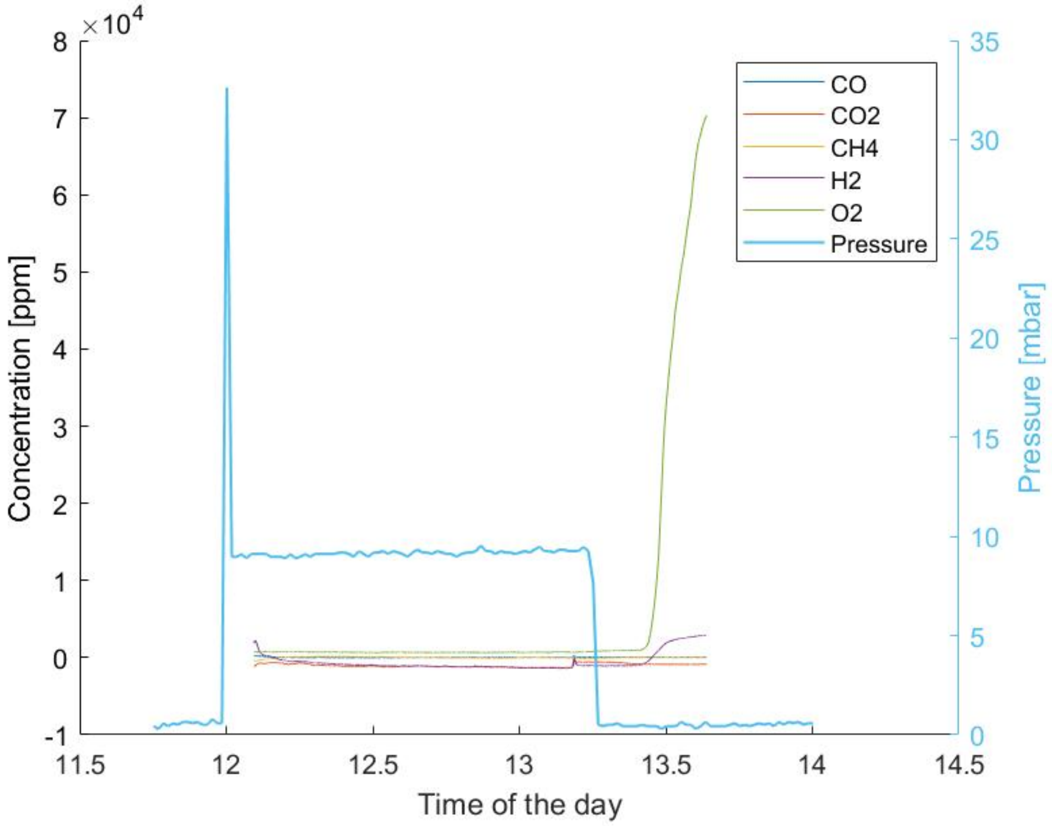

Figure 38 – Ppm concentration of the gaseous mixture outflowing the reactor during test #4 (performed on July 20th).

Figure 39 – Picture of the reactor after test #4. The area of the pipe hit by the most concentrated solar radiation (the focal area) is missing the tube wall. Instead a hole with elliptical shape is found and the materials placed inside looked completely burned and destroyed by intense heat. Edges of the hole look like there have been a melting process, but the pipe is still made up o only one piece. The thermocouple looked damaged by the melted steel.

4.5 Test 5

As the previous test did not allow to obtain a sufficient amount of data on the reaction, the test was repeated one more time. As a big problem in the performing was clearly represented by the resistance of the material to those high temperatures, a different material was selected. While a ceramic material such as alumina was probably not suitable because of the high temperature gradients, a metallic material such as AISI 316 was not suffering because of them, but more probably because the solar concentrator was able to reach, at least in the focus, a temperature close to the melting point of the steel. Therefore, it has been decided to go for a high temperature resistant alloy, usually applied for processes at extremely high temperatures. A pipe of Inconel Hastelloy c276 was used and modified in order to fit into the supports. Keeping the L/D ratio of 1.5, the reactor was charged with 0.865 g of thermally treated powder. The calibration was repeated and the quantities set on the controller were fixed at 281 smcc for N_2 (for sending 169.4) and 109 smcc for CH_4 (for sending 90.0). The test was repeated a few days later, on the 23rd of July.

The pipe was flushed with N_2 since before switching the solar concentrator on. Due to the atmospheric conditions, the growth of temperature was not so quick that day, and the internal thermocouple struggled to reach 400°C. The direct radiation was indeed quite low, as it can be seen in fig. 40, and a layer of clouds and haze caused a strong diffusion of the light. Despite this low concentration of the beam, at 12:10, smoke was seen around the reactor. The concentrator was switched off and returned to its safe position (decrease of temperature in fig. 40). No rupture was noticed, and therefore the test was continued. CH_4 started being flushed with the pipe in the safe position, as it can be noticed from fig. 40 (pressure increase happens while T is still low). Fig. 41 therefore, shows how this time, H_2 does not immediately reaches its higher point, and a higher amount of methane is still present. At the beginning in fact, the tool is detecting almost 35% of CH_4, therefore meaning that at those temperatures, the reaction was not happening at all. Then, with the increase of T due to the switching on of the concentrator, levels of CH_4 started decreasing in favour of H_2, that reached 25 %. CO and CO_2 followed the same path as in test #3. At 12:23 the loss of pressure indicated the

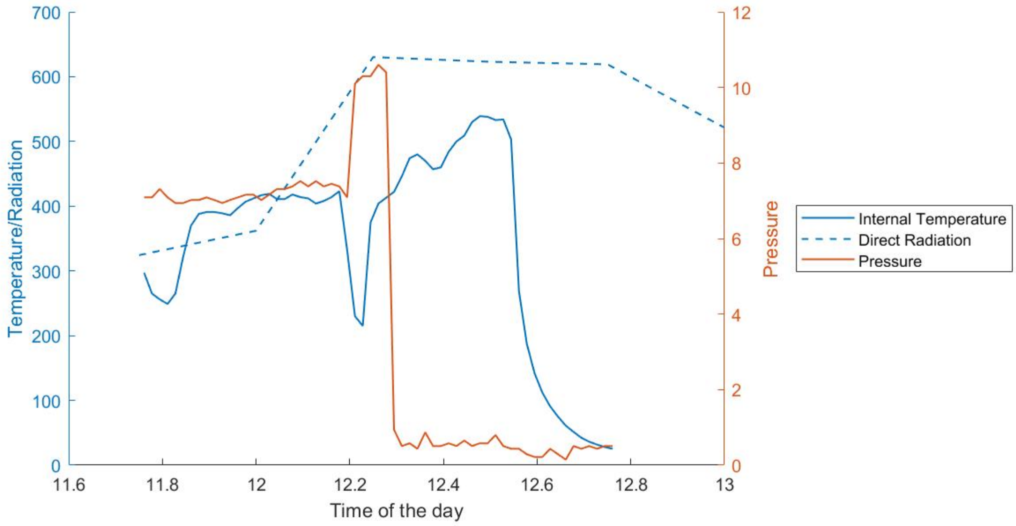

Figure 40 – Internal temperature, direct radiation on the normal plane and pressure recorded during test #5 (performed on July 23rd).

rupture of the pipe. A flare coming out of the hole has been noticed, clearly showing the switch of the reaction from reforming to combustion (due to the exposure to air). Data after the rupture are not significant and not shown here.

The rupture of the pipe can be seen in fig. 42. Although again very far from the ceramic behaviour, hastelloy did not melt the same way as AISI 316, but it rather underwent a flaking process. In fact, the pipe wall started peeling off losing layers of material. The hole edges indeed, do not look like pipes of test #3 and test #4, but more as a results of weakening process. The hole once again shows an elliptical shape.

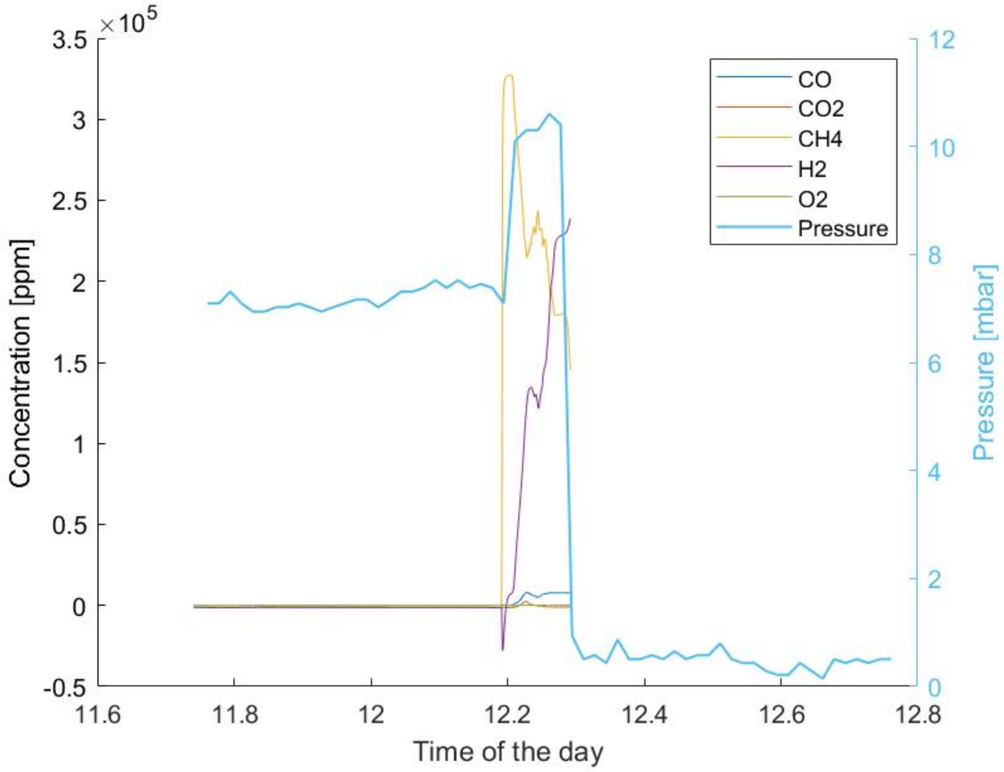

Figure 41 – Ppm concentration of the gaseous mixture outflowing the reactor during test #5 (performed on July 23rd).

Figure 42 – Picture of the experimental setup after running test #5 (performed on 23rd July). The rupture is due to a loss of material in the focal area, while the rest of the pipe did not undergo melting.

5

SIMULATIONS

To better understand which are the most important parameters involved in the studied phenomena, the experiments were replicated in a virtual environment. This chapter is dedicated to explaining how the models of the experimental setup are built and to comparing the simulations results with the real ones. This phase of comparison is fundamental for checking whether the model is effectively representing the truth. In fact, a model has to approximate the real phenomenon, so that it can be used for exploring more in detail what happens when other parameters are changed. In this sense, a simulation can be extremely useful as it expands the real experiment to other aspects that maybe can not be studied in the real case because of constraints of whatever nature.

5.1 Temperature Simulations

The tests performed highlighted the important issue of not being able to measure the temperature in the reactor bed, i.e. where the iron oxides are located. This happens simply because inserting a thermocouple in there would surely modify significantly the gas flow and substract space necessary for the reaction. Therefore, a few simulations where performed on Comsol Multiphysics to develop a tool able to predict the temperature in the reactor bed. To evaluate the efficacy of the simulations, the obtained temperature distributions were compared to the temperature data available thanks to the experimental test. A value of T close enough to the recorded external or internal one (or both, if available) suggested the goodness of the representation of the simulation. Hence, it might be sensed considering the temperature distribution in the reactor bed as meaningful as well.

As the main scope of these simulations is to get a distribution of temperature inside and on the external surface of the reactor, the only two physics used in the software were "Heat Transfer in Porous Media" for obtaining the heat transfers and temperature distribution and "Chemistry" for the thermochemical properties of the ideal gas mixture flowing inside. The fluid dynamic part of the simulation was intentionally neglected (apart from imposing a value of velocity of the flow inside the pipe). In fact, due to the low flowrate imposed in the tests and the enormous amount of solar power collected, the effect on the temperature distribution appeared to be negligible both from the simulation and experience. Indeed, when starting the flowrate of nitrogen no significant decrease of temperature was noticed. Therefore, the simulations were run without the fluid dynamics physics to require a much lower computational power and time.

The general equations used by the software are the following:

$$(\rho C_p)_{eff}\frac{\delta T2}{\delta t}+\rho_f C_{p,f}u\nabla T2+\nabla q=Q+Q_{vd}. \tag{5.1}$$

$$q=-k_{eff}\nabla T2 \tag{5.2}$$

Where ρC_p is the effective volumetric heat capacity at constant pressure, and u is the velocity imposed considering mass conservation. Q is, in this case, the heat source, i.e. the incoming solar power, while q is the heat flux generated in the medium because of the conduction of heat. $Q_v d$ is the heat generated for viscous dissipation.

More in particular, the software uses different equations for the solid, fluid and porous domains of the system. Indeed, it can modify general equation 5.1 to adapt it to each case. Solid is characterized by conduction:

$$\rho C_p\frac{\delta T2}{\delta t}+\rho C_p u\nabla T2+\nabla q=Q+Q_{ted} \tag{5.3}$$

$$q=-k\nabla T2 \tag{5.4}$$

Q_{ted} is the heat generated for thermoelastic damping. In the case of the fluid, it must be remembered that the density is obtained through the ideal gas equation:

$$\rho=\frac{p_a}{R_s T} \tag{5.5}$$

Table 8 – Different geometries used for every test.

Test	Geometry
1	Alumina
2	Alumina
3	AISI 316 1
4	AISI 316 2
5	Hastelloy C-276

For the porous medium instead:

$$(\rho C_p)_{eff}\frac{\delta T2}{\delta t} + \rho_f C_{p,f} u \nabla T2 + \nabla q = Q + Q_{vd} \tag{5.6}$$

and both heat capacity and conductivity are weighted on the solid and fluis parts, considering that Θ is the volume fraction of solid material in porous media and 4ϵ is the porosity.

$$(\rho C_p)_{eff} = \Theta_s \rho_s C_{p,s} + \epsilon \rho_f C_{p,f} \tag{5.7}$$

and

$$k_{eff} = \Theta_s k_s + \epsilon_p k_f + k_{disp} \tag{5.8}$$

As not only one, but 5 different tests have been carried out during the experimental part, more than a single simulation have been performed in order to better approximate the different aspects of the tests.

In particular, 4 different geometries have been built on COMSOL to resemble the different reactors used as it is explained in table 8. The boundary conditions imposed comprehend:

- Incoming heat flux on the focal area, a circular shape located at the medium point of the pipe with a diameter given by equation 2.21. The heat flux have been imposed to be a second derivative of the heat flux over surface. The value set in each simulation depends on the value of direct irradiation detected in the corresponding test. To understand if the simulations are effectively representing the reality, it is necessary to impose the same conditions as during the real tests. The value of direct radiation is multiplied by 2000 which has been assumed to be a conservative value for the concentration ratio, as stated by [12], see Fig. 46.

Table 9 – Diameters and velocity component parallel to the pipe axis.

Geometry	D_i [cm]	u
Alumina	1.402	0.045
AISI 316 1	1.537	0.037
AISI 316 2	0.771	0.15
Hastelloy C-276	0.900	0.11

- The remaining external surface of the pipe has been considered as dissipating heat for forced external convection as an horizontal cylinder in cross flow with a speed velocity of 2 m/s (as the average wind speed).

- Inflow and outflows have been imposed at the edges of the pipe. A medium velocity of the fluid has been imposed considering an average volumetric flow of 400 scmm with different internal diameters of the pipes as listed in table 9. The assumption is that, due to low pressures at which the system is operating, the gas could be considered as almost uncompressed.

- Thermal insulation on the solid edges of the pipe.

The domains of the geometry have been set to be as closer as possible to the real case:

- The central part, hosting the powder has the shape of a short cylinder with the L/D ratio of 1.5. The quantity of charged powders follows considering hematite powder density. It has been modelled as a porous medium, as it can be seen in Fig. 43.

- Two cylinders of glass wool hold the powder in the central part. They are 2.5 cm long in each geometry and modelled as a porous medium (Fig. 43).

- The remaining internal part of the pipe is modelled as a fluid (nitrogen) with a velocity in the axial direction, see Fig. 44.

- The pipe itself is considered as a solid. The material depends on the simulation, see Fig. 45.

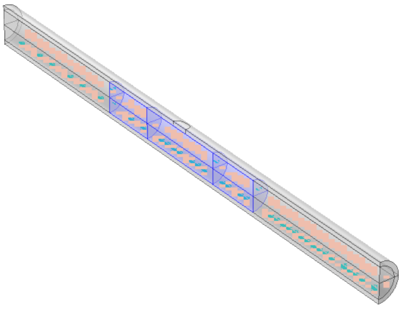

Figure 43 – Porous domain of the geometries.

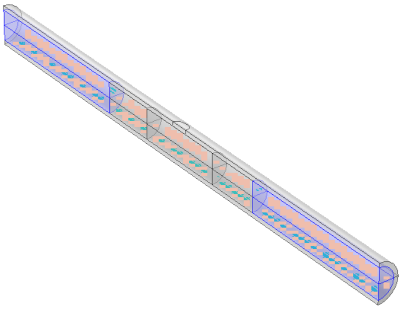

Figure 44 – Fluid domains of the geometries.

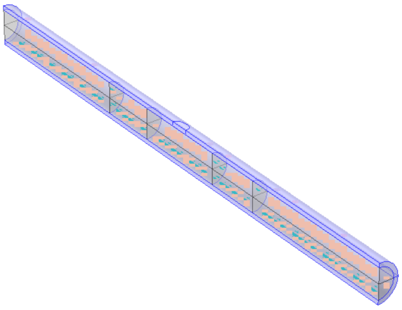

Figure 45 – Solid domain of the geometries.

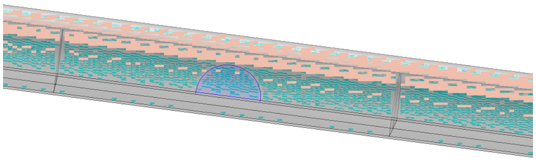

Figure 46 – Area receiving the incoming solar heat flux.

5.1.1 Alumina

The alumina reactor has a simple geometry with an internal diameter of 1.402 cm and external diameter of 1.806 cm as it can be seen in Fig. 47. The results of the simulation were to be compared with the measurements from test #1 and test #2. Test #1 was in particular the most interesting from the point of view of the temperature recordings, while test #2 was run with partial shading of the reflective surfaces and control of the increase of the temperature. Therefore, data for the direct irradiation and wind speed have been retrieved from the averaged values recorded during the tests. As the alumina has a very low thermal conductivity, the simulation has been run for 2 hours, to allow the material to distribute the heat and reach a more stationary situation. Data are summarized in Table 10. The results of the simulation are shown in Fig. 48. The simulation seems to be effectively representing the reality. Indeed, the area directly hit by the incoming solar flux reaches more than 1300 K, and from the measurements, as it can be seen in appendix A.1, temperature reached around 1300K in the focal point.

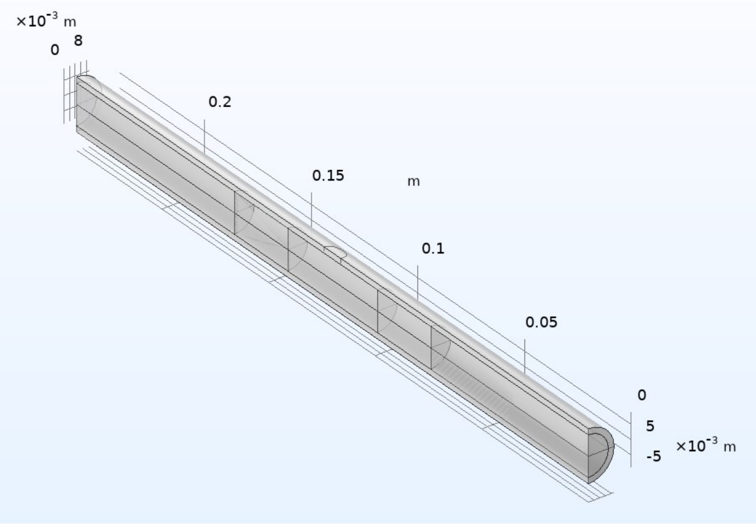

Figure 47 – Sketch of the geometry built for the alumina pipe reactor.

Table 10 – Main data used for the simulation.

Definition	Symbol	Value	Unit
Internal diameter	D_i	1.402	cm
External diameter	D_e	1.806	cm
Pipe length	l_p	24.5	cm
Direct irradiation	I	900	W/m^2
Wind speed	u	1.89	m/s
Simulation time	t	120	min

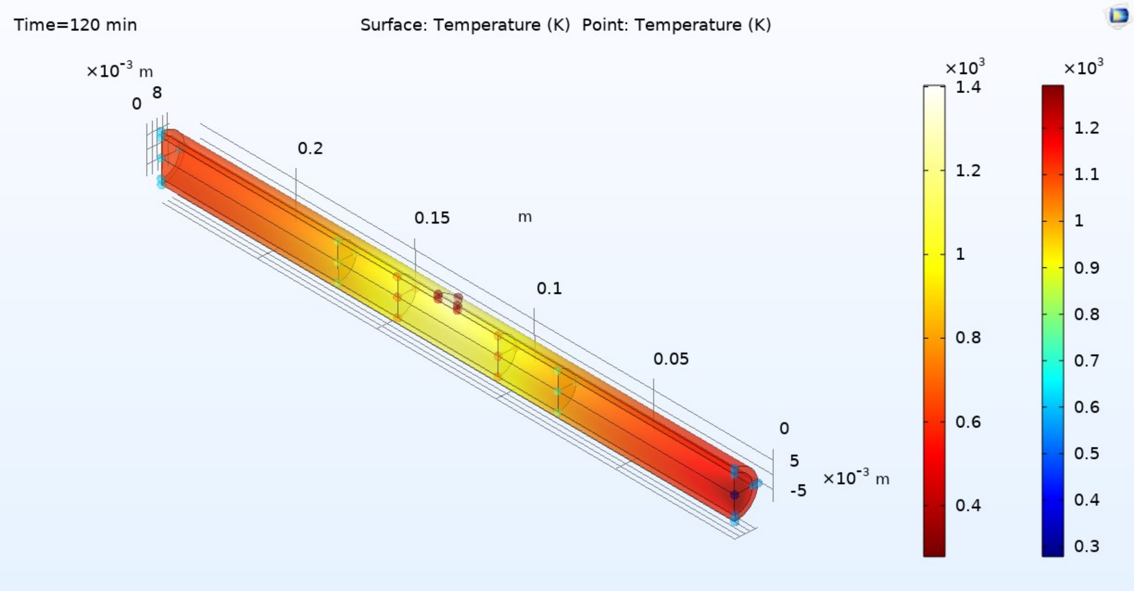

Figure 48 – Temperature distribution of the temperature field obtained with the data of Table 10.

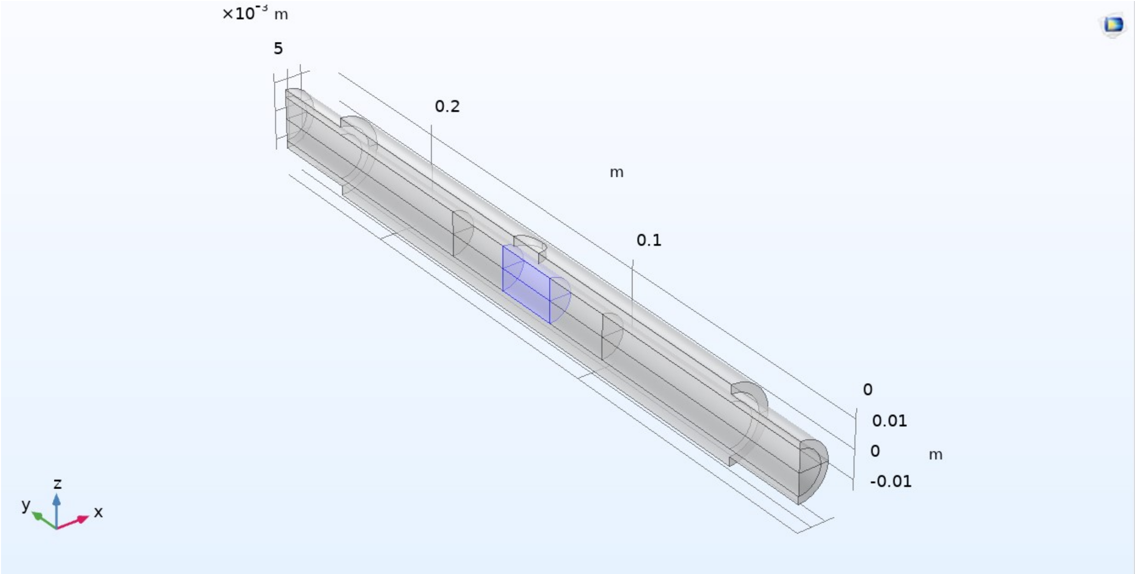

Figure 49 – Sketch of the geometry built for the first AISI 316 pipe reactor.

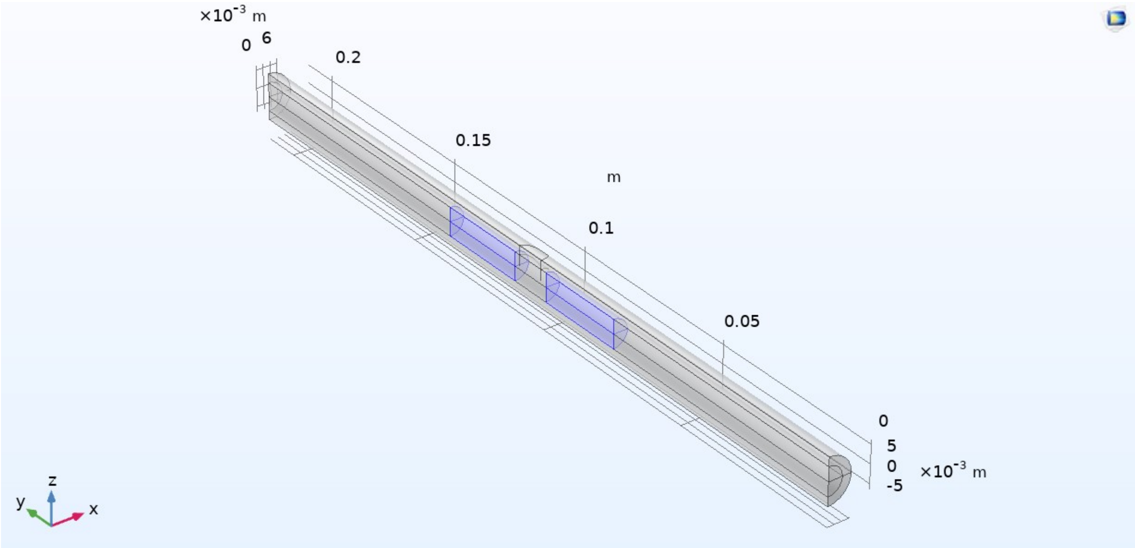

Figure 50 – Sketch of the geometry built for the second AISI 316 pipe reactor.

5.1.2 AISI 316

The two pipes made of AISI 316 used in test #3 and #4 had different geometries (see Fig. 49 and 50. Therefore, two different simulations were conducted to better approximate each condition. Once again, data for the average wind speed and average direct radiation are retrieved from measurements of weather conditions during experimental tests. Data used as inputs for the simulations are listed in tables 11 and 12.

The simulation output temperatures similar to the one measured by the thermocouples placed inside and outside the reactor in only in the first simulation.

Table 11 – Main data used for the first simulation with the thicker tube.

Definition	Symbol	Value	Unit
Internal diameter	D_i	1.537	cm
External diameter	D_e	21.20	cm
External diameter at the edges	D_{ee}	1.804	cm
Pipe length	l_p	25.00	cm
Edges length	l_e	2.995	cm
Direct irradiation	I	885	W/m^2
Wind speed	u	1.67	m/s
Simulation time	t	30	min

Table 12 – Main data used for the second simulation with the thinner tube.

Definition	Symbol	Value	Unit
Internal diameter	D_i	0.771	cm
External diameter	D_e	1.26	cm
Pipe length	l_p	21.00	cm
Direct irradiation	I	810	W/m^2
Wind speed	u	1.80	m/s
Simulation time	t	30	min

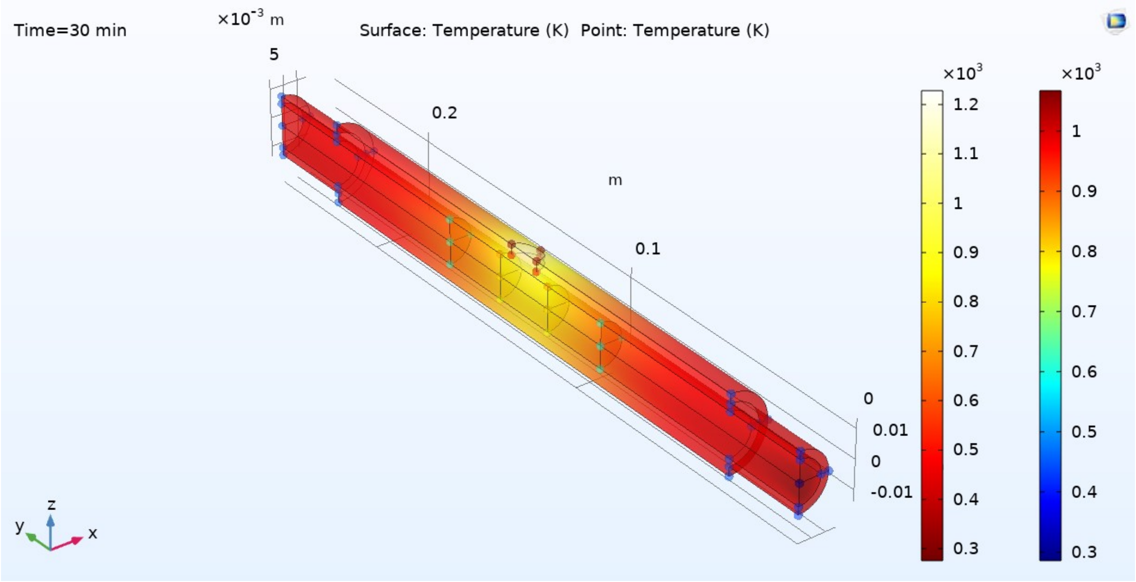

Figure 51 – Temperature distribution of the temperature field obtained with the data of Table 11.

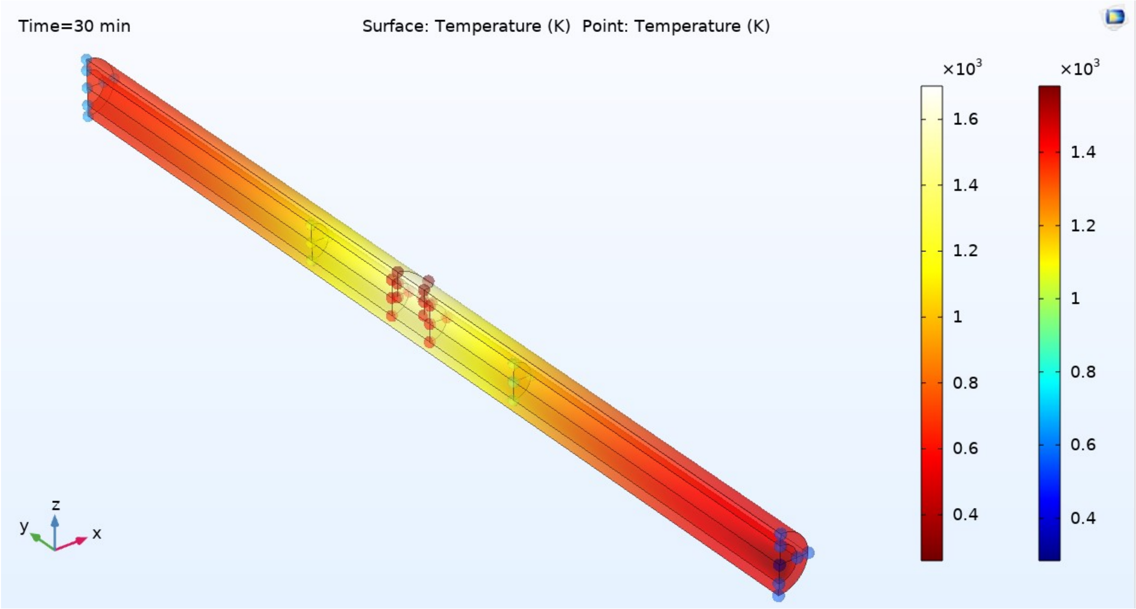

Figure 52 – Temperature distribution of the temperature field obtained with the data of Table 12.

In fact, the temperature obtained in the focal area reached around 1200 K. From the recordings of the external temperature instead, the value reaches around 1160 K before the rupture of the sensor. Looking at the internal temperature instead, from the side where the gas is injected, the obtained value is over 700 K. The recorded one is instead around 770 K. The final temperature field can be found in fig. 51.

The second simulation instead showed much lower values of temperature from the external sensor. This might be probably due to the fact that the tip of the thermocouple was not properly touching the pipe. Anyway, the simulation is outputting quite higher temperature values around the focal area. This might be due to the lower diameter of the pipe, and therefore lower volume of material to be heated up by the solar irradiation. Results are showed in fig. 52. To sustain this hypothesis, test #4 experienced a quick breaking of the pipe which did not let getting any results out of that experiment. In fact, the rupture happened much before test #3, which was run using the same material, but a much thicker pipe.

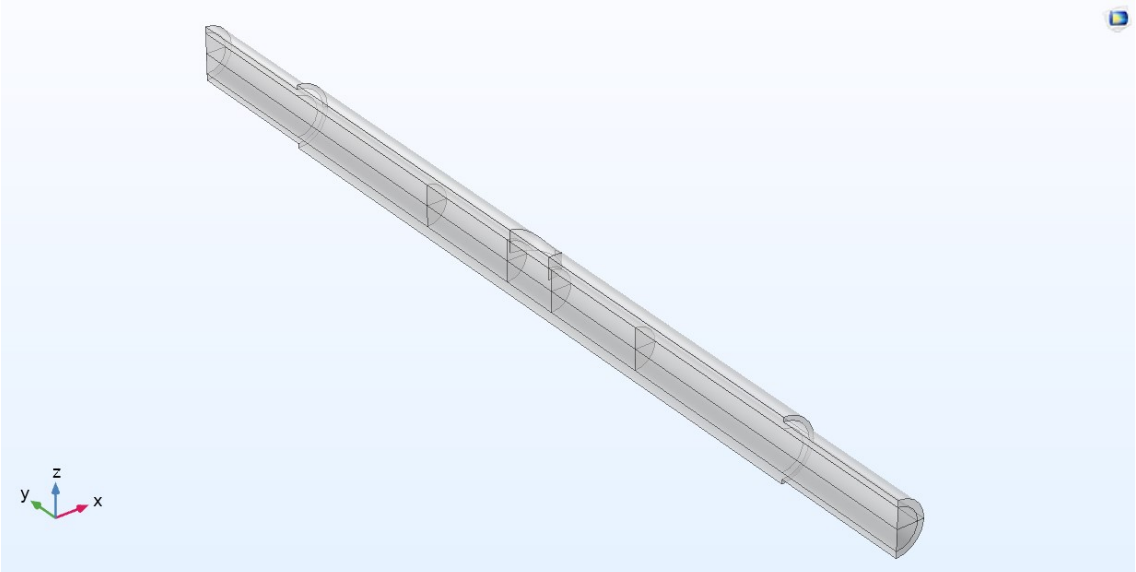

Figure 53 – Sketch of the geometry used for the hastelloy c276 pipe reactor.

Table 13 – Main data used for the simulation with the hastelloy c276 pipe reactor.

Definition	Symbol	Value	Unit
Internal diameter	D_i	0.90	cm
External diameter	D_e	1.385	cm
External diameter at the edges	D_{ee}	1.187	cm
Pipe lenght	l_p	21.00	cm
Edges length	l_e	3.113	cm
Direct irradiation	I	513	W/m^2
Wind speed	u	1.98	m/s
Simulation time	t	30	min

5.1.3 Inconel Hastelloy c-276

The simulation for the pipe in hastelloy c-276 instead, gave more interesting results, and the output values were very similar to the ones recorded in test #5. the geometry is represented in fig. 53 Similarly to the first simulation of the AISI 316 pipe, the diameter has been modified at the edges, in order to make it fit in the supports. Data used as input for this simulation are found in table 13

For this simulation, it has not been possible to install an external thermocouple, therefore the only available data on the temperature was recorded inside the pipe, close to the glass wool plug. Anyway, the values were very similar: in fact, the simulation output a value around 800 K, and the sensor recorded initially a value around 670 K and 770 K after the restarting of the solar concentrator. This can be assumed as a proof of the good

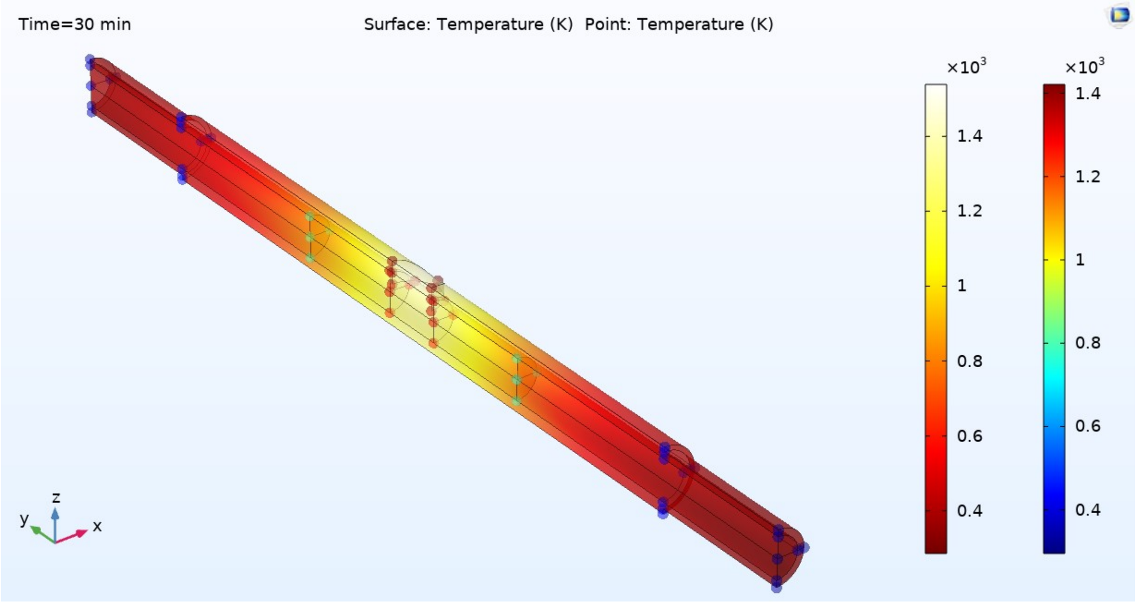

Figure 54 – Temperature distribution of the temperature field obtained with the data of Table 13.

approximation the software is making of the real case.

5.2 Chemical simulation

A second round of simulations has been performed to reproduce the chemistry of the experiment performed in the solar collector. Likewise the temperature simulation, the model has been built and run on COMSOL Multiphysics. The model was chosen to be a 0 dimensional one, making use of the Reaction Engineering physics, for being as lighter as possible from the computational point of view.

The initial model was only loaded with the complete reaction proposed by Monazam et al. [36], that is reaction 3.38. Nevertheless, the reaction alone was not effectively reproducing the empirical results. In fact, the stoichiometry proposed is not close to the detected quantities of gases leaving the mixture: more CO was produced than CO2 and the percentages were varying with time. A more detailed model would therefore have to consider all the parallel reactions happening when those molecules are put together at a very high temperature.

5.2.1 Model configuration

Reaction Engineering physics initially needs to select the type of reactor used and the temperature at which it is working or the energy balance. For the purposes of this simulation, the reactor was considered to be a continuously stirred reactor with constant volume, as it allows reactions between a gas and a solid surface. It is assumed to be perfectly mixed, so that the species concentrations of the exit stream are the same as the concentrations in the reactor volume. The temperature was set to be around 950°C, after the previously run temperature simulation. Then, Reaction Engineering allows to add several chemical reactions happening at the same time. The parameters required by the software are the chemical reaction formula, the overall reaction orders (volumetric and superficial) and the rate constants (using Arrhenius expressions). Since not all of them are always known, or unanimously confirmed by different sources, some approximations were made. All reactions inserted in the model were considered to be irreversible.

$$k = A\left(\frac{T}{T_{ref}}\right)^n exp\left(\frac{E}{R_g T}\right) \tag{5.9}$$

The Arrhenius expression 5.9 is representing the reaction constant by making use of three parameters:

- A, which is the frequency factor, also alled as pre-exponential factor, indicates the frequency of collisions between reactant molecules at a standard concentration, and it depends on the temperature and the activation energy. Moreover, it depends on the rate at which molecules collide and also on the relative orientation they have. Being a frequency, the unit of measure usually is 1/s.

- n, is the temperature exponent. It expresses the dependency over temperature change. It can be set to zero if the other values are referred to the operating temperature.

- E, which is the activation energy, corresponds to the energy barrier that has to be supplied to the reaction to make it happen. In other words, it is the minimum amount of energy that must be provided to compounds to result in a chemical reaction [55]. It does not have to be confused with the enthalpy of the reaction, which is instead related to the quantity of energy released after the reaction happened. The unit of measure is energy over moles, usually kJ/mol.

As the software was now asked to solve a chemical problem, the equations used were different. The equilibrium of the reaction is reached when the Gibbs free energy is minimized. Th Gibbs free energy is defined by equation 5.10, where U is the internal energy, P is pressure, V is volume, T is temperature, S is entropy and H is enthalpy of the system.

$$G(T,P) = U + PV - TS = H - TS \tag{5.10}$$

For reaching the minimum, it is necessary to equal the derivative to 0, knowing that, for a closed system:

$$dU = \delta Q + \delta W = TdS - PdV$$

where δQ is (reversible) heat transfer to the fluid and δW is (pressure) work in the system.

$$dG = TdS - PdV + PdV + VdP - TdS - SdT = VdP - SdT$$

Regarding the CSTR with constant volume, the governing equations are:

$$\frac{d(c_i, V_r}{dt} = \sum v_{f,m} c_{f,m} - v c_i + R_i V_r \tag{5.11}$$

The reactor volume as a function of time should be:

$$\frac{dV_r}{dt} = \sum v_{f,m} - v + v_p \tag{5.12}$$

But, as already mentioned, in this kind of reactor the volume is constant and therefore the volume of the reactor V_r (expressed in m^3) can be taken out of the expression 5.11 and its derivative is posed equal to 0 in eq. 5.12. R_i, expressed in mol/(m^3*s) is the species rate expression, while $c_{f,m}$ (SI unit: mol/m^3) is the species molar concentration of the associated feed inlet stream $v_{f,m}$ (SI unit: m^3/s). v_p (SI unit: m^3/s) denotes the volumetric production rate and is defined by equation 5.13, where M_i, in kg/mol, expresses the molecolar weight of specie i.

$$, v_p = V_r \sum \frac{R_i M_i}{i} = \frac{R_g T}{p} V_r \sum R_i \tag{5.13}$$

Finally, v is the volumetric outlet rate, defined by eq. 5.14.

$$v = \sum v_{f,m} + v_p \tag{5.14}$$

The energy balance was excluded from the simulation, as an operating temperature was set, as previously mentioned.

Because, according to Monazam, the reduction reaction of hematite proceeds through two parallel paths, reaction 3.38 was added twice with the different parameters indicated by the authors. In fact, they suggest there are two reactions, R_1 and R_2 operating at the same time, but with different kinetics, a topochemical and a nucleation and growth process. The first has a frequency factor of 4.759*$yCH_4^{0.636}$, while the second has a frequency factor of 1.33*$yCH_4^{1.06}$ where yCH_4 is the molar fraction of methane in the inlet mixture [36]. Nevertheless, it has been decided not to use the activation energies provided by Monazam, but rather to choose the minimum value provided by Lu et al. [37] of 74 kJ/mol. In fact, activation energy can depend on many properties of the powder such as the dimension of the grains and the type of thermal treatment it underwent. Therefore, very different values can be found in literature, and by trying out some of them in the simulations, the best one was chosen according to to the results obtained by the software. Moreover, the value indicated by Lu et al. [37] is for calcinated magnetite, a process similar to the thermal treatment the powders used for the experiment were prepared with.

In order to take into account the fact that not only complete oxidation is happening, it has been decided to consider the partial oxidation reactions too. That is, the reactions of reduction of the oxides that do not yield directly CO_2 and H_2O, but only CO and H_2. The reactions have the theoretical chemical formula 5.15 and 5.16, according to Lu et al. 22.

$$Fe_2O_3 + CH_4(g) \rightarrow 2FeO + CO(g) + 4H_2(g) \tag{5.15}$$

$$Fe_3O_4 + CH_4(g) \rightarrow 3FeO + CO(g) + 2H_2(g) \tag{5.16}$$

The Arrhenius parameters for the reaction were supposed to be similar to the ones used for R2 by Monazam et al. [36], with an activation energy of 74 kJ/mol.

The other reactions added to the model are the ones explained in section 3.1.5. Methane

decomposition or cracking, 17, that happens at high temperatures, when the methane molecule is directly broken into molecular hydrogen and solid carbon, which is deposited on the substrate. Although it has the positive effect of increasing the quantity of hydrogen released in the mixture, it partially inactivates the powders because of the accumulation of carbon. Values for the pre-exponential factor and activation energy were retrieved from [56], being them 1.3*10^7 mol/(m^2/s) and 214 kJ/mol. This reaction usually happens at quite high temperatures, but the presence of hematite can act as a catalyst for the reaction. The indicated value for energy activation and reaction constant were measured in presence of hematite and is therefore useful for this simulation.
Carbon gasification 3.22 instead, can help cleaning up a bit the substrate as it eliminates solid carbon from the powder by releasing hydrogen and carbon monoxide. The pre-exponential factor over hematite is 1.8*10^4 m/s and activation energy is 172 kJ/mol [56].
The Boudouard reaction is positively affecting the system as it helps cleaning the substrate from solid carbon depositions and transforming CO_2 into more useful CO. In fact, it involves atomic oxygen adsorbed at the surface as an agent. The value for the pre-exponential factor is 1.2*10^6 mol/(m^2/s), while activation energy is 185 kJ/mol [56]. The values are relative to the reaction happening over austenite, hypothesizing the difference with an iron oxide is not so important. Anyway, the influence of this reaction (also called char gasification) is insignificant under 1000 K [57].
Steam reforming 3.10 is also happening at those temperatures and has therefore been added to the simulation. This reaction converts CH_4 into H_2 and CO by making use of H_2O. It is favoured at high temperatures as it is an endothermic reaction. The values of pre-exponential factor and energy activation over a ferrite are 1.3*10^7 mol/(m^2/s) and 214 kJ/mol respectively [56].
Additionally, the software required some other input parameters for successfully running the simulation. Since the different tests presented some differences from one another, the model was built as to be as much similar as possible to the layout of test #3, which was the one giving the most interesting and complete results. The volume of the reactor was set to be of 4.278*10^{-6} m^3, calculated considering a diameter of the pipe of

1.537 cm and an L/D ratio of 1.5. The reacting surface has been calculated considering that the particles of hematite might have a spherical shape. The average size of each particle has been considered to be around 20 μm, according to Lu et al. [37]. Th number of spheres that fit in the selected volume has been obtained with the formula 5.17

$$N_{spheres} = \frac{6(1-\epsilon) * V_{tot}}{\pi d^3} \tag{5.17}$$

The value used for V_{tot} is the one previously indicated for the reacting volume. Once the number of particles has been calculated, it can be multiplied by the area of each spherical grain. The total area of reaction obtained is therefore 0.89 m^2.

The initial conditions of the reaction is that all the gas concentrations are set to 0, as a result of the work of the void pump. The initial surface concentrations are instead calculated considering the quantity of moles inserted in the pipe, divided by the surface of reaction. Having a quantity of powders of 2.7 g, the surface concentrations should be 0.05 mol/m^2. Nevertheless, the number of reactive sites is higher, as every molecule of hematite contains 3 oxygens. The value for moles per surface is multiplied by 3 and set to 1.5 mol/m^2.

The model is also set with a feed inlet of a mixture of CH_4 in N_2 in the same proportions as in the experiment (35% CH_4 and 65% N_2).

5.2.2 Results

The output of the simulation is a graph representing the behaviour of the flue gases concentrations plotted against time. In fact, the selected model was a time-dependent scenario, aiming at calculating the variations in the reactor with the proceeding of the reaction.

Results for CH_4, CO, H_2 and CO_2 are shown in Fig. 55. The comparison with the data collected during test #3 comes easy, as reported in Fig. 56. The most interesting aspect for the thesis, is to find common patterns between the real and simulated data, together with highlighting any difference. First of all, it can be seen how, when the injection of methane starts (at 0 s in Fig. 55 and around 13.2 in Fig. 56), a sudden increase in the relative quantities of all the other gases is detected. In particular, H_2 oscillates between

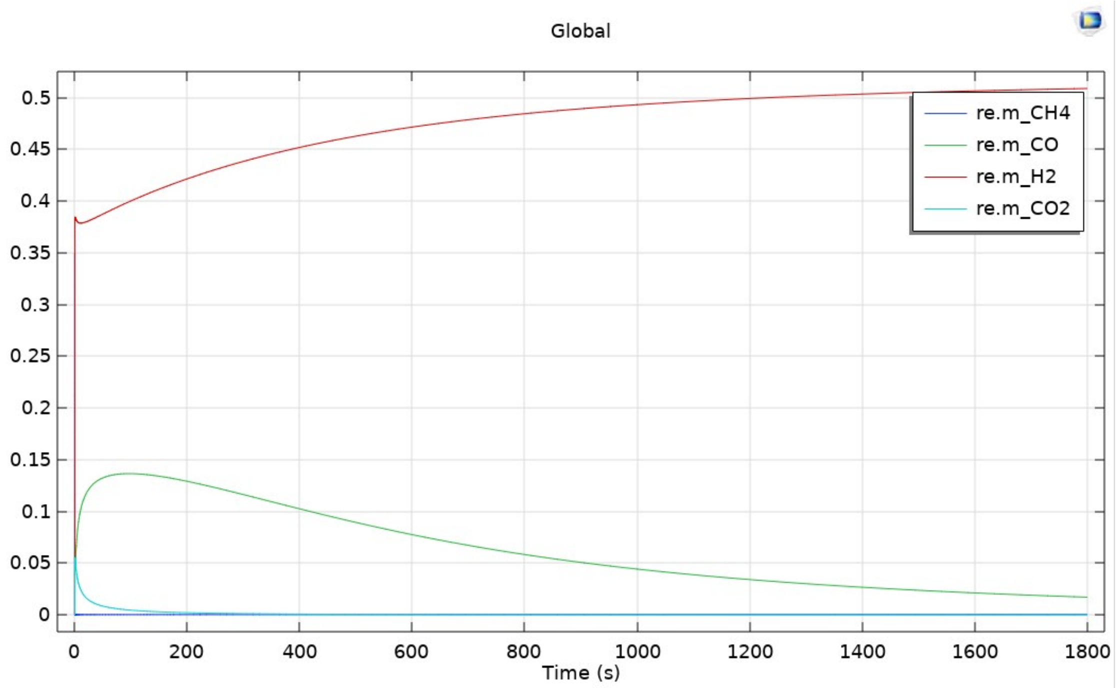

Figure 55 – The graph represents the results of the simulation for the same flue gases that were detected by the experimental tests.

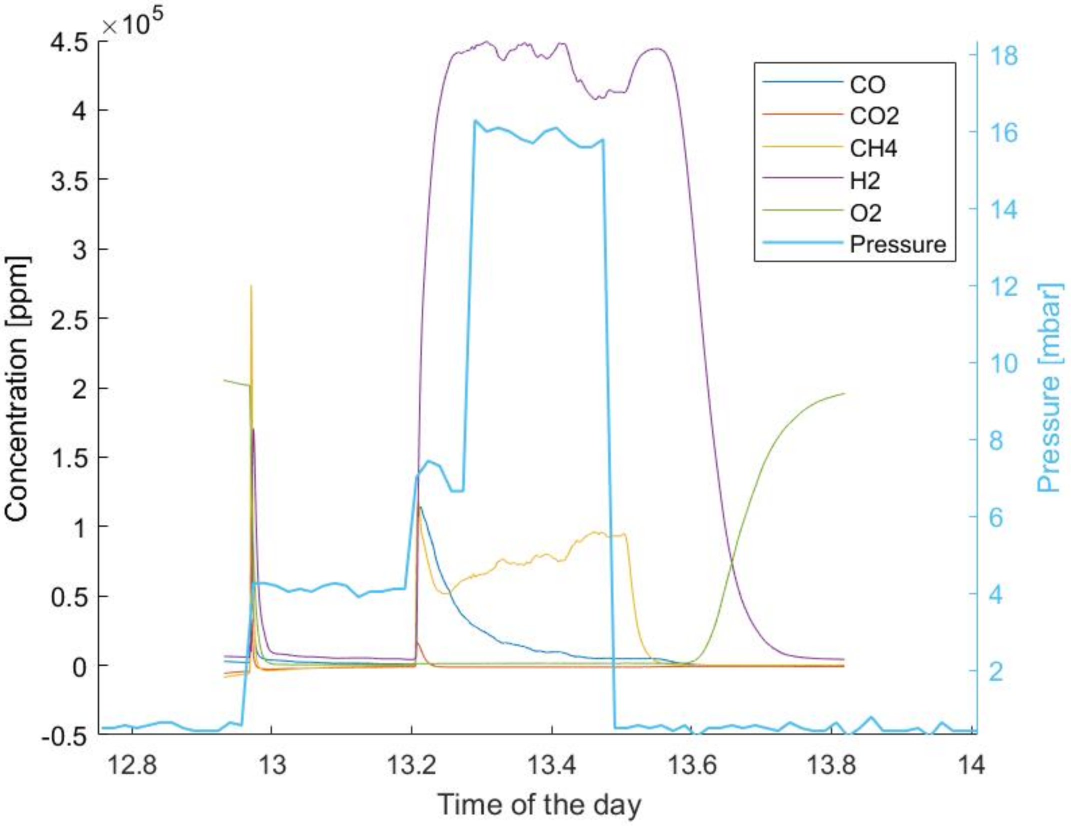

Figure 56 – Results of test #3 performed on 9^{th} July.

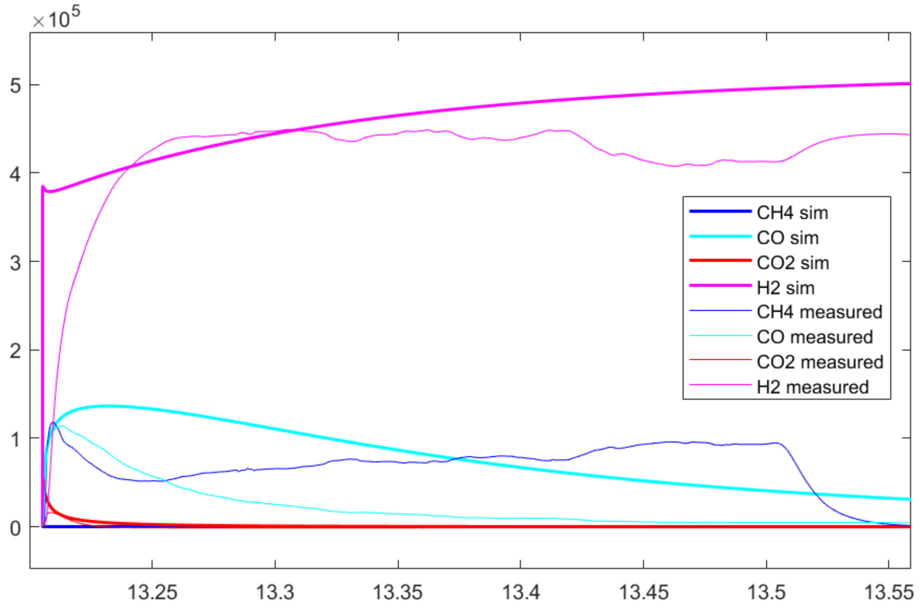

Figure 57 – The graph is comparing the results of the experimental test #3 and of the simulation. It has been considered to launch the simulation at the same time the injection of methane started in the reactor.

40% and 45% in the real case, while in the simulation results it grows from a bit less than 40% up to 50%. As previously explained, the sudden decrease in H_2 concentration in Fig. 56 is explicated by the rupture of the pipe, and has nothing to do with the chemistry of the untouched reactor. CO as well shows an immediate peak between 10 and 15% (a bit delayed in the simulation) and then decreases towards very low fractions. CO_2 follows a similar pattern as CO in both the figures, but starting from a much lower peak. The main difference is represented by CH_4. In fact, in the real experiment, the analytic was detecting a fraction of unreacted methane in the flue mixture, while this is not happening in the simulation. This might be due to the more idealistic nature of the chemical reaction in the software that might not be taking into account other forms of imperfections. The presence of both CO, H_2 and CO_2, although in very little quantities is in line with what stated by Monazam et al. [36] as CLC and CLPO are happening at the same time.

Fig. 57 plots both the data sets and therefore makes it easier to compare.

Once the results have been compared and in case the simulation is found to be compelling, it is interesting to also check the other components of the reaction. Fig. 58 shows

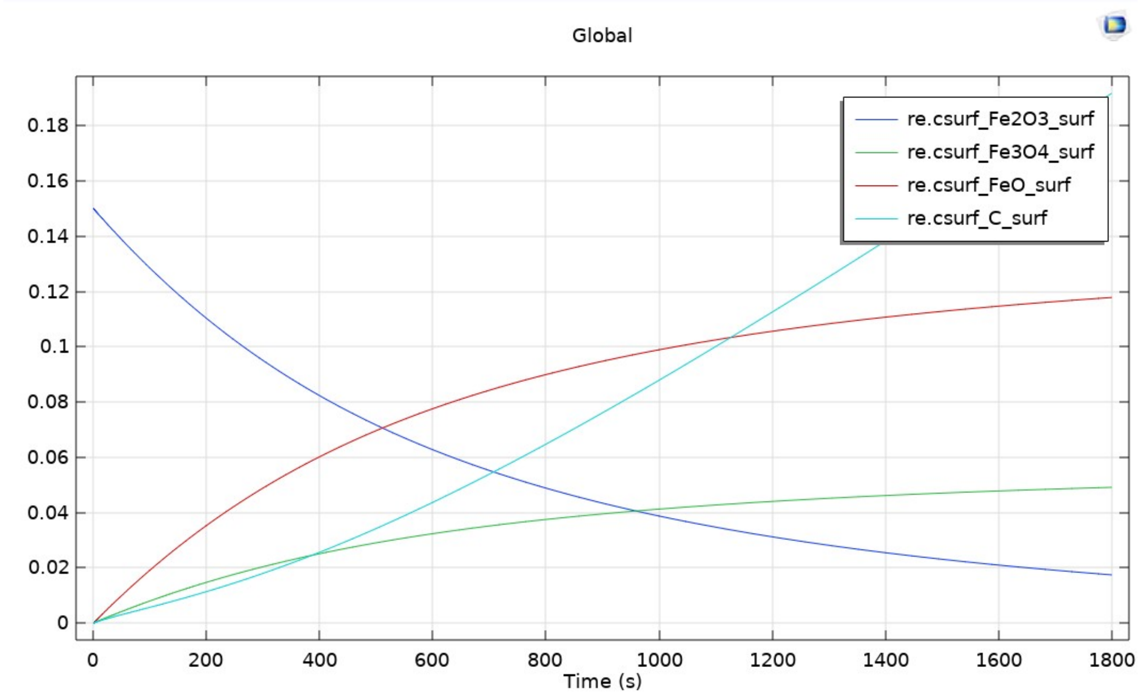

Figure 58 – Surface concentrations in mol/m^2 of the solid components in the reactor.

how the concentrations of the solid reactants and products of the reactions are changing during time. The most obvious thing is that the quantity of hematite is decreasing. At the same time, FeO and Fe_3O_4 are being produced, but in different quantities: wüstite is more abundant, while magnetite is being produced less. Therefore, at this temperature level and with this quantity of CH_4 as reducing gas, total reduction of the carrier is predominant on partial reduction. Moreover, there is an increase in carbon deposition, that is, surface concentration of solid carbon over the carrier. This might be happening as methane cracking, eq.17 is favoured in this temperature range. This could be explaining the reason why as hematite decrease and CO and CO_2 are being produced in lower quantities, H_2 does not follow the same behaviour. Hydrogen is instead kept at a more or less stable quantity that does not decrease in the 30 minutes of the simulation.

6

CONCLUSIONS

The thesis explored and investigated various aspects of chemical looping for green hydrogen production. Starting with a review of the state of the art of CSP technology provided the knowledge to operate the solar collector facility on the Energy Center rooftop. To optimize the use of this machine, not only the knowledge of solar geometry, but also observation of empirical aspects turned out to be extremely important. Knowing the larger path of the Sun during the summer season, helped understanding how the machine was not fully exploiting it as it was not able to switch on sufficiently early. Therefore, a modification of the setup (displacement of the end-of-run sensor) was required to make use of the solar collector earlier in the morning. Empirical trials for finding the focus, before actually receiving precise instructions from El.Ma. enabled to gain a deeper knowledge of the imperfections and problems of the reflecting surface. Subsequently, literature review on the topic of chemical looping reduction and oxygen carriers for hydrogen production, finally allowed to highlight the most interesting opportunity for setting up the experiment. Use of methane allowed to reduce the carrier at lower temperatures than with pure thermal reduction. After these more theoretical problems, the experimental setup encountered some other problems. In fact, the materials used for the reactor were not performing as well as foresaw. In particular, they experienced quick thermal degradation and loss of structural integrity. Alumina, the ceramic used at beginning, was cracking during every test, especially when the solar irradiation reached summer levels. The extreme temperature gradient at which the pipe was exposed to was considered responsible for this. Subsequently, a metallic

pipe was considered and used. Although it was initially excluded as an option, it finally turned out to be the game changer. A metallic pipe, especially Inconel Hastelloy, was not suffering thermal gradients that much, and was keeping its structural integrity longer. Anyway, no material used in this series of experiments was able to sustain those condition for longer than one cycle (only considering reduction).
As a result of the intensive work, the reduction reaction was finally carried out in the solar concentrator on the rooftop of the Energy Center. This achievement is successfully in line with the work previously done on chemical looping and the theses of the other students. Additionally, it finally demonstrated the feasibility of the reaction in real conditions. Previous work indeed, only happened to reproduce the reduction and oxidation in controlled conditions (i.e., inside a laboratory oven). The experiments performed in the sense of this thesis were useful to show that the process is implementable in a real case despite all the difficulties encountered. Moreover, the work allowed to gain a much deeper knowledge on the issues that might hamper the efficacy of the process and their effect on the process.

The main takeaways of the thesis can be summarized as follows:

- The production of hydrogen is already extremely relevant in the reduction phase of the loop. In fact, it takes up to almost half of the moles present in the outflowing gas. The rest is made up of CO, under 10% and a very little quantity of CO_2. The unreacted CH_4 is around 10% according to the real data collected during test #3. Anyway, the simulation resulted a fraction of methane of 0. It might be possible to lower the quantity of unreacted methane in real experiments by varying the fraction of the gas in the inlet feed or the relative quantity of powder.

- By looking at the flue gases from the experiments it looked like partial oxidation overcame total oxidation, especially with the proceeding of the reaction. This result is in accordance also with what found by Monazam at al. [36].

- The simulation highlighted the happening of strong carbon deposition over the carrier, and this seems to be consistent also for other clues. In fact, despite the quantities of CO and CO_2 produced are decreasing with the proceeding of the reaction and subsequent exhaustion of hematite, H_2 levels look not to be altered significantly. This might be happening because the molecules of methane are cracked as a consequence of the suitable temperature range and catalytic action of hematite.

- The concentration of Sun beams on the external surface of a horizontal cylinder poses several threats to the efficacy of the receiver. As the radiation hits asymmetrically the pipe, the material is posed under stress that might hinder its structural properties. A ceramic such as the alumina used for the receivers in these tests can not stand this kind of situation. In fact, the use is completely different from the application inside an oven: it is not heated heated up slowly, and not uniformly along all the dimensions of the object. Moreover, the receiver is exposed to the risk of extreme temperature changes that might cause a thermal shock. In fact, according to [20], the maximum thermal shock resistance of alumina is between 200 and 300°C depending on the test. Moreover, its low thermal conductivity (between 16 and 35 W/mK [20]) combined with its coefficient of thermal expansion (between 7.2 and 8.3 μ/mK, comparable to the one of steels [20]), can cause extremely strong and localized thermal stresses that can finally result in the failure of the sample. Therefore, if alumina is to be used, a different shape of the receiver should be used.The reactor must be heated up as more homogeneously as possible on all its faces, to avoid localized hot-spots.

  A solution could be represented by the use of a secondary concentrator to catch the light collected by the first reflecting surface and redistribute it.

  Compound parabolic concentrators (CPCs) have to be placed instead of the receiver, but can direct the light in their central area (depending on the type) and are therefore more suitable to homogeneously heat up the sample. Fig. 59 shows some examples of the shape these systems.

- On the other hand, if a metallic material is to be used, an alloy able to operate at extremely high temperature has to be selected. In fact, metals used in these tests (steel AISI 316 and Inconel Hastelloy) did not present the structural fragility of alumina, but underwent melting and consequent loss of material in the area hit by

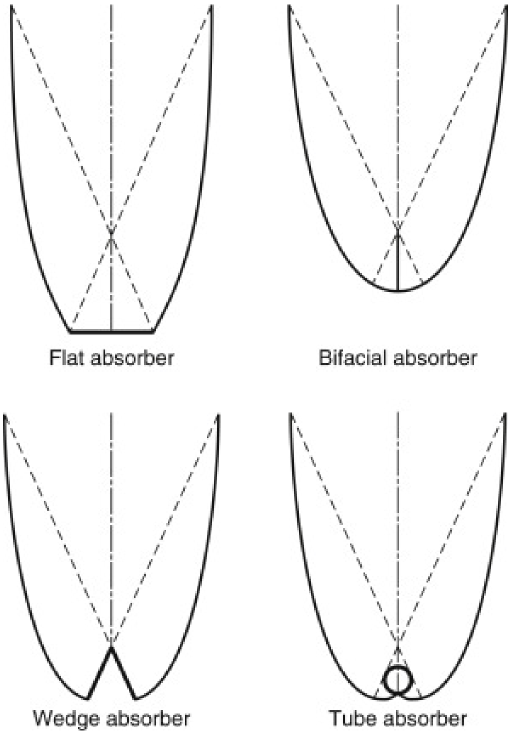

Figure 59 – Schemes of the most common types of CPCs, retrieved from [58].

the concentrated radiation. A more distributed heating up of the sample might allow not to reach extremely high temperatures in small points but the suitable temperature for the reaction over a wider area.

- The extreme variability of the weather can cause sudden decrease of temperature even during sunny days. This can not only cause the stop of the reaction, but also thermal shocks of the receiver. In case of wind gusts, the receiver can be cooled down extremely quickly and experience a too strong quench (if ceramic).

The current work leaves space to further exploration of the topic. Regarding the solar concentrator facility on the Energy Center rooftop, more studies on the type of receiver have to be made. These include both the choice of a more appropriate shape that can better stand thermal stresses together with a material able to resist those extreme temperatures. In fact, the pipe reactor poses severe limitations on the applicability of the technology. In fact, the reactors were breaking down too quickly for studying the complete reaction.

Together with that, some sort of protection from adverse atmospheric conditions should be implemented to avoid sudden temperature variations. A possible path could be implementing a thermal energy storage, so that the thermal inertia of the reactor is augmented.

Regarding the loop, the thesis covered mainly the reduction phase. The oxidation step has not been implemented yet in the solar facility and can be object of further exploration. Once more stable conditions can be reached in the reactor, additional considerations can be made around the chemical looping reactions, such as the influence of temperature and methane fraction in the feed.

To my family, who helped me getting rid of even the littlest obstacle from my path.

To my friends, who took out even the tiniest rock from my heart.

To all the people I met that taught me how humans are

the most important things we will ever have in life.

Thank you for all the marvelous adventures until now.

BIBLIOGRAPHY

[1] European Commission. *2030 Climate Target Plan*. https://ec.europa.eu/clima/policies/eu-climate-action/2030_ctp_en. Accessed on 08/09/2021.

[2] V. Tzelepi et al. “Biomass Availability in Europe as an Alternative Fuel for Full Conversion of Lignite Power Plants: A Critical Review”. In: *Energies* 13.13 (2020). DOI: 10.3390/en13133390.

[3] A. Gallo et al. “High flux solar simulators for concentrated solar thermal research: A review”. In: *Renewable and Sustainable Energy Reviews* 77 (2017), pp. 1385–1402. DOI: https://doi.org/10.1016/j.rser.2017.01.056.

[4] J. Ekanayake N. Jenkins. *Renewable Energy Engineering*. Cambridge University Press, 2017, pp. 227–229. ISBN: 1107680220.

[5] B. Hoffschmidt et al. *3.06 - High Concentration Solar Collectors*. Ed. by Ali Sayigh. Oxford: Elsevier, 2012, pp. 165–209. ISBN: 978-0-08-087873-7.

[6] C. Andraka J. Coventry. “Dish systems for CSP”. In: *Solar Energy* (2017). DOI: https://doi.org/10.1016/j.solener.2017.02.056.

[7] Jeffrey R.S. Brownson. *Chapter 06 - Sun-Earth Geometry*. Ed. by Jeffrey R.S. Brownson. Boston: Academic Press, 2014, pp. 135–178. ISBN: 978-0-12-397021-3.

[8] Rafael Guédez. *Renewable Energy Technology, Advanced Course, VT201*. University Lecture. 2020.

[9] Soteris A. Kalogirou. *Chapter 2 - Environmental Characteristics*. Ed. by Soteris A. Kalogirou. Second Edition. Boston: Academic Press, 2014, pp. 51–123. ISBN: 978-0-12-397270-5.

[10] A. Da Rosa. "Chapter 12 - Solar Radiation". In: *Fundamentals of Renewable Energy Processes (Third Edition)*. Ed. by Aldo da Rosa. Third Edition. Boston: Academic Press, 2013, pp. 485–532. ISBN: 978-0-12-397219-4.

[11] J. Pye K. Lovegrove. *2 - Fundamental principles of concentrating solar power (CSP) systems*. Ed. by Keith Lovegrove and Wes Stein. Woodhead Publishing Series in Energy. Woodhead Publishing, 2012, pp. 16–67. DOI: https://doi.org/10.1533/9780857096173.1.16.

[12] M. Günther et al. "Advanced CSP Teaching Materials Chapter 2 Solar Radiation". In: 2011.

[13] A.Z. Hafez et al. "Design analysis factors and specifications of solar dish technologies for different systems and applications". In: *Renewable and Sustainable Energy Reviews* 67 (2017), pp. 1019–1036. DOI: https://doi.org/10.1016/j.rser.2016.09.077.

[14] NOAA's National Weather Service. *Glossary*. https://forecast.weather.gov/glossary.php?word=Sky%20Condition. Accessed on 08/06/21.

[15] R. Perez et al. "Modeling daylight availability and irradiance components from direct and global irradiance". In: *Solar Energy* 44.5 (1990), pp. 271–289. DOI: https://doi.org/10.1016/0038-092X(90)90055-H.

[16] Commission Internationale de Eclairage. "Standardization of Luminous Efficacy Distribution on Clear Skies". In: 222 (1973).

[17] *El.Ma. website*. https://www.elmanet.info/azienda?lang=en. Accessed on 08/08/2021.

[18] El.Ma. srl. *MANUALE USO E MANUTENZIONE - Concentratore solare a disco - Matr. 10434 - Anno costruzione: 2019*.

[19] S. Colombo. *Experimental selection of optimal chemical looping conditions using iron oxides for applications in CSP systems*. Master Student Thesis. 2021.

[20] A. Ruys. "4 - Processing, structure, and properties of alumina ceramics". In: *Alumina Ceramics*. Ed. by A. Ruys. Woodhead Publishing Series in Biomaterials. Woodhead Publishing, 2019, pp. 71–121. DOI: https://doi.org/10.1016/B978-0-08-102442-3.00004-X.

[21] M. Santarelli. *Polygeneration and advanced energy systems, 01QGXND*. University Lecture. 2020.

[22] R. Banerjee D. Yadav. "A review of solar thermochemical processes". In: *Renewable and Sustainable Energy Reviews* 54 (2016), pp. 497–532. ISSN: 1364-0321.

[23] J. Wang et al. "Thermodynamic Properties for Carbon Dioxide". In: *ACS Omega* 4.21 (2019), pp. 19193–19198. DOI: 10.1021/acsomega.9b02488.

[24] J. R. Scheffe R. J. Carrillo. "Advances and trends in redox materials for solar thermochemical fuel production". In: *Solar Energy* 156 (2017). Advances in Solar Thermochemistry, pp. 3–20. DOI: https://doi.org/10.1016/j.solener.2017.05.032.

[25] P. Furler et al. "Solar Thermochemical CO2 Splitting Utilizing a Reticulated Porous Ceria Redox System". In: *Energy & Fuels* 26.11 (2012), pp. 7051–7059. DOI: https://dx.doi.org/10.1021/ef3013757.

[26] C. Agrafiotis et al. "A review on solar thermal syngas production via redox pair-based water/carbon dioxide splitting thermochemical cycles". In: *Renewable and Sustainable Energy Reviews* 42 (2015), pp. 254–285. ISSN: 1364-0321.

[27] J. R. Scheffe and A. Steinfeld. "Oxygen exchange materials for solar thermochemical splitting of H2O and CO2: a review". In: *Materials Today* 17.7 (2014), pp. 341–348. DOI: 10.1016/j.mattod.2014.04.025.

[28] C. Perkins and A. W. Weimer. "Likely near-term solar-thermal water splitting technologies". In: *International Journal of Hydrogen Energy* 29.15 (2004), pp. 1587–1599. DOI: https://doi.org/10.1016/j.ijhydene.2004.02.019.

[29] R. D. Palumbo and C. L. Larson. "Production of C from CO, in a two-step solar process utilizing FeO and Fe_3O_4". In: *Department of Mechanical Engineering, Valparaiso University, Valparaiso, IN 46383, U.S.A.* (1989). DOI: https://doi.org/10.1016/0360-5442(90)90053-5.

[30] A. Tofighi F. Sibieude M. Ducarroir and J. Ambriz. "High temperature experiments with a solar furnace: The decomposition of Fe3O4, Mn3O4, CdO". In: *International Journal of Hydrogen Energy* 7.1 (1982), pp. 79–88. ISSN: 0360-3199.

[31] I. Bransky and A. Z. Hed. "Thermogravimetric Determination of the Composition-Oxygen Partial Pressure Diagram of Wustite (Fe1-y O)". In: *Journal of the American Ceramic Society* 51.4 (1968), pp. 231–231. DOI: 10.1111/j.1151-2916.1968.tb11884.x.

[32] L. S. Darken and R. W. Gurry. "The System Iron-Oxygen. I. The Wüstite Field and Related Equilibria". In: *Journal of the American Chemical Society* 67.8 (1945), pp. 1398–1412. DOI: 10.1021/ja01224a050.

[33] O. N. Salmon. "High temperature thermodynamics of the iron oxide system". In: *The Journal of Physical Chemistry* 65.3 (1961), pp. 550–556. DOI: 10.1021/j100821a039.

[34] P. Charvin et al. "Two-step water splitting thermochemical cycle based on iron oxide redox pair for solar hydrogen production". In: *Energy* 32.7 (2007), pp. 1124–1133. DOI: https://doi.org/10.1016/j.energy.2006.07.023.

[35] M. Najera et al. "Carbon capture and utilization via chemical looping dry reforming". In: *Chemical Engineering Research and Design* 89.9 (2011), pp. 1533–1543. DOI: https://doi.org/10.1016/j.cherd.2010.12.017.

[36] E. R. Monazam et al. "Kinetics of the reduction of hematite (Fe2O3) by methane (CH4) during chemical looping combustion: A global mechanism". In: *Chemical Engineering Journal* 232 (2013), pp. 478–487. DOI: https://doi.org/10.1016/j.cej.2013.07.091.

[37] C. Lu et al. "Chemical looping reforming of methane using magnetite as oxygen carrier: Structure evolution and reduction kinetics". In: *Applied Energy* 211 (2018), pp. 1–14. DOI: https://doi.org/10.1016/j.apenergy.2017.11.049.

[38] S. Bhavsar et al. "Chapter 7 - Chemical-looping processes for fuel-flexible combustion and fuel production". In: *Reactor and Process Design in Sustainable Energy Technology*. Ed. by Fan Shi. Amsterdam: Elsevier, 2014, pp. 233–280. DOI: https://doi.org/10.1016/B978-0-444-59566-9.00007-7.

[39] *Production of hydrogen via the steam-iron process*. US Patent US3442620A. 1968.

[40] M. Rydén and M. Arjmand. "Continuous hydrogen production via the steam–iron reaction by chemical looping in a circulating fluidized-bed reactor". In: *International Journal of Hydrogen Energy* 37.6 (2012), pp. 4843–4854. DOI: https://doi.org/10.1016/j.ijhydene.2011.12.037.

[41] P. Chiesa et al. "Three-reactors chemical looping process for hydrogen production". In: *International Journal of Hydrogen Energy* 33.9 (2008), pp. 2233–2245. DOI: https://doi.org/10.1016/j.ijhydene.2008.02.032.

[42] Kang Seok Go et al. “Hydrogen production from two-step steam methane reforming in a fluidized bed reactor”. In: *International Journal of Hydrogen Energy* 34.3 (2009), pp. 1301–1309. DOI: https://doi.org/10.1016/j.ijhydene.2008.11.062.

[43] A. Ashcroft, A. Cheetham, and M. Green. “Partial oxidation of methane to synthesis gas using carbon dioxide”. In: *Nature* 352 (1991), pp. 225–226. DOI: https://doi.org/10.1038/352225a0.

[44] S. Vyazovkin. “Conversion dependence of activation energy for model DSC curves of consecutive reactions”. In: *Thermochimica Acta* 236 (1994), pp. 1–13. DOI: https://doi.org/10.1016/0040-6031(94)80249-1.

[45] Y. Tamaura et al. “Production of solar hydrogen by a novel, 2-step, water-splitting thermochemical cycle”. In: *Energy* 20.4 (1995), pp. 325–330. ISSN: 0360-5442.

[46] M. Guo et al. “Cobalt doping modification for enhanced methane conversion at low temperature in chemical looping reforming systems”. In: *Catalysis Today* 350 (2020). Frontier of Catalysis of Energy and Fuels: From Catalyst Synthesis to Production Yield, pp. 156–164. DOI: https://doi.org/10.1016/j.cattod.2019.06.016.

[47] L. Qin et al. “Impact of 1% Lanthanum Dopant on Carbonaceous Fuel Redox Reactions with an Iron-Based Oxygen Carrier in Chemical Looping Processes”. In: *ACS Energy Letters* 2.1 (2017), pp. 70–74. DOI: https://doi.org/10.1021/acsenergylett.6b00511.

[48] L. Ma et al. “Spinel-Structured Ternary Ferrites as Effective Agents for Chemical Looping CO2 Splitting”. In: *Industrial & Engineering Chemistry Research* 59.15 (2020), pp. 6924–6930. DOI: https://doi.org/10.1021/acs.iecr.9b06799.

[49] A. Navrotsky. “Energetics and Crystal Chemical Systematics among Ilmenite, Lithium Niobate, and Perovskite Structures”. In: *Chemistry of Materials* 10.10 (1998), pp. 2787–2793. DOI: https://doi.org/10.1021/cm9801901.

[50] Q. Jiang et al. “Thermochemical CO2 splitting reaction with supported LaxA1xFeyB1yO3 (A=Sr, Ce, B=Co, Mn; 0x, y1) perovskite oxides”. In: *Solar Energy* 103 (2014), pp. 425–437. DOI: https://doi.org/10.1016/j.solener.2014.02.033.

[51] Emerson. *Flyer process gas analytical solutions for gas purity rosemount*.

[52] Mesa Labs. “Definer™ 220 Series, User Manual”. In: ().

[53] Advalue Technology. *Technical Information on Alumina Products*. https://www.advaluetech.com/technical-alumina-products. Accessed on 07/08/21.

[54] The World Material. *AISI 316 Stainless Steel Properties, SS 316 Grade Density, Composition, Yield Strength, Thermal Conductivity*. https://www.theworldmaterial.com/aisi-316-ss316-stainless-steel-properties-composition/. Accessed on 07/08/21.

[55] Internet Archive. *Activation Energy*. https://web.archive.org/web/20161207175516/http://www.chem.fsu.edu/chemlab/chm1046course/activation. Accessed on 22/08/21.

[56] J.T. Slycke et al. "1 - Thermodynamics and kinetics of gas and gas–solid reactions". In: *Thermochemical Surface Engineering of Steels*. Ed. by Eric J. Mittemeijer and Marcel A.J. Somers. Oxford: Woodhead Publishing, 2015, pp. 3–111. DOI: https://doi.org/10.1533/9780857096524.1.3.

[57] P. Basu. "Chapter 7 - Gasification Theory". In: *Biomass Gasification, Pyrolysis and Torrefaction (Third Edition)*. Ed. by P. Basu. Third Edition. Academic Press, 2018, pp. 211–262. DOI: https://doi.org/10.1016/B978-0-12-812992-0.00007-8.

[58] S. A. Kalogirou. "Chapter 3 - Solar Energy Collectors". In: *Solar Energy Engineering (Second Edition)*. Ed. by S. A. Kalogirou. Second Edition. Boston: Academic Press, 2014, pp. 125–220. DOI: https://doi.org/10.1016/B978-0-12-397270-5.00003-0.

A

APPENDIX

A.1 Test #1

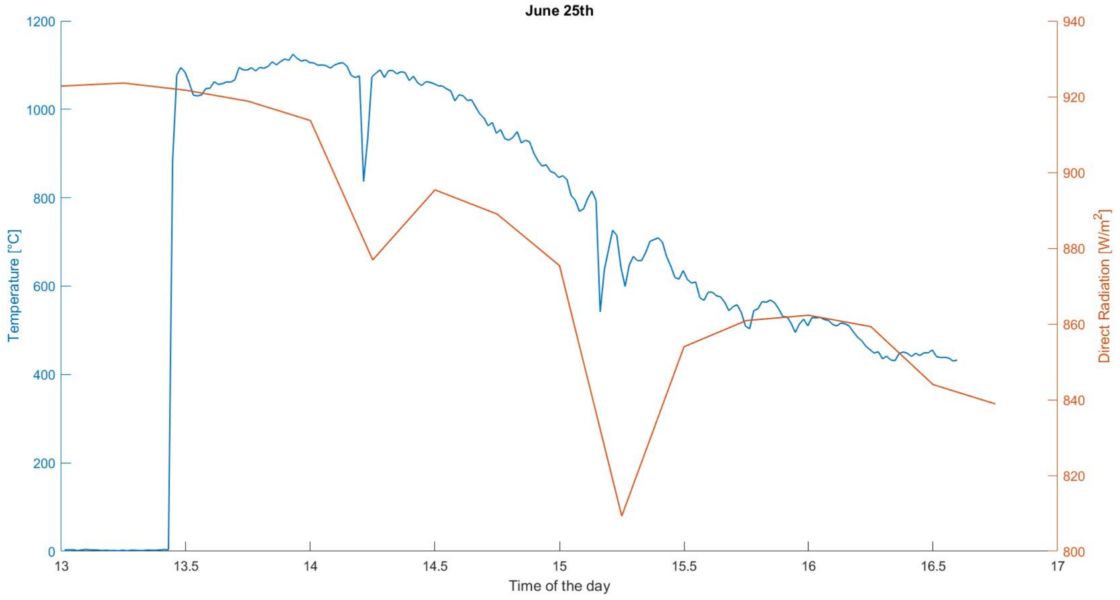

Figure 60 – Temperature and global radiation for the duration of test 1. The oscillations of the temperature are due to the position of the thermocouple, which is external in this case. It has been noticed while running the test that even the lightest wind gust cause a sudden decrease of temperature.

A.2 Test #2

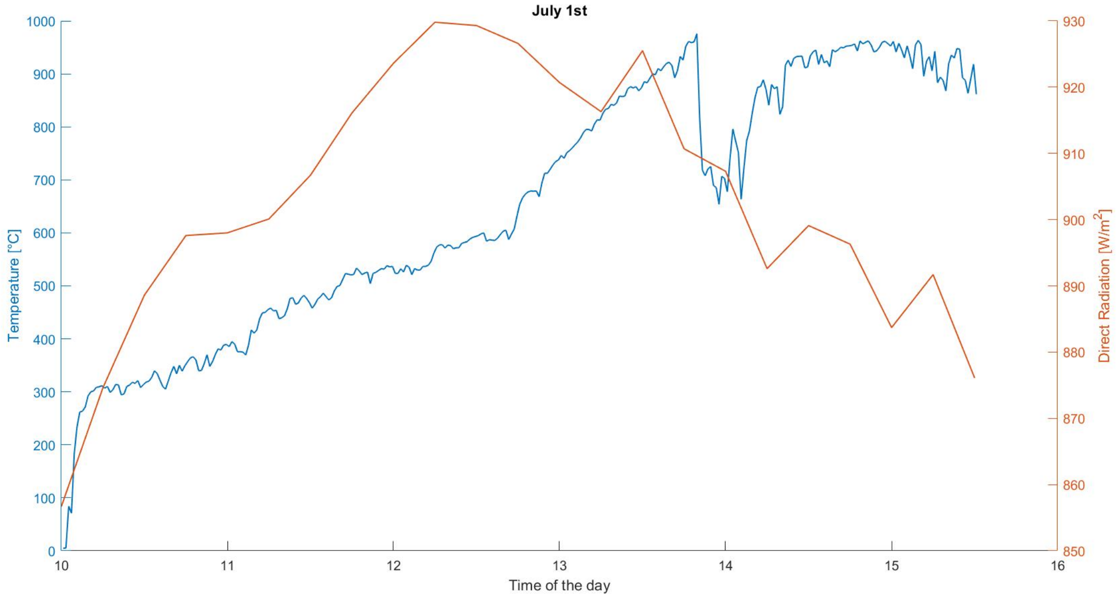

Figure 61 – Temperature and global radiation for the duration of test 2. Here it is possible to see a much more gradual growth of the temperature thanks to the slow removal of paper sheet covering part of the reflective surface. The sudden loss of heat flux unfortunately caused a decrease of T some minutes before 14:00. As radiation data are collected every 15 minutes, the cloud passage was not even recorded.